University of Science and Technology of China

Hefei, CHINA

Single Electron Transverse Momentum and Azimuthal Anisotropy Distributions: Charm Hadron Production at RHIC

A dissertation submitted

for the degree of

Doctor of Philosophy in Physics

by

Xin Dong

Co-supervisors: Ziping Zhang, Nu Xu

2005

© Copyright by

Xin Dong

2005

All Rights Reserved

Table of Contents

1 Introduction: Quantum Chromodynamics and Heavy Ion Collisions . 1

1.1 Quantum Chromodynamics 1

1.1.1 QCD running coupling constant α_s 2

1.1.2 Perturbative QCD (pQCD) 2

1.1.3 Confinement and chiral symmetry breaking 5

1.1.4 QCD Phase transition 6

1.2 Heavy Ion Collisions 7

1.2.1 Nucleon stopping power and initial energy density 9

1.2.2 Jet quenching 10

1.2.3 Collective motion 12

1.2.4 Transverse azimuthal anisotropy 13

1.2.5 Heavy flavor production in HIC 16

1.2.6 What have we learned so far? 17

2 Experimental Set-up 19

2.1 RHIC accelerator 19

2.2 STAR detector 21

2.3 Main tracker - TPC 23

2.4 Prototype TOF detector 25

3 Single electron transverse momentum distributions 30

3.1 Single electrons from d + Au and $p+p$ collisions at $\sqrt{s_{NN}} = 200$ GeV . . 30

3.1.1 Data sets and Trigger 30

3.1.2 Electron identification and hadron contamination 31

3.1.3 Acceptance, Efficiency and Trigger bias 36
3.1.4 Photonic background contribution 38
3.1.5 Signal extraction 41
3.1.6 Background subtraction check 45
3.1.7 Electron dN/dy and implications for total charm production cross section 46
3.1.8 Systematic error study 50
3.2 Single electrons from Au + Au collisions at $\sqrt{s_{NN}} = 62.4$ GeV 51
3.2.1 Data set and electron PID 51
3.2.2 Non-photonic background estimation in Au + Au 53
3.2.3 Spectra from Au + Au collisions at $\sqrt{s_{NN}} = 62.4$ GeV 57

4 Single electron azimuthal anisotropy distributions 59
4.1 Event plane and its resolution 59
4.2 Elliptic flow of stable hadrons 62
4.3 Elliptic flow of inclusive and photonic background electrons 65

5 Discussion 72
5.1 Open charm production in high energy collisions 72
5.1.1 Total charm cross section 72
5.1.2 Spectrum comparison 75
5.1.3 Bottom contribution 78
5.1.4 Cronin effect of charm hadrons in d + Au 79
5.2 Closed charm production 80
5.2.1 J/ψ production in $p+p$ collisions 80
5.2.2 J/ψ production in heavy ion collisions 81

5.3 Elliptic flow of charm quarks and thermalization 83

6 Outlook **86**

6.1 Detector upgrade proposals 86

6.2 Open charm measurements 87

6.3 Low mass e^+e^- spectrum 89

A QCD Lagrangian **93**

A.1 Notations 93

A.2 $SU(3)_C$ invariant QCD Lagrangian 94

A.3 Chiral symmetry and effective chiral Lagrangian 96

B Kinematic variables **99**

C Low energy charm cross section data points selection **101**

References **104**

List of Figures

1.1 QCD running coupling constant α_s 3

1.2 LQCD calculation for pressure 6

1.3 LQCD calculation for heavy quark potential 7

1.4 QCD phase diagram 8

1.5 Rapidity loss in heavy ion collisions 9

1.6 R_{AB} of Au + Au and d + Au 11

1.7 Dihadron correlations 11

1.8 $\langle p_T \rangle$ of away side jet 11

1.9 Blast-wave fit for PID spectra 12

1.10 Blast-wave fit results 14

1.11 PID v_2 at low p_T 15

1.12 PID v_2 scaling 15

1.13 Time scale diagram 17

2.1 The RHIC complex 20

2.2 Cutaway view of STAR 21

2.3 Cutaway view of the TPC detector 23

2.4 PID capability of STAR 26

2.5 Two-side view of a MRPC module 27

2.6 TOFr hadron PID 28

3.1 Electron PID with TOF and dE/dx 32

3.2 dE/dx fit with TOF PID cut 33

3.3 dE/dx fit at higher p_T 34

3.4 Hadron contamination 35

3.5 Efficiency vs. contamination 35

3.6 Electron to hadron ratio 35

3.7 TPC efficiency for electrons 37

3.8 Total efficiency for electrons 37

3.9 $M^2_{e^+e^-}$ and opening angle distributions 39

3.10 Conversion efficiency 40

3.11 Ratio of conversion to Dalitz 40

3.12 Other background fractions 41

3.13 Electron spectra 42

3.14 Random rejection fractions 43

3.15 Vertex Z check 45

3.16 Separate e^+ and e^- spectra 46

3.17 p_T correlation of D and e 47

3.18 Combined fit 49

3.19 Electron PID in Au + Au 62.4 GeV 52

3.20 Hadron contamination in Au + Au 62.4 GeV 53

3.21 $M_{e^+e^-}$ in Au + Au 62.4 GeV 54

3.22 Background reconstruction in Au + Au 62.4 GeV 54

3.23 Background efficiency in Au + Au 62.4 GeV 56

3.24 Photonic background contribution in Au + Au 62.4 GeV 56

3.25 Matching efficiency in Au + Au 62.4 GeV 57

3.26 Electron spectrum in Au + Au 62.4 GeV 58

4.1 ϕ weight distribution 60

4.2 Event plane distribution 61

4.3 Event plane resolutions for all centrality bins 62

4.4 v_2 of $\pi^{\pm}$, $K^{\pm}$ and $p(\bar{p})$ 64

4.5 v_2 comparison with 200 GeV data 64

4.6 Pion v_2 in large p_T region 65

4.7 v_2 of inclusive electrons and pions 66

4.8 $M_{e^+e^-}$ distribution in every $\Delta\phi$ bin 68

4.9 Subtracted $M_{e^+e^-}$ distribution in every $\Delta\phi$ bin 69

4.10 $\Delta\phi$ distribution of photonic electrons 70

4.11 Electron v_2 result 70

5.1 Total charm cross section 73

5.2 Charm differential cross section at mid-rapidity 75

5.3 Spectra consistency check 76

5.4 Electron spectra from different energies 76

5.5 Comparison with PYTHIA 77

5.6 Charm and bottom contributions 78

5.7 R^e_{dAu} plot 80

5.8 $\sigma_{J/\psi}$ compared with $\sigma_{c\bar{c}}$ 81

5.9 J/ψ predictions from models 83

5.10 v_2 of electrons from D and π^0 84

6.1 R_{AA} of charm hadrons and decayed electrons 87

6.2 $M_{e^+e^-}$ of electron pairs from simulation 90

6.3 Conversion electrons rejection with HFT 91

List of Tables

2.1 TOF system performance 27

3.1 Data sets list 31

3.2 Electron selection criteria 36

3.3 Fractions of background 42

3.4 Non-photonic electron spectra 44

3.5 Combined fit 48

3.6 Systematic errors 50

3.7 Electron selection criteria in Au + Au 52

3.8 Partner candidate selection criteria in Au + Au 53

4.1 Track selection in event plane calculation 60

4.2 Parametrization for v_2 of $K^{\pm}$ and $p + \bar{p}$ 63

6.1 N_{evt} to observe 3σ D^0 and D_s^+ 89

6.2 Electron pair contribution from background 90

6.3 N_{evt} to observe 3σ ω and ϕ 92

C.1 Data points selection 102

Acknowledgments

Abstract of the Dissertation

Single Electron Transverse Momentum and Azimuthal Anisotropy Distributions: Charm Hadron Production at RHIC

by

Xin Dong

Doctor of Philosophy in Physics

University of Science and Technology of China, Hefei, 2005

Quantum Chromodynamics (QCD) is a basic gauge field theory to describe strong interactions. Lattice QCD calculations predict a phase transition from hadronic matter to a deconfined, locally thermalized *Quark-Gluon Plasma* (QGP) state at high temperature and small baryon density. Plenty of exciting results from RHIC experiments in the first three years have demonstrated that a hot dense matter with strong collective motion which cannot be described with hadronic degrees of freedom was created at RHIC. Charm quarks are believed to be mostly created from initial gluon fusion in heavy ion collisions. Since they are massive, charm hadrons are proposed to be ideal probes to study the early stage dynamics in heavy ion collisions.

We provide here an indirect measurement of charm semi-leptonic decay. Single electron transverse momentum (p_T) distributions from 200 GeV d + Au , $p+p$ collisions and 62.4 GeV Au + Au collisions, and single electron azimuthal anisotropy (v_2) from 62.4 GeV Au + Au collisions are presented.

Electron identification is performed with the combination of the prototype Time-Of-Flight detector (TOFr) and the ionization energy loss (dE/dx) in the *Time Projection Chamber* (TPC). Photonic background electrons are subtracted statistically by reconstructing the invariant mass of the tagged $e^{\pm}$ and every other partner candidate $e^{\mp}$. Partner track finding efficiency is estimated from Monte Carlo simulations. More than

$\sim$ 95% of photonic background (photon conversion and π^0 Dalitz decay) can be subtracted through this method. The non-photonic electron p_T spectrum is extracted. In Au + Au collisions at $\sqrt{s_{NN}} = 62.4$ GeV, due to low yield of charm quarks, only inclusive electron and photonic electron p_T spectra are presented to illustrate the feasibility of this method in Au + Au collisions. Electron azimuthal anisotropy in Au + Au 62.4 GeV is calculated from the event plane technique. Photonic background in each $\Delta\phi$ bin is reconstructed using the invariant mass method. v_2 of inclusive electrons and photonic electrons is presented.

The non-photonic electron p_T spectrum is consistent with the direct open charm reconstruction spectrum in d + Au collisions. The total charm production cross section per nucleon-nucleon collision is calculated from the combined fit of the D^0 spectrum and non-photonic electron spectrum in d + Au collisions. The result is $d\sigma_{c\bar{c}}^{NN}/dy = 0.30 \pm 0.04(\text{stat.}) \pm 0.09(\text{syst.})$ mb, which is significantly higher than the Next-to-Leading-Order perturbative QCD (pQCD) calculations extrapolated from low energy data points. The total charm cross section measurement is crucial to investigate J/ψ production mechanism in Au + Au collisions, which may be a robust signature of QGP formation. Not only the total yield is larger, but also the p_T spectrum is harder than those from pQCD predictions, indicating a possible unusual charm fragmentation function at RHIC energy. In Au + Au 62.4 GeV, the photonic electron p_T spectrum agrees with the inclusive electron spectrum well. The v_2 of photonic electrons also agrees with that of inclusive electrons. These are consistent with the expected low charm yield at this energy. The success of this technique in Au + Au 62.4 GeV data makes us confident about extracting both the non-photonic p_T spectrum and v_2 in the coming large 200 GeV Au + Au data set.

Many open charm measurements can be carried out with a full barrel TOF and heavy flavor tracker upgrade. These upgrades will allow us to study the details of open charm collective motion, elliptic flow, correlations and so on with much better statistics. These two sub-detector upgrades will also allow us to reconstruct vector mesons (ω, ϕ *etc.*) from the low mass di-electron invariant mass distributions, which may offer us indications of possible chiral restoration issues during a possible phase transition at RHIC.

中文摘要

单电子横动量谱和方位角各向异性分布

— RHIC能区粲粒子产生

董　昕

中国科学技术大学，2005 年6 月

量子色动力学(QCD)是一种描述强相互作用的基本的规范场理论。格点QCD计算预言在高温和低重子密度的条件下会产生从普通的强子物质到一种夸克解禁、局部热化的物质状态－夸克-胶子等离子体(QGP)的相变。位于美国布鲁克海汶国家实验室(BNL)的相对论重离子对撞机(RHIC)在头三年的运行中取得了大量的可喜的结果。这些结果都证明在RHIC上已产生了一种新的高温、高密度的且具有很强的集体运动特征的物质，这种物质不能用强子物质的自由度来描述。另一方面，在高能重离子对撞中，绝大部分粲夸克是通过初始的胶子聚合产生的。而且因为粲夸克很重，粲强子于是被认为是研究重离子碰撞产生的系统早期状态动力学的理想探针。

本文我们给出一种测量方法－通过粲夸克半轻子衰变产生的电子来得到粲强子的产生机制。本文将给出在每核子对质心能量200 GeV的氘核－金核和质子－质子碰撞中、以及在每核子对质心能量62.4 GeV的金核－金核碰撞中的单电子横动量谱。同时还将给出在每核子对质心能量62.4 GeV的金核－金核碰撞中单电子的方位角各向异性(椭圆流)分布。

在STAR探测器上，通过联合飞行时间探测器(样机)(TOFr)和时间投影室(TPC) 中的电离能损(dE/dx)可以鉴别出(正)电子。电磁过程产生的电子本底通过重建标记电子(正电子)和伴随正电子(电子)的不变质量来在统计上剪除。伴随径迹的重建效率从蒙特卡罗模拟中得到。这种方法可以剪除约95%的电磁过程本底(光子转换和中性π介子达利兹衰变)。非电磁产生的电子横动量谱便可以得到。在金－金碰撞中，由于预期的粲夸克产额很小，我们只给出单举电子谱和电磁过程本底电子的谱，以此来证明该方法

在金－金碰撞中的可行性。金－金碰撞中电子的方位角各向异性分布(椭圆流)通过重建事例平面的方法获得。电磁过程本底电子的产额在每个$\delta\phi$ 区间通过上述类似的不便质量方法来获得。于是可以给出单举电子和电磁过程本底电子的椭圆流。

氘核－金核碰撞中非电磁产生的电子横动量谱和直接重建的粲强子谱一致。通过对低横动量D^0的谱和非电磁产生的电子谱的联合拟合可以得到平均每核子对碰撞中粲夸克产生的总截面。中快度区的测量结果是$d\sigma_{c\bar{c}}^{NN}/dy = 0.30 \pm 0.04(\text{stat.}) \pm 0.09(\text{syst.})$ mb。这个结果比从低能量点延伸来的次低阶(NLO)微扰QCD(pQCD)计算结果要高。粲夸克产生总截面的测量对研究在金核－金核碰撞中J/ψ 的产生机制很关键，而J/ψ 的产生机制将是判断QGP是否形成的强有力的证据。不仅总截面比理论计算要高，横动量谱也比pQCD预言的要硬，可能预示在RHIC能区粲夸克有不寻常的碎裂函数。在金核－金核62.4 GeV碰撞中，电磁产生的本底电子与单举电子谱吻合，两者的椭圆流结果也吻合。这个结果与该能区预期的很低的粲夸克产额一致。这一方法在62.4 GeV金金数据中的成功实现确保我们在即将产生的大量的200 GeV金金数据中的分析得以进行。

利用以后即将升级的全覆盖桶部飞行时间探测器和重味粒子探测器，我们可以在很大的统计量下进行很多粲夸克的测量：集体流效应、椭圆流、关联等等。这两个探测器的升级还可以使得重建低质量端电子对的不变质量来研究矢量介子(ω, ϕ *etc.*)成为可能，这将会对RHIC上可能的相变所产生的手征宇称恢复给出解答。

CHAPTER 1

Introduction: Quantum Chromodynamics and Heavy Ion Collisions

1.1 Quantum Chromodynamics

From the lepton-nucleon *Deep Inelastic Scattering* (DIS) experiments in the late 1960's, it was formed that hadrons have structure and the quark parton model was exposed. The introduced sub-nucleon structures include quarks which are constituents of hadrons, and gluons which propagate interactions between partons. This kind of interaction, namely the strong interaction, is one of the four fundamental interactions in the nature. *Quantum ChromoDynamics* (QCD) has been established since the 1970's to describe strong interaction, and together with the unification of electroweak theory, composes the *Standard Model* (SM), which is a reasonably successful model to describe all interactions except gravity.

QCD [DKS03] is based on the gauge group $SU(3)_C$, with gauge bosons - color octet gluons for factors and a unique group coupling constant g_s. The subscript C denotes the quantum number - color, which is an exact symmetry. Quarks belong to a color triplet representation in this symmetry, but hadronic states are assumed to be color singlets in QCD. Owing to the non-abelian character of the color group, the invariant QCD Lagrangian[1] requires gauge (gluon) self-interactions, which do not appear in *Quantum ElectroDynamics* (QED) - the gauge theory describing electromagnetic interaction.

Generally speaking, QCD is a non-perturbative gauge theory in most cases. It can be

[1]See Appendix A for QCD Lagrangian

calculated using a computer-assisted method - *Lattice QCD* [Gup98]. In this calculation, the spacetime is discretized and replaced by a lattice with lattice spacing equal to a. The quark fields are only defined at the elements of the lattice and the gauge fields are defined on the links of the lattice. The action is rewritten in such a way that the limit $a \to 0$ formally gives the original continuous action. Lattice QCD has been widely used for reliable QCD calculations. The precision of Lattice QCD calculations are limited by the lattice spacing or the computing power.

1.1.1 QCD running coupling constant α_s

The renormalized QCD coupling shows a scale dependent coupling $\alpha_s(\mu)$ (running coupling), similar to that in QED. However, the QED running coupling increases with energy scale, while the gluon self-interactions lead to a complete different behavior in QCD. $\alpha_s(\mu)$ can be written as:

$$\alpha_s(\mu) \equiv \frac{g_s^2(\mu)}{4\pi} \approx \frac{4\pi}{\beta_0 \ln(\mu^2/\Lambda_{QCD}^2)} \tag{1.1}$$

When $\beta_0 > 0$, this solution illustrates the *asymptotic freedom* property: $\alpha_s \to 0$ as $\mu \to \infty$, which means QCD can be calculated perturbatively in high momentum transfer or short distance approach. On the other hand, this solution also shows strong coupling at $\mu \sim \Lambda_{QCD}$, so QCD is non-perturbative in this case. α_s needs to be determined from experiment. The world averaged α_s at the fixed-reference $\mu_0 = M_Z$ is $\alpha_s(M_Z) = 0.1187 \pm 0.002$ [Eid04], and the QCD scale $\Lambda_{QCD} \sim 200$ MeV. Fig. 1.1 shows the measured α_s at different momentum transfer scale μ compared with Lattice QCD calculations.

1.1.2 Perturbative QCD (pQCD)

At sufficiently high μ, where α_s is sufficiently small, physics quantities, such as cross sections, can be calculated to a truncated series, known as *Leading Order* (LO), *Next-to-Leading Order* (NLO) *etc.*. There are plenty of experiments on high energy processes which offer quantitative tests of pQCD. Due to the complexity of hadronic processes, the

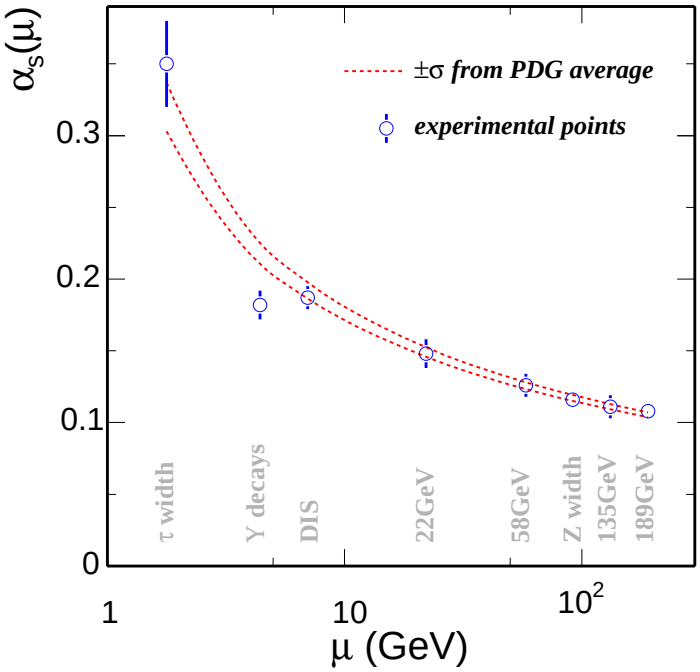

Figure 1.1: Measured QCD running coupling constant α_s from different experiments compared with Lattice QCD calculations.

test for pQCD has more difficulties than that for QED.

Assuming factorization, the cross section of a process $A + B \to C + ...$ can be written as:

$$\sigma_{AB\to C} = f_{a/A}(x_a, \mu_F^2) f_{b/B}(x_b, \mu_F^2) \otimes \hat{\sigma}_{ab\to c}(\hat{s}, \mu_F^2, \mu_R^2, \alpha_s) \otimes D_{c\to C}(z, \mu_F^2) \tag{1.2}$$

Only the middle term $\hat{\sigma}_{ab\to c}$ can be calculated in pQCD from Feynman diagrams. The first term $f_{a/A}(x_a, \mu_F^2)$ or $f_{b/B}(x_b, \mu_F^2)$ is the hadron *Parton Distribution Function* (PDF) and the last term $D_{c\to C}(z, \mu_F^2)$ is the *Fragmentation Function* (FF) that describes the transition from a parton to a hadron. For leptons, these two terms do not contribute in this formula. Hence, we can measure PDFs through lepton-nucleon DIS interactions and FFs through high energy e^+e^- collisions. μ_R is the renormalization scale, originating from the need to regularize divergent momentum integrals in calculating high order diagram loops. μ_F is the factorization scale, at which the parton densities are evaluated. $\hat{s}$ is the partonic center of mass energy squared. From this formula, we can see it is complicated

to determine the expected hadron production cross section in hadron-hadron collisions.

Heavy quark (c, b) production, due to large masses, is believed to match to pQCD prediction better than light quark production. And because they cannot be produced through the initial light hadron fragmentation, the FF part is irrelevant to the total production cross section of heavy quarks. Hence the measurement of the total heavy quark production cross section offers a powerful test of pQCD.

Let us take the calculation of heavy quark pair $Q\bar{Q}$ cross section in $p+p$ collisions as an example [Vog02]. At LO, heavy quarks are created by gg fusion and $q\bar{q}$ annihilation, while at NLO, qg and $\bar{q}g$ scattering is included. To any order, the partonic cross section can be calculated as an expansion in the power of α_s, assuming $\mu_R = \mu_F = \mu$:

$$\hat{\sigma}_{ij}(\hat{s}, m_Q^2, \mu^2) = \frac{\alpha_s^2(\mu)}{m^2} \sum_{k=0}^{\infty} (4\pi\alpha_s(\mu))^2 \sum_{l=0}^{k} f_{ij}^{(k,l)}(\eta) \ln^l(\frac{\mu^2}{m_Q^2}) \tag{1.3}$$

where $\eta = \hat{s}/4m_Q^2 - 1$ and $f_{ij}^{(k,l)}(\eta)$ is called the scaling function, obtained from the calculation of Feynman diagrams for each order. The total production cross section can be obtained from the above partonic cross section:

$$\sigma_{pp}(s, m_Q^2) = \sum_{i,j=q,\bar{q},g} \int_{\frac{4m_Q^2}{s}}^{1} \frac{d\tau}{\tau} \delta(x_i x_j - \tau) f_{i/p}(x_i, \mu^2) f_{j/p}(x_j, \mu^2) \hat{\sigma}_{ij}(\tau, m_Q^2, \mu^2) \tag{1.4}$$

Numerical results of theoretical calculations show strong dependence on the truncation of the series, the selection of parameters μ_F, μ_R and m_Q *etc.* [MNR93, Vog02, RP03]. Hence, theoretical predictions still have large uncertainties.

Experimentally, measurement of charmed hadrons is difficult due to their short lifetime ($c\tau(D^0) = 124$ μm), low production rates, and large combinatoric background. Both direct reconstruction through the hadronic channel and indirect measurement of the semi-leptonic decay of charmed hadrons were preformed in the previous measurements. In the low center-of-mass energies ($\lesssim$ 40 GeV), measurements were done on fixed targets [Tav87, Bar88, Amm88, Kod91, Alv96]. At $\sqrt{s} \sim 52 - 63$ GeV (ISR), the measurements were done from $D\Lambda_c$ production and ee, $e\mu$ pair correlation, and the results

showed inconsistency between different publications [Tav87]. At higher energies, the UA2 experiment measured single electron distributions at 630 GeV $p + \bar{p}$ collisions [Bot90]. However, due to large uncertainties of the decay from charmed hadron to electrons, these measurements included large errors. The CDF II collaboration made a direct measurement of open charm hadrons at $\sqrt{s} = 1.96$ TeV $p+p$ collisions [Aco03], but the spectrum only covers the high p_T region. Recent pQCD calculations seem to reproduce the spectrum at CDF. No charm measurement in elementary $p + p$ collisions at RHIC energy was done and theoretical predictions differ significantly at this energy due to the large uncertainties of many parameters. So charm production at the baseline elementary $p+p$ collisions at RHIC energy is helpful.

1.1.3 Confinement and chiral symmetry breaking

Since quarks have color quanta, while hadrons are color-neutral to us, quarks must be confined within hadrons. This can also be explained from the QCD coupling α_s. When two quarks are separated to a large distance, which corresponds to a small energy scale, the coupling becomes strong, *i.e.* intuitively, more and more self-coupled gluons hold the quarks not to be isolated. It is quite different in QED because there is no self coupling between photons, so that we can observe isolated electric charges.

In the absence of quark masses, the QCD Lagrangian can be split into two independent sectors: the left- and right-handed components [Pic95]. This Lagrangian is invariant under chiral symmetry transformations then. This symmetry, which is the extension of classical $SU(3)$, is a global $SU_L(n_f) \times SU_R(n_f)$ symmetry for n_f massless quark flavors. However, it is spontaneously broken in the vacuum in the Nambu-Goldstone's way to realize this symmetry and this breaking gives rise to $(n_f^2 - 1)$ massless Goldstone particles. Thus we can identify the π, K, η with the Goldstone modes of QCD: their small masses being generated by the quark-mass matrix which explicitly breaks the global chiral symmetry of the QCD Lagrangian[2].

[2]See Appendix A for chiral symmetry and effective lagrangian approach.

1.1.4 QCD Phase transition

QCD matter is mostly observed as nuclei or hadron gas in our current condition. With sufficient temperature and energy density, QCD predicts a phase transition to a new matter, named *Quark Gluon Plasma* (QGP), with new (color) *degrees of freedom* (d.o.f.). In this new phase, quarks and gluons are liberated from hadrons, and can move around in a larger distance rather than confined in hadrons, which is called *deconfinement*. Meanwhile, the broken chiral symmetry in normal QCD matter will be restored and consequently, masses of scalar mesons and vector mesons will decrease [Kar02a]. Lattice QCD calculations provide quantitative predictions on this phase transition: the critical temperature of this phase transition is $T_c \sim 150-180$ MeV, and the energy density at the critical point is $\varepsilon_c(T_c) \sim 1-3$ GeV/fm^3 (~ 0.17 GeV/fm^3 for nuclear matter) [Kar02b]. The appearance of these color d.o.f. can be illustrated by a sharp increase in pressure with temperature, shown in Fig. 1.2 [KLP00].

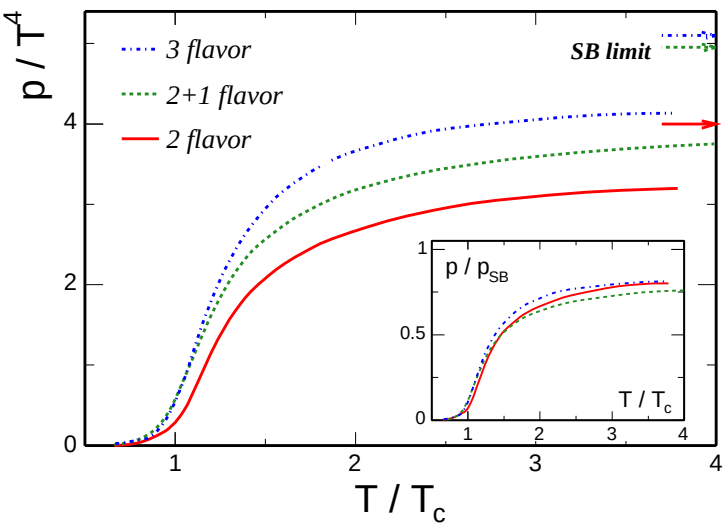

Figure 1.2: The evolution of p/T^4 with the increase of temperature T for 3 different flavor configurations. The arrows indicate the SB limit for each case. The insert plot shows the ratio of p/p_{SB} with function of T.

The arrows indicate the Stefan-Boltzmann limits, which are for the systems with massless, non-interacting quarks and gluons. The similarity of the three curves in the insert plot of Fig. 1.2 illustrates that besides the effect of quark masses, there should be interactions in the newly formed system, which is different from the original QGP

scenario (weakly interacting), but is already demonstrated by experimental results (see next section).

Lattice QCD calculations of the potential between two heavy-mass quarks also offer evidence of deconfinement.

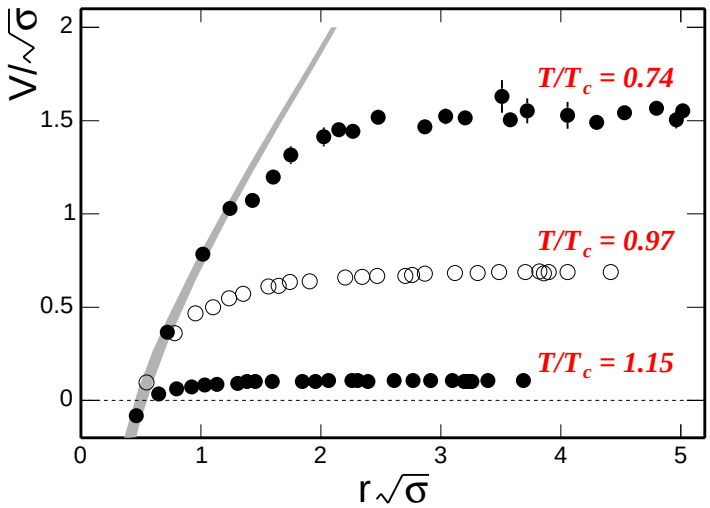

Figure 1.3: Lattice calculations for the heavy-mass quark potential in different temperature cases. The band depicts the Cornell potential of $V(r) = -\alpha/r + \sigma r$ with $\alpha = 0.25 \pm 0.05$.

Fig. 1.3 shows a recent calculation of the heavy-mass quark-antiquark pair Cornell potential in different temperature conditions [KLP00]: with the increase of temperature, the rampart of the potential between two quarks, which causes confinement, will bend down and thus liberate quarks from the trap. In addition, the continuous bending without sudden change indicates a crossover transition at high temperature and vanishing net quark density.

1.2 Heavy Ion Collisions

Experimentally, to search for this new kind of matter, a large amount of energy needs to be packed into a limited space volume. Heavy ion collisions have been proposed as a more effective way because the initial energy density increases as a power law function with the atomic number while only logarithmically with collision energy [Lin96]. Since

the 1970's, physicists from BEVALAC at LBL, SIS at GSI, AGS at BNL, SPS at CERN and RHIC at BNL *etc* [Sto04] have been trying to reach and cross the phase transition boundary in the laboratory through relativistic heavy ion collisions.

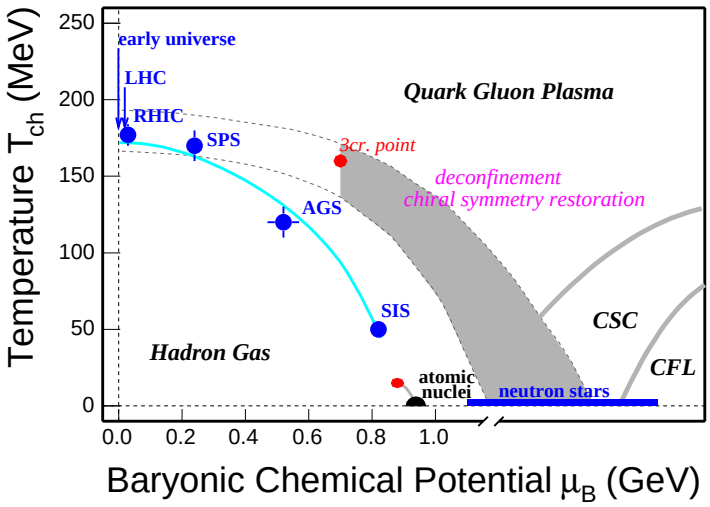

Figure 1.4: QCD phase diagram. The grey shadows depict first-order phase transition boundaries. The red dots depict the critical points and "3cr point" is calculated from Lattice QCD [FK02]. The blue dots depict the positions of several colliders from statistical fit [Bra01].

Fig. 1.4 shows the QCD phase diagram and approaching transition boundary of the colliders.

For the past four years the *Relativistic Heavy Ion Collider* (RHIC) at *Brookhaven National Lab* (BNL) has conducted very successful runs. Plenty of exciting physics results reveal that the matter created at RHIC is quite different from what we observed before: It cannot be described by hadronic degrees of freedom and demonstrates many of the signatures from a QGP scenario. These measurements provide strong hints for the discovery of QGP [Adc04]. Some of the key measurements will be discussed in the following sections[3].

[3]Useful kinematic variables are defined in Appendix B.

1.2.1 Nucleon stopping power and initial energy density

One of the most fundamental quantities we need to investigate is whether the initial deposited energy is enough to cross the energy density threshold for QGP formation. Because baryon number is conserved and the rapidity distributions are only slightly affected by rescattering in the late stage of collisions, the measured net baryon $(B - \bar{B})$ distribution can reveal the energy loss of initial participants and allow us to estimate the degree of nucleon stopping power. Fig. 1.5 shows rapidity loss $\langle \delta y \rangle = \langle y \rangle - y_p$ for different energies from AGS to RHIC [Bea04]. Using the data point at RHIC, one can estimate that $73 \pm 6^{+12}_{-26}$ GeV of the initial 100 GeV per participant is deposited and available for excitations.

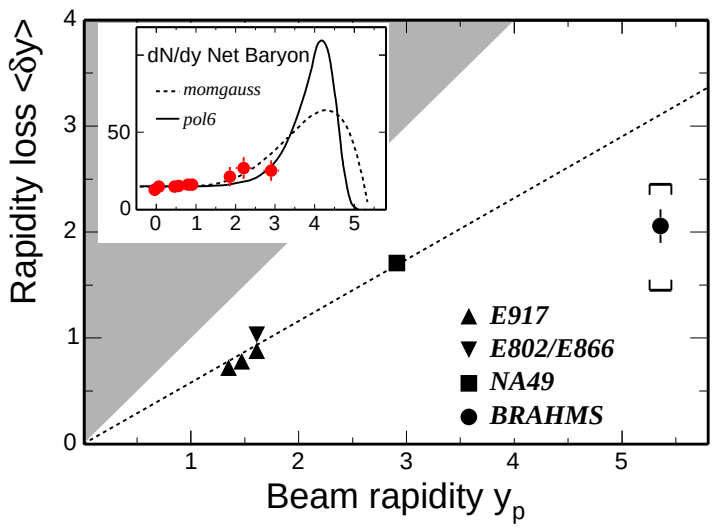

Figure 1.5: The rapidity loss as a function of beam rapidity. The shadow indicates an unphysical region and the dashed line depicts the phenomenological scaling $\langle \delta y \rangle = 0.58 y_p$. The insert plot shows the measured data points of net baryon distribution from BRAHMS and different extrapolations to full rapidity.

The initial Bjorken energy density [Bjo83] can be calculated using:

$$\epsilon_{Bj} = \frac{1}{A_\perp \tau} \frac{dE_T}{dy} \tag{1.5}$$

where τ is the formation time and $A_\perp$ is the nuclei transverse overlap region area. The PHENIX dE_T/dy measurement [Adl04a] indicates an initial energy density of ~ 5

GeV/fm^3 ($\tau \approx 1$ fm/c, $A_\perp = \pi R^2$, $R \approx 1.2A^{1/3}$ fm) for central Au + Au collisions at RHIC, well above the expected critical energy density $\epsilon_c \sim 1$ GeV/fm^3.

Thus, the initial condition in Au + Au collisions at RHIC is believed to be capable of forming the new partonic matter - QGP.

1.2.2 Jet quenching

In heavy ion collisions, high p_T ($p_T >\sim 5$ GeV/c) particles are believed to be produced mainly from the initial QCD hard-scattering processes [Adl02a]. These energetic particles can be used as unique probes by studying their interactions with the medium. Experimentally, the nuclear modification factor, the difference between the spectrum in A+B collisions *with respect to* (w.r.t.) a $p+p$ collision reference, is extensively used. It is defined as:

$$R_{AB}(p_T) = \frac{d^2N_{AB}/dp_T dy}{T_{AB} d^2\sigma_{pp}/dp_T dy} \tag{1.6}$$

where $T_{AB} = \langle N_{bin}\rangle/\sigma_{pp}^{inel}$ is the nucleus overlap function, calculated from a Glauber model [Won94]. N_{bin} represents the number of binary collisions in a nucleus-nucleus collision. The experimental result [Ada03b] in Fig. 1.6 shows that there is a strong suppression relative to the binary scaling expectation at high p_T in the central Au + Au collisions − jet quenching. But this suppression is not seen in d + Au collisions, the control experiment, which suggests the suppression in central Au + Au is due to the final state interactions rather than initial state effect and thus a very dense matter must be created in central Au + Au collisions at RHIC.

This result has also been illustrated by a dihadron azimuthal angle correlation study. Fig. 1.7 shows the associated hadrons ($p_T > 2$ GeV/c) azimuthal distribution relative to a triggered hadron ($p_T > 4$ GeV/c). The enhanced correlation at $\Delta\phi \sim 0$, which means the pair is from a single jet, was observed in $p+p$, d + Au and Au + Au collisions. The pair from the back-to-back jet correlation at $\Delta\phi \sim \pi$ only appears in $p+p$ and d + Au while it almost completely disappears in central Au + Au collisions.

Due to momentum conservation, the disappearance of away-side fast partons must

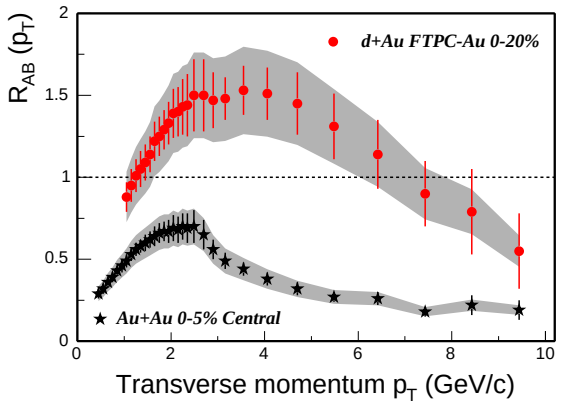

Figure 1.6: Nuclear modification factor in central Au + Au and d + Au collisions.

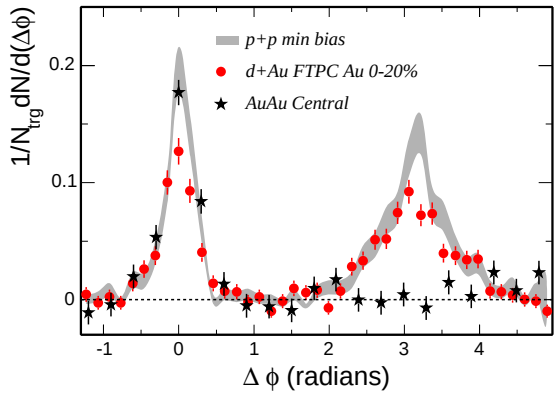

Figure 1.7: Dihadron azimuthal angle correlation at high p_T in $p+p$, d + Au and Au + Au collisions.

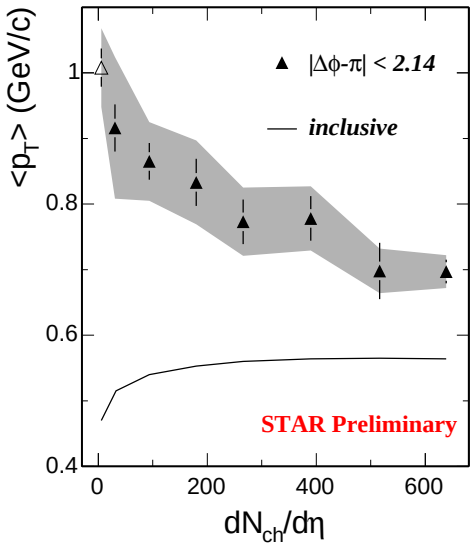

Figure 1.8: The $\langle p_T \rangle$ of away side jet evolves with the change of multiplicities in $p+p$ (open triangle) and Au + Au (solid triangles) collisions.

result in an excess of softer emerging hadrons. Fig. 1.8 shows the centrality dependence of the $\langle p_T \rangle$ of the associated away-side charged hadrons (threshold lowered to 0.15 GeV/c), compared with that of inclusive hadrons, illustrating the above point [Wan04]. This also offers a hint of the attainment of thermalization via the frequent soft parton-parton interactions in the early collision stages. But how strong those partons interact is still a crucial open question, that needs to be answered quantitatively to address the evidence of early thermalization of the system.

1.2.3 Collective motion

Hadron spectra are useful tools to study the properties of the bulk system and specified particles can be used to probe different stages after the heavy ion collisions. Fig. 1.9 shows the identified particle p_T spectra measured in central Au+Au collisions [Ada04a, Ada04b, Ada04c, Cas04].

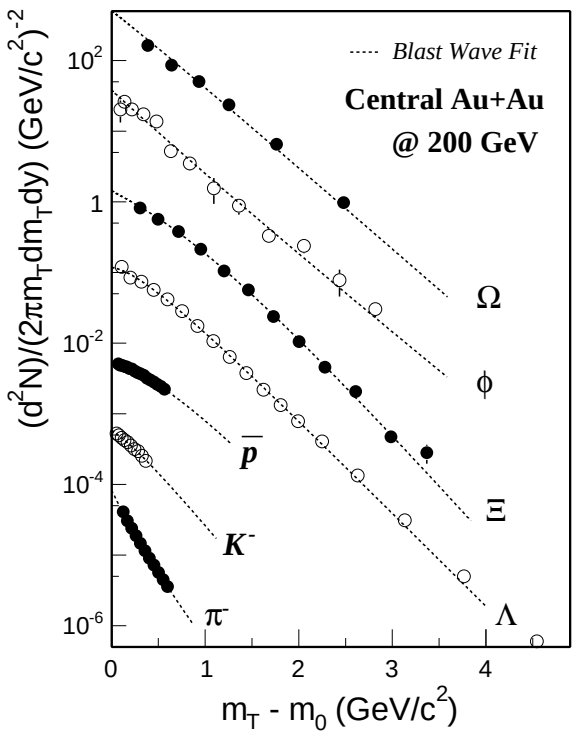

Figure 1.9: Identified particle spectra in central Au+Au collisions at $\sqrt{s_{NN}} = 200$ GeV and the Blast Wave fit results. The BW fits were done for π^-, K^-, $\bar{p}$ simultaneously and for other particles separately.

The plot shows the slopes of particle spectra changes for different particles (masses), indicating the strong collectivity of final state particles. The dashed lines depict the fit results from the Blast Wave thermal model [SSH93]. In thermal models, local thermal equilibrium is assumed and hence particles spectra only depend on the mass of particles and the temperature of system. "Blast wave" means that particles freeze out from the system surface simultaneously when dense matter becomes dilute enough. Under the assumption of simple cylindrical source and boost invariance in rapidity, there are only two parameters to describe the particles spectra: freeze-out temperature T_{fo} and average transverse velocity $\langle\beta_T\rangle$. Fig. 1.10 shows the fit results for different particles. For the simultaneous fit to π^-, K^-, $\bar{p}$, stronger and stronger collectivity is observed from peripheral to central collisions. But the fit to Ω and ϕ in central Au + Au collisions shows higher freeze-out temperature and lower transverse velocity, indicating those particles leave the system at the earlier stage than stable hadrons. This is not surprising since those multi-strange baryons/mesons are expected to have much smaller hadronic scattering cross sections and thus the temperature from the fit to those particles may reflect the chemical freeze-out temperature T_{ch}. This temperature is close to the critical temperature T_c, meaning the temperature of the system created in the collisions is greater than T_c and hence the phase transition may take place at RHIC energy.

1.2.4 Transverse azimuthal anisotropy

In non-central heavy ion collisions, the overlapping region of the two nuclei will form an anisotropy in coordinate space. Because of rescattering, the anisotropic pressure gradient will lead to an anisotropy in momentum space. The dynamic expansion of the system will wash out the coordinate-space-anisotropy, while the momentum-space-anisotropy will saturate during the evolution of the system [KH03]. The final state particle spectrum in

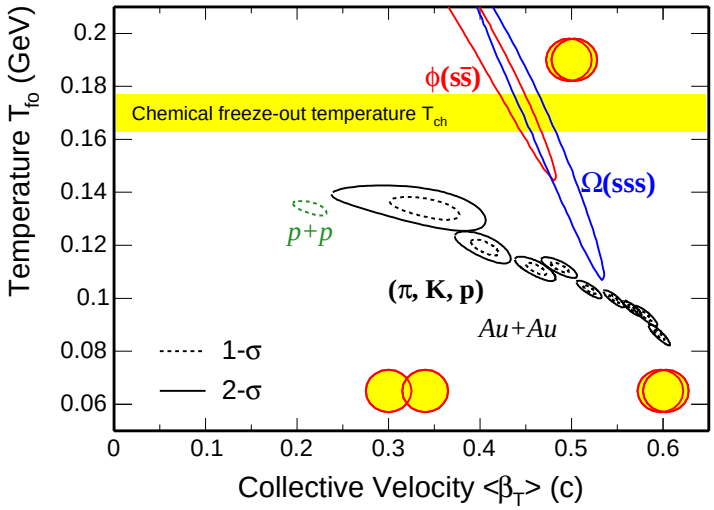

Figure 1.10: Blast-wave parameters T_{fo} vs. $\langle\beta_T\rangle$ contour plot from the simultaneous fits to stable hadrons (π, K, p) spectra in Au + Au collisions and $p+p$ collisions and separate fits to multi-strange hadrons $\phi(s\bar{s})$, $\Omega(sss)$ spectra in central Au + Au collisions. The contours of π, K, p fits in Au + Au are for peripheral collisions in the left and central collisions in the right. The contours of ϕ and Ω are for central Au + Au collisions.

momentum space can be expanded into a Fourier series as Eq. 1.7.

$$E\frac{d^3N}{dp^3} = \frac{d^2N}{2\pi p_T dp_T dy}(1 + \sum_{n=1}^{\infty} 2v_n cos[n(\phi - \Psi_{rp})]) \tag{1.7a}$$

$$v_n = \langle cos[n(\phi - \Psi_{rp})]\rangle \tag{1.7b}$$

where Ψ_{rp} denotes the direction of the reaction plane. The first and second harmonic coefficients v_1, v_2 are called directed and elliptic flow. Due to the approximate elliptic shape of the overlapping region, the elliptic flow v_2 is the largest harmonic observed in mid-rapidity. Because of the quenching of coordinate-space-anisotropy, elliptic flow can reveal early information about the system and because it depends on rescattering, elliptic flow is sensitive to the degree of thermalization of the system in the early stage.

Fig. 1.11 shows identified particle $v_2(p_T)$ and the hydrodynamic model predictions for $p_T < 2$ GeV/c [Ada05]. In this low p_T region, v_2 has larger values for lower mass particles. This mass ordering is reasonably described by the hydrodynamic models, which assume ideal relativistic fluid flow and negligible relaxation time compared to the time scale of the

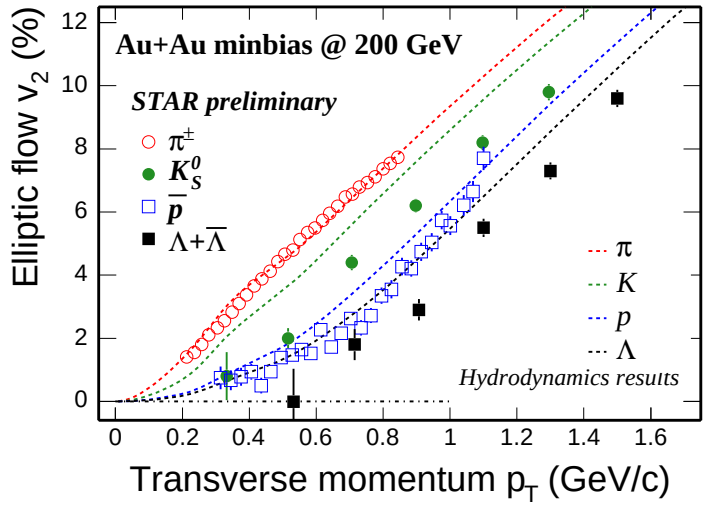

Figure 1.11: Elliptic flow v_2 of identified particles as a function of p_T at low p_T region compared with hydrodynamic model predictions.

equilibrated system. The agreement implies early thermalization, *i.e.* strongly interacting matter with a very short mean free path dominates the early stages of the collisions.

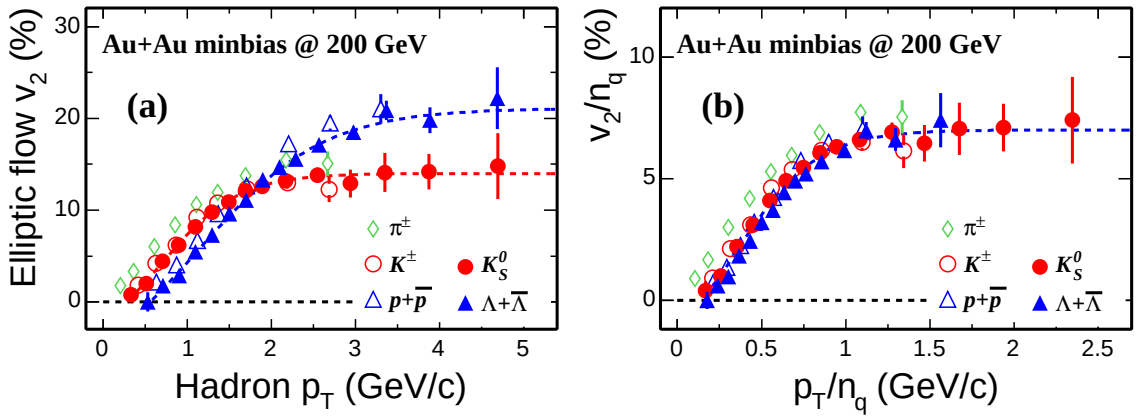

Figure 1.12: Left: Identified particle v_2 up to intermediate p_T . Right: After scaling the v_2 and p_T with number of constituent quarks n_q, all particles fall onto one universal curve at $p_T/n_q > 0.6$ GeV/c.

Fig. 1.12 shows $v_2(p_T)$ in a larger p_T range for different particles [Adl03a, Ada04b]. v_2 for all particles saturates above a certain p_T ($\sim 2-3$ GeV/c). On the left panel, in addition, particles show two groups on the plots: mesons and baryons. After scaling both v_2 and p_T with *the Number of the Constituent Quarks* (NCQ) in the corresponding hadron, all particles with $p_T/n_q > 0.6$ GeV/c fall onto one universal curve except pions (due to

resonance decay effect [GK04, DES04]), shown on the right panel. This meson/baryon grouping phenomenon was also observed in the nuclear modification factor R_{CP} at intermediate p_T ($1.5 < p_T/(\mathrm{GeV/c}) < 5$) [Ada04b]. Coalescence models [LK02, MV03] which assume hadrons are formed through coalescing of constituent quarks provide a viable explanation for these observations. This indicates the flow developed during a sub-hadronic (partonic) epoch, and offers a strong evidence of deconfinement at RHIC.

1.2.5 Heavy flavor production in HIC

Heavy flavor hadrons are expected to be unique tools to probe the early stage information in heavy ion collisions due to the following features. The creation of heavy flavor quarks is dominated by the initial gluon fusion processes and is negligible in the pre-equilibrium stage [Lin96]. Systematic studies of charm production in $p + p$, and p + A collisions have been proposed as a sensitive way to measure the PDF in the nucleon, and the nuclear shadowing effect [LG96]. Due to their heavy masses, energetic heavy flavor partons are expected to lose less energy than light quarks from gluon radiations when traversing the dense medium ("dead-cone" effect) [DK01]. At RHIC energies, due to the possible large production of charm quarks, coalescence processes might not be negligible, especially for closed charm production, indicating the standard J/ψ suppression scenario might be invisible [GR01, TSR01, GKL02, ABR03]. Recent studies propose that charm quark flow not only offers a check of hydrodynamic models and/or coalescence models, but also could imply the thermalization of the light quarks in the system [DES04, BKG03, GKR04].

Theoretically, there are lots of calculations of heavy quark energy loss [DG04], nuclear shadowing [LG96], cronin enhancement [Vog03], charmonium production [NLC03] and charm quark flow [LM03, BCS04] *etc.* for the collisions at RHIC. However, we have very few experimental results to test or prove these features so far. The first publication of charm production at RHIC energy was a single-electron measurement by the PHENIX collaboration at $\sqrt{s_{NN}} = 130$ GeV in Au + Au collisions [Adc02]. They claimed that

charm production in heavy ion collisions obeys the number of binary collisions scaling and the spectrum is consistent with PYTHIA [Sj01] (pQCD) calculations. Both direct reconstruction and indirect semi-leptonic decay electron measurements (spectrum and elliptic flow) at top RHIC energy offer us an opportunity to understand not only pQCD, but also the early stage features of the matter created in heavy ion collisions.

1.2.6 What have we learned so far?

So what is happening after heavy ions collide? Fig. 1.13 is a cartoon showing the evolution of excitation energy E^* (represented as temperature T for a thermally equilibrated system) and the particles being created and decoupling from the system. There is no absolute scale on the plot because we don't know most of these variables yet.

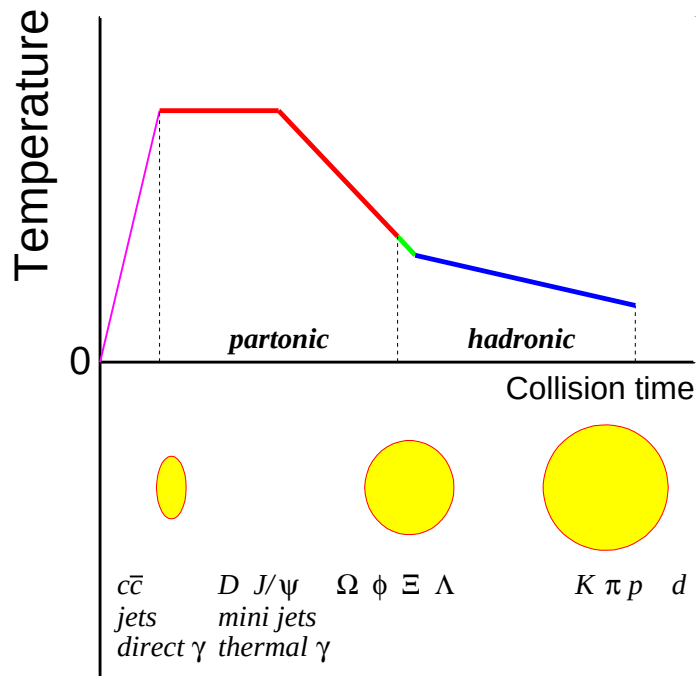

Figure 1.13: A time scale plot to show the evolution of the created matter. The several ellipses depict the system shape during evolution. And creation and decoupling of different identified particles are also shown on the plot.

At RHIC, after two heavy nuclei collide, plenty of energy ($\sim$ 70% of the initial energy per participant [Bea04]) is deposited into a compact overlap region suddenly. The initial Bjorken energy density is well above the critical energy density for a phase tran-

sition [Adl04a]. Those particles from hard processes (such as jets and heavy quarks) as well as direct photons ($qg \rightarrow q\gamma$, $q\bar{q} \rightarrow g\gamma$) are created in these initial collisions. The overlap region is an ellipse in coordinate space. Then rescatterrings between components in the system make the system expand and approach thermal equilibrium. Soft mini-jets ($p_T <\sim 2$ GeV/c) are created abundantly. The anisotropy in coordinate space quenches due to the expansion, but the anisotropy in momentum space saturates quickly during this stage [KH03]. The system will sooner or later reach its maximum temperature, and the matter at this stage is expected to have the partonic *d.o.f.* equation of state. Fast partons traversing through this hot dense matter will lose large amounts of their energy (jet quenching). Meanwhile, particles (photons, leptons, g, u, d, s, but very small fraction of heavy quarks) with relative small masses are produced thermally in this stage. With the continuous expansion of the system, the temperature starts to drop, the matter becomes more and more dilute and those partonic components begin to hadronize from the system either through coalescence or fragmentation. In the stage after hadronization, hadrons keep rescatterring between each other and fractions between different hadrons are still varying. During this stage, some hadrons with small scattering cross sections start to freeze out from the system with fixed momentum such as charm hadrons (D, J/ψ), multi-strange hadrons (Ω, ϕ, Ξ). Then the system becomes dilute enough that there is no inelastic scattering between different hadrons and the fractions of different hadrons are stable. This point is called chemical freeze-out. Some hadrons (π, K, $p(\bar{p})$) in the system keep scattering elastically and finally all particles freeze out from the system with each particle having stable momentum. This is called kinetic freeze-out.

In heavy ion collisions, what we want to study ultimately is the equilibrated matter with partonic *d.o.f.*. Multi-strange hadrons, and more early freeze-out charm hadrons are ideal probes to illustrate the properties of this matter created in collisions. Based on the knowledge we have learned from three years of RHIC runs, we need these probes to answer the questions: whether the partonic matter is locally thermalized or not, and if yes, what are its thermal and symmetry properties?

CHAPTER 2

Experimental Set-up

2.1 RHIC accelerator

The Relativistic Heavy Ion Collider (RHIC) at Brookhaven National Laboratory (BNL) is designed to accelerate and collide heavy ions and polarized protons with high luminosity, allowing physicists to explore the strong interaction through many extensive and intensive measurements. It is the first facility to collide heavy ion beams and the top center-of-mass collision energy is 200 GeV per nucleon pair, which is about more than 10 times greater than the highest energy reached at previous fixed target experiments. The purpose of this extraordinary new accelerator is to seek out and explore new high-energy forms of matter and thus continue the centuries-old quest to understand the nature and origins of matter at its most basic level. RHIC is also delivering polarized proton beams up to center-of-mass energy 500 GeV to carry on vigorous spin scientific programs.

Fig. 2.1 shows a diagram of the RHIC machine complex, including a Van de Graaff facility, a linear proton accelerator, the booster synchrotron, the Alternative Gradient Synchrotron (AGS), and ultimately the RHIC synchrotron ring. For Au beam operations, the Au ions with charge $Q = -1e$ are created using the Pulsed Sputter Ion Source. Then they are accelerated through the Van de Graaff facility and a series of stripping foils, and the Au ions at the exit are with a kinetic energy of 1 MeV/nucleon and a net charge of $Q = +32e$. The ions are then injected into the booster synchrotron and accelerated to an energy of 95 MeV/nucleon. After the Au ions leave the booster, they are further stripped to $Q = +77e$ and transferred into the AGS, where they are accelerated to 8.86 GeV/nucleon and sorted into four final bunches. Finally, the ions are injected into RHIC

and stripped to the bare charge state of $Q = +79e$ during the transfer. For p+p operations, protons are injected from the 200 MeV Linac into the booster, followed by acceleration in the AGS and injection into RHIC.

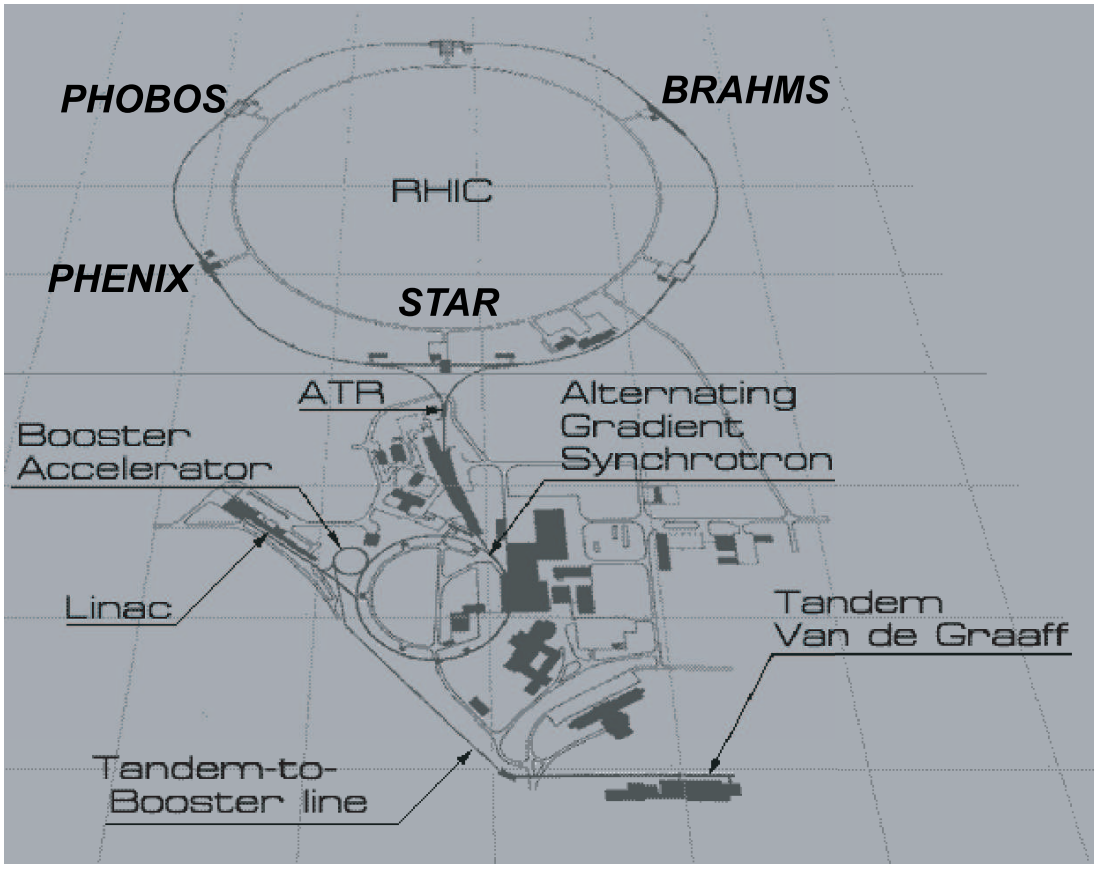

Figure 2.1: Schematic of the RHIC complex. RHIC's two 3.8-kilometer rings collide relativistic heavy ions and polarized protons at six intersection points.

RHIC consists of two concentric super-conducting storage rings that are called blue and yellow rings, respectively. Each ring has its own dependent set of bending and focusing magnets as well as ratio frequency cavities, but both share a common horizontal plane in the tunnel. The rings have six interaction points, and 4 of them are equipped with detectors. They are two large experiments STAR (6 o'clock), PHENIX (8 o'clock) and two small ones PHOBOS (10 o'clock) and BRAHMS (2 o'clock), respectively.

To date, RHIC has been run in p+p , d + Au , Au + Au and Cu + Cu configurations.

2.2 STAR detector

The Solenoidal Tracker at RHIC (STAR) is a specially designed detector to track thousands of particles simultaneously produced by each ion collision at RHIC. It has an azimuthal symmetric acceptance and covers large range around mid-rapidity. STAR consists of several subsystems and a main tracker - the *Time Projection Chamber* (TPC) located in a homogenous solenoidal analyzing magnet.

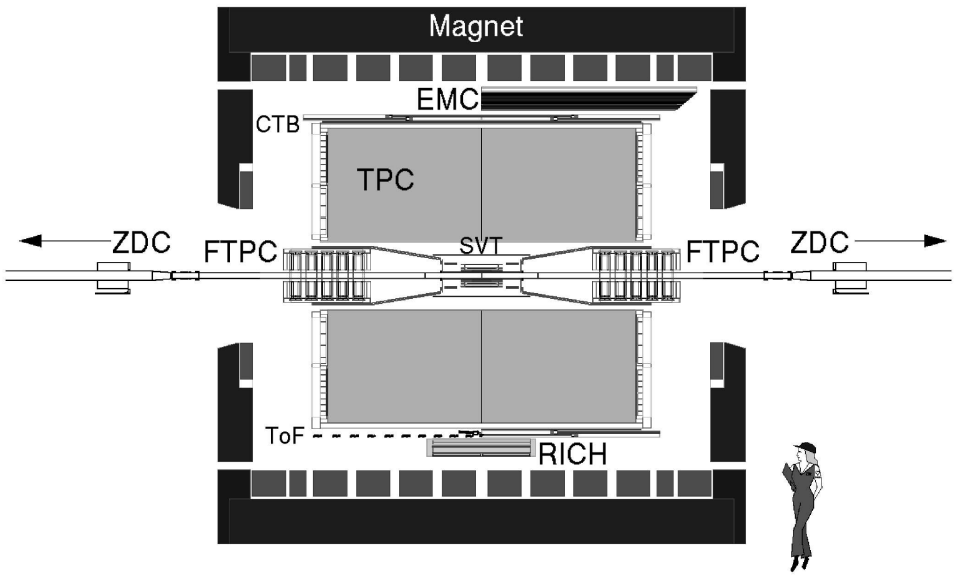

Figure 2.2: Cutaway view of the STAR detector. It includes the partial installed ElectroMagnetic Calorimeter (EMC) and two prototypes Time-of-Flight (TOF) detectors.

Fig. 2.2 shows the cutaway view of the STAR detector. The main tracker - TPC covers the $|\eta| < 1.5$ and 2π in azimuth. The details of TPC detector will be discussed in the next section. There are inner detectors *Silicon Vertex Tracker* (SVT) and *Silicon Strip Detector* (SSD) close to the beam pipe, which provides additional high precision space points on track so that it improves the position resolution and allows us to reconstruct the secondary vertex of weak decay particles. There are two *Forward TPC* (FTPC) detectors covering $2.8 < |\eta| < 3.8$ to track particles at forward and backward rapidity. One prototype tray of *Time-Of-Flight* (TOF) detector using scintillator materials (TOFp) was installed since Run II and another prototype tray of TOF detector using *Multigap Resistive Plate*

Chamber (MRPC) technology (TOFr) was installed since Run III. Each replaces one *Central Trigger Barrel* (CTB) tray (120 in total) surrounding TPC. They are used to test the performance of upcoming full barrel TOF detector upgrade which is expected to extend the PID capability of STAR greatly. Part of barrel *ElectronMagnetic Calorimeter* (EMC) was also installed since Run II. They are used to measure the electromagnetic probes - electrons and photons.

There are some main trigger detectors: *Zero Degree Calorimeter* (ZDC), CTB and *Beam-Beam Counters* (BBC). Two ZDCs locates on each side $\sim$ 18 m away from the collision points. Each is centered at 0° and covers $\sim$ 2.5 mrad. The ZDCs are hadronic calorimeters to detect the outgoing neutrons. They are put beyond the dipole magnets which bend away the charged fragments. The ZDC signals are used for monitoring the heavy ion beam luminosity and for the experiments triggers. The CTB is a collection of scintillating tiles covering the whole barrel ektexine of the TPC. The CTB will be mostly used to select central triggered events in heavy ion collisions by measuring the occupancy of those CTB slats. The BBC subsystem covers $3.3 < |\eta| < 5.0$, measuring the "beam-jets" at high rapidity from *Non-Singly Diffractive* (NSD) inelastic $p + p$ interactions. It consists of two disk shaped scintillating detectors, with one placed at each endcap of the TPC (3.5 m from TPC center). Each BBC disk is composed of scintillating tiles that are arranged in a hexagonal closest packing. The $p+p$ NSD trigger sums the output of all tiles on each BBC and requires a coincidence of both BBC's firing above noise threshold within a time window. Some other detectors are used for special triggers, *e.g. pseudo Vertex Position Detectors* (pVPDs) are used for TOF triggered events (this will be discussed in the following section), and EMC is used to trigger on high p_T particle events *etc.*

The STAR magnet is cylindrical in design with a length of 6.85 m and has inner and outer diameters of 5.27 m and 7.32 m, respectively. It generates a field along the length of the cylinder having a maximum of $|B_z| = 0.5$ T. It allows the tracking detectors to measure the helical trajectory of charged particles to get their momenta. To date, the STAR magnet has been run in full field, reversed full field and half filed configurations.

2.3 Main tracker - TPC

TPC is the "heart" of the STAR detector [And03]. Consisting of a 4.2 m long cylinder with 4.0 m in diameter, it is the largest single TPC in the world. The cylinder is concentric with the beam pipe, and the inner and outer radii of the active volume are 0.5 m and 2.0 m, respectively. It can measure charged particles within momentum $0.15 < p_T/(\mathrm{GeV/c}) < 30$ (0.075 GeV/c low limit for 0.25 T). The TPC covers the full region of azimuth ($0 < \phi < 2\pi$) and covers the pseodurapidity range of $|\eta| < 2$ for inner radius and $|\eta| < 1$ for outer radius. Fig. 2.3 shows a cutaway view of the structure of the TPC.

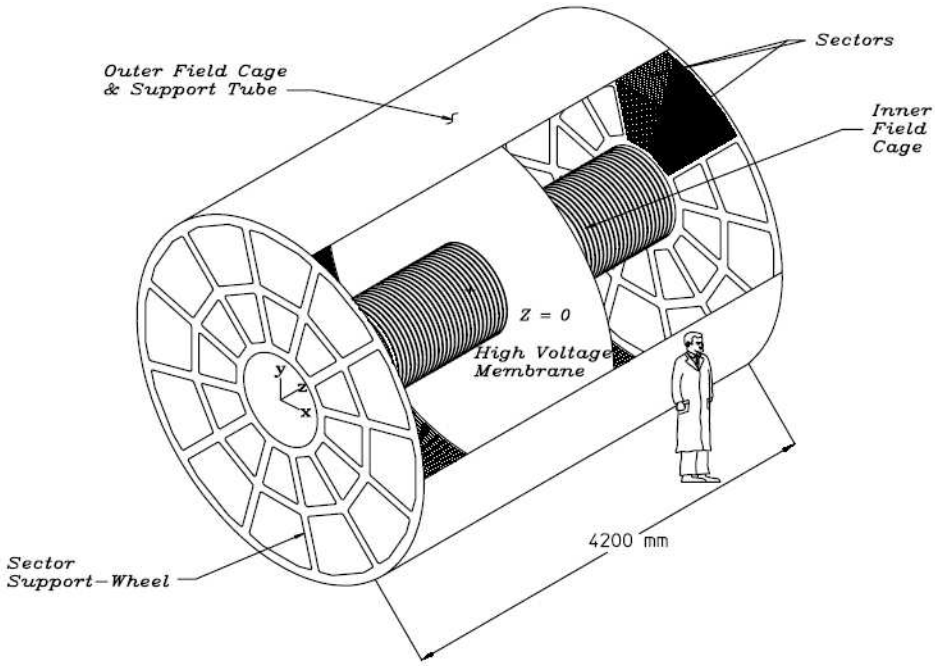

Figure 2.3: Cutaway view of the TPC detector at STAR.

The TPC is divided into two parts by the central membrane. It is typically held at 28 kV high voltage. A chain of 183 resistors and equipotential rings along the inner and outer field cage create a uniform drift filed ($\sim$ 135 V/cm) from the central membrane to the ground planes where anode wires and pad planes are organized into 12 sectors for each sub-volume of the TPC. The working gas of the TPC is two gas mixture − P10 (Ar 90% + CH_4 10%) regulated at 2 mbar above the atmospheric pressure. The electron drift velocity in P10 is relatively fast, $\sim$ 5.45 cm/μs at 130 V/cm drift field. The gas mixture

must satisfy multiple requirements and the gas gains are ~ 3770 and ~ 1230 for the inner and outer sectors working at normal anode voltages (1170 V for inner and 1390 V for outer), respectively. Each readout plane is instrumented with a thin *Multi-Wire Proportional Chamber* (MWPC) together with a pad chamber readout. Each pad plane is also divided into inner and outer sub-sectors, while the inner sub-sector is designed to handle high track density near collision vertex. 136,608 readout pads provide (x, y) coordinate information, while z coordinate is provided by 512 time buckets and the drift velocity. Typical resolution is $\sim 0.5 - 1.0$ mm.

When charged particles traverse the TPC, they liberate the electrons from the TPC gas due to the ionization energy loss (dE/dx). These electrons are drifted towards the end cap planes of the TPC. There the signal induced on a readout pad is amplified and integrated by a circuit containing a pre-amplifier and a shaper. Then it is digitalized and then transmitted over a set of optical fibers to STAR *Data AcQuisition system* (DAQ).

The TPC reconstruction process begins by the 3D coordinate space points finding. This step results in a collection of points reported in global Cartesian coordinates. The *Timing Projection chamber Tracker* (TPT) algorithm is then used to reconstruct tracks by helical trajectory fit. The resulted track collection from the TPC is combined with any other available tracking detector reconstruction results and then refit by application of a Kalman filter routine − a complete and robust statistical treatment. The primary collision vertex is then reconstructed from these global tracks and a refit on these tracks with the *distance of closest approach* (*dca*) less the 3 cm is preformed by a constrained Kalman fit that forces the track to originate from the primary vertex. The primary vertex resolution is ~ 350 μm with more than 1000 tracks. The refit results are stored as primary tracks collection in the container. The reconstruction efficiency including the detector acceptance for primary tracks depends on the particle type, track quality cuts, p_T , track multiplicity *etc.* The typical value for the primary pions with $N_{fit} > 24$ and $|\eta| < 0.7$, $dca < 3.0$ cm is approximate constant at $p_T > 0.4$ GeV/c: $>\sim 90\%$ for Au + Au peripheral collisions and $\sim 80\%$ for central collisions, respectively.

The TPC can also identify particles by the dE/dx of charged particles traversing the

TPC gas. The mean rate of dE/dx is given by the Bethe-Bloch equation 2.1 [Eid04]:

$$-\frac{dE}{dx} = Kz^2 \frac{Z}{A} \frac{1}{\beta^2} \left[\frac{1}{2} \ln \frac{2m_e c^2 \beta^2 \gamma^2 T_{max}}{I^2} - \beta^2 - \frac{\delta}{2} \right] \tag{2.1}$$

The meaning of each symbol can be referred to [Eid04]. Different types of particles (different rest masses) with the same momentum have different kinematic variables β (γ), which may result in distinguishable dE/dx. The typical resolution of dE/dx in Au + Au collisions is $\sim$ 8%, which makes the π/K separation up to $p \sim 0.7$ GeV/c and proton/meson separation up to $p \sim 1.1$ GeV/c.

A new recent technique was developed to identify high momentum ($p > 3$ GeV/c) pions and protons in the relativistic rising region of dE/dx [Xu04] benefiting from the advantage that the mean rates of dE/dx for different particles have a visible separation in the relativistic rising region ($\sim 2\sigma$ separation for pions and protons). Due to large acceptance of the TPC, using the topology of their weak decay in the TPC, the K^0_S, $\Lambda(\bar{\Lambda})$ *etc.* can be identified across p_T region $0.3 < p_T/(\text{GeV/c}) < 7.0$ (upper edge limited by statistics). Resonances (K^*, ϕ, Δ *etc.*) can be reconstructed through the event mixing technique [Adl02b]. Fig. 2.4 shows the PID capabilities up to date with the TPC. In addition, the TOF PID capability is also shown on the plot which will be discussed in the next section and the analysis part as well.

2.4 Prototype TOF detector

STAR has proposed the full barrel *Time-Of-Flight* (TOF) detector upgrade based on the *Multigap Resistive Plate Chamber* (MRPC) technology in the coming future. The TOFp detector (a prototype based on scintillator technology) was installed since Run II [Llo04]. It replaced one of CTB trays, covering $-1 < \eta < 0$, and $\pi/30$ in azimuth. It contains 41 scintillator slats with the signal read out by *Photo Multiplier Tubes* (PMTs). The resolution of TOFp is $\sim$ 85 ps in Au + Au collisions. However, due to the significant higher cost by the PMTs, this design will not be used in the full TOF upgrade.

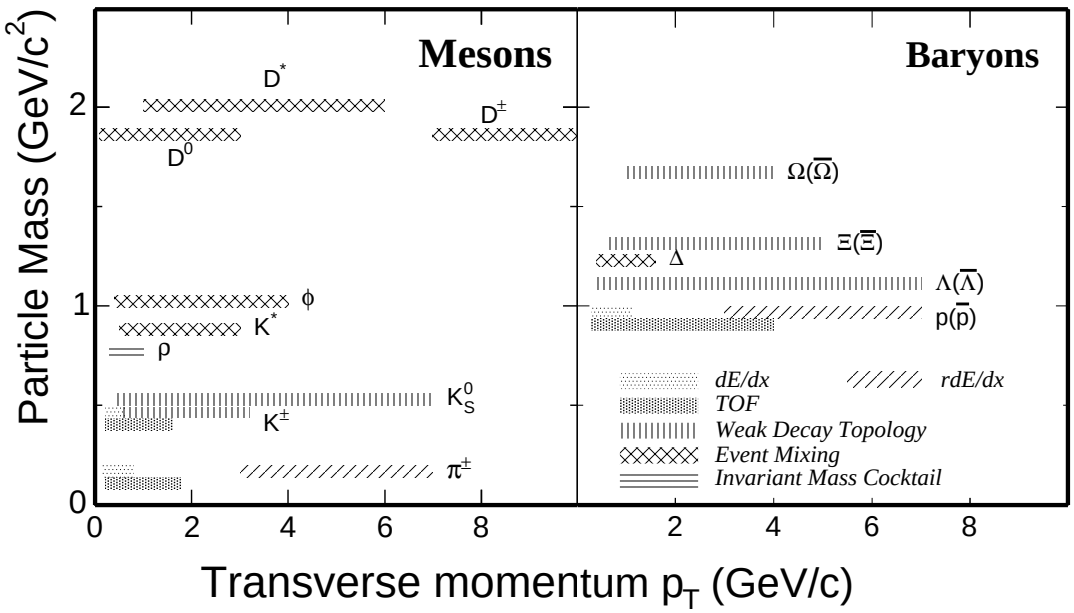

Figure 2.4: p_T reach of particle identification capability with STAR detectors for Run II and Run III configurations. The upper edges of rdE/dx, weak decay topology, event mixing are limited by statistics.

In Run III and Run IV, new prototypes of TOF detector based on MRPC (TOFr) were installed. Each also replaced one CTB tray, covering $-1 < \eta < 0$ and $\pi/30$ in azimuth too. In Run III, 28 MRPC modules were installed in the tray and 12 of them were equipped with electronics, corresponding to $\sim 0.3\%$ of the TPC acceptance [Ada03c]. In Run IV, 24 modules were installed in a new tray and the tray was put in the same position in STAR as Run III (but slightly global z position shift), but only 12 modules were equipped with valid electronics, which means the acceptance in Run IV was roughly similar to that in Run III.

Two pVPDs were installed as well since Run II to provide a starting time for TOF detectors, each staying 5.4 m away from the TPC center along the beam line [Llo04]. Each pVPD consists of three detecting element tubes covering $\sim 19\%$ of the total solid angle in $4.43 < |\eta| < 4.94$. Due to different multiplicities, the effective timing resolution of total starting time is 25 ps, 85 ps and 140 ps for 200 GeV Au + Au , d + Au and $p+p$ collisions, respectively.

MRPC technology was first developed by the CERN ALICE group. Fig. 2.5 shows

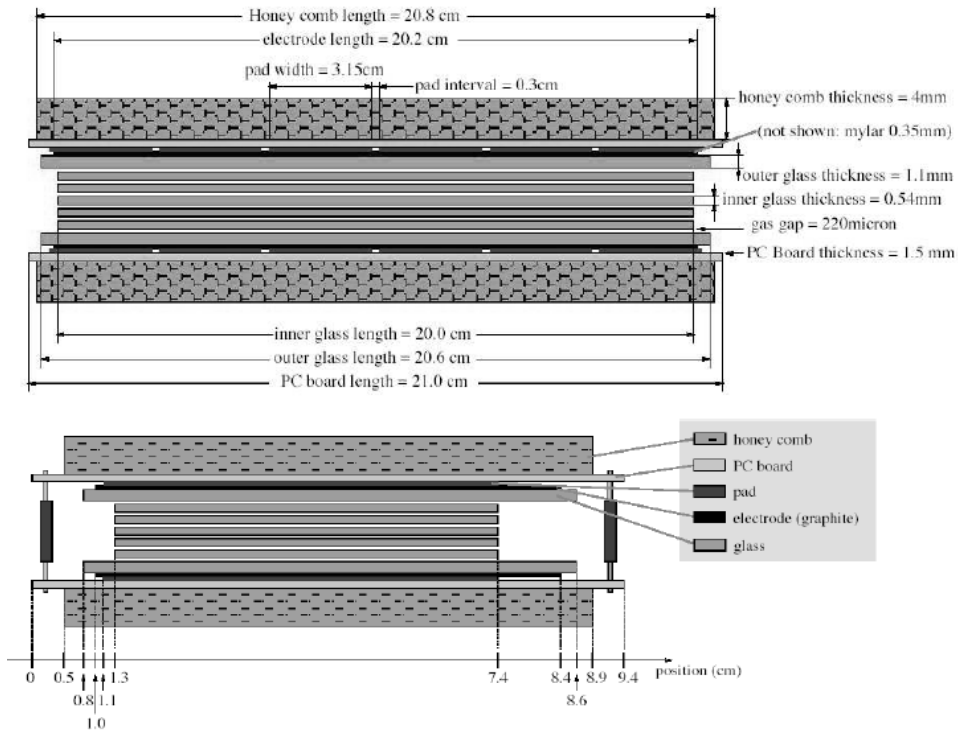

Figure 2.5: Two-side view of a MRPC module [Sha02].

Table 2.1: TOF system performance in Run III and Run IV

			Timing Resolution (ps)		
			pVPDs	TOFr system	TOFp system
Run III	d + Au @ 200 GeV		85	120 (85)†	100-140
	$p + p$ @ 200 GeV		140	160 (85)	N/A
Run IV	Au + Au @ 62.4 GeV		55	105 (89)	110 (95)
	Au + Au @ 200 GeV	FF/RFF, w/o E pVPD‡	40	95 (86)	96 (87)
		FF/RFF	27	86 (82)	92 (88)
		HF*	20	82 (80)	85 (83)

† numbers in the brackets are those for intrinsic TOFr/TOFp detector.
‡ east pVPD is not available for those runs from 5022001 to 5036000.
* HF - half field; FF - full field; RFF - reversed full field.

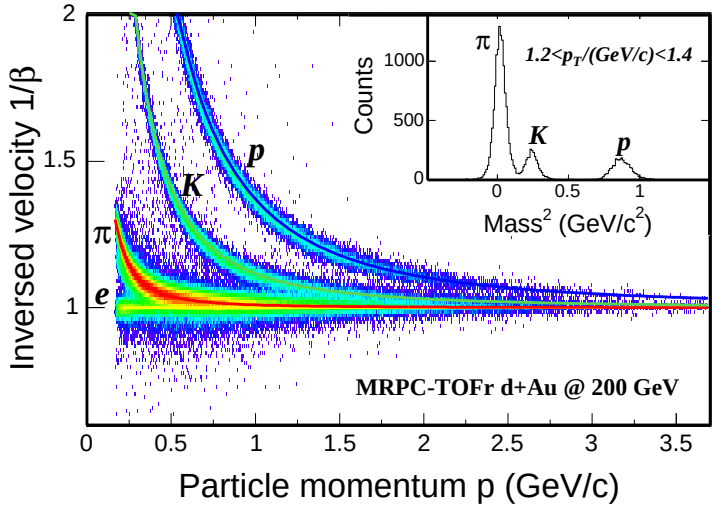

Figure 2.6: $1/\beta$ vs. momentum (p) from 200 GeV d + Au collisions. Separations between pions and kaons, protons and mesons are achieved up to $p_T \sim 1.6$ and ~ 3.0 GeV/c, respectively. The insert plot shows $m^2 = p^2(1/\beta^2 - 1)$ for $1.2 < p_T < 1.4$ Gev/c.

the two side views (long edge view on top and short edge view on bottom) of an MRPC module appropriate for STAR [Sha02]. An MRPC basically consists a stack of resistive plates with a series of uniform gas gaps. It works in avalanch mode. Electrodes are applied to the outer surface of the outer plates. With a strong electric field applied on, the internal plates are left electrically floating and they will keep the correct voltage due to the flow of electrons and ions created in avalanches. There are six read-out strips on each module in this design. The first beam test for 6-gap MRPCs at CERN PS-T10 facility with $p_{lab} = 7$ GeV/c pions beam resulted in a ~ 65 ps timing resolution with more than 95% detecting efficiency and the module is capable of working at high event rate (500 Hz/cm^2) [Sha02]. These modules were then assembled in a prototype TOF tray and tested in the AGS radiation area. Similar resolution was obtained. In RHIC Run III and Run IV, the MRPC modules in TOFr trays installed in the STAR detector were applied on the high voltage of 14 kV and with the working gas of 95% freon and 5% isobutane. The charged particle detecting efficiency is $> 95\%$ at high voltage plateau.

TOF system calibrations include the start time calibration from pVPDs and TOFr/TOFp flight time calibration. The main sources need to be considered are global time offset due to different electronics delays, the correlation between the amplitude and the timing

signals, the correlation between the hit position and the timing signals *etc.* Detailed calibrations on TOF systems can be found in [Rua04b, Ada03c] (TOFr) and [Llo04] (TOFp). Table. 2.1 lists the calibrated timing resolution results for TOFr and TOFp system in Run III and Run IV (Run IV 200 GeV Au + Au results are from test sample so far). The results show that the intrinsic timing resolution of TOFr was $\sim$ 85 ps and this performance was quite stable in two-year runs. Fig. 2.6 shows the hadron PID capability of TOFr system in 200 GeV d + Au collisions [Ada03c]. The performance of TOFr satisfied STAR TOF system upgrade requirements.

CHAPTER 3

Single electron transverse momentum distributions

Single lepton measurement has been proposed as a feasible and effective way to extract heavy flavor production since long time ago. Since the decay kinematics of heavy flavor hadrons to leptons is well known, the transverse momentum (p_T) distribution of single lepton can reveal that of heavy flavor hadrons. And furthermore, many topics may be carried on, such as total cross section, heavy quark fragmentation, heavy quark energy loss in medium in A + A collisions, *etc.* In this chapter, analysis details of single electron p_T distributions from 200 GeV d + Au , $p+p$ collisions and 62.4 GeV Au + Au collisions will be presented.

3.1 Single electrons from d + Au and $p+p$ collisions at $\sqrt{s_{NN}}$ = 200 GeV

3.1.1 Data sets and Trigger

In RHIC Run III, STAR detector has accumulated several data sets from d + Au and $p+p$ collisions at $\sqrt{s_{NN}} = 200$ GeV. Besides the *minimum bias* triggered data from d + Au collisions and the *Non Singly Diffractive* (NSD) collisions from $p+p$ collisions, special triggers were set up for TOFr detector data accumulation in both d + Au and $p+p$ collisions since TOFr detector has a relative very small acceptance. Table 3.1 lists all the data sets under the selections used in this analysis from Run III.

The d + Au minimum bias trigger required at least one beam-rapidity neutron in the ZDC in the Au beam outgoing direction, which is assigned negative pseudorapid-

Table 3.1: Data sets from Run III used in this analysis

Collision System	Trigger	Vertex Z Selection	Data Sample Size
d + Au	minbias	$\|V_Z\| < 30$ cm	6.42 M
	dAuTOF	$\|V_Z\| < 50$ cm	1.89 M
$p + p$	NSD	$\|V_Z\| < 30$ cm	4.35 M
	ppFPDTOFu	$\|V_Z\| < 50$ cm	1.08 M

ity (η) [Ada03b]. The trigger accepts $95 \pm 3\%$ of the d + Au hadronic cross section. The NSD $p + p$ events are triggered on the coincidence of two BBCs, which are angular scintillator detectors covering $3.3 < |\eta| < 5.0$ [Ada03d]. The NSD cross section was measured to 30.0 ± 3.5 mb by a *van der Meer* scan and PYTHIA simulation of the BBC acceptance [Ada03c]. The TOF trigger set up in Run III was to select events with a valid pVPD coincidence and at least one TOFr hit (out of 72). The trigger enhancement factors in comparison to minimum bias trigger are ∼10 in d + Au and ∼40 in $p + p$ collisions.

Centrality definition in d + Au collisions was based on the charged particle multiplicity in $-3.8 < \eta < -2.8$, measured by the FTPC in the Au beam direction [Ada03b]. But in this analysis, due to the limited statistics, the analysis was done on minimum bias d + Au events, not on each specified centralities.

3.1.2 Electron identification and hadron contamination

TPC is the main detector in STAR for tracking and identifying charged particles. With TPC only, electron identification is complicated because the electron band crosses the hadrons bands. A previous analysis on conversion electron was done for Run II Au + Au data using pure topological method, however, electron identification was limited up to $p_T \sim 0.8$ GeV/c [Ada04d, Joh02].

In addition to its hadron identification capabilities, TOFr detector can be used to identify electrons in combination with the dE/dx in the TPC, shown in Fig. 3.1. The top panel of left plot shows the 2-D scattering plot of dE/dx vs. particle momentum (p) for the charged particles with good TOFr matched hits from d + Au collisions [Rua04b]. The selection criteria are listed in Table 3.2. If additional particle velocity (β) cut

$|1/\beta - 1| < 0.03$ is applied on, this plot is shown in the bottom panel. Slow hadrons were eliminated and electrons band, then, can be separated from those fast hadrons band more readily. With combination of dE/dx in the sTPC and β in TOFr, electrons can be identified starting from $p \sim 0.15$ GeV, while the upper limit in momentum is constrained by the statistics in this analysis.

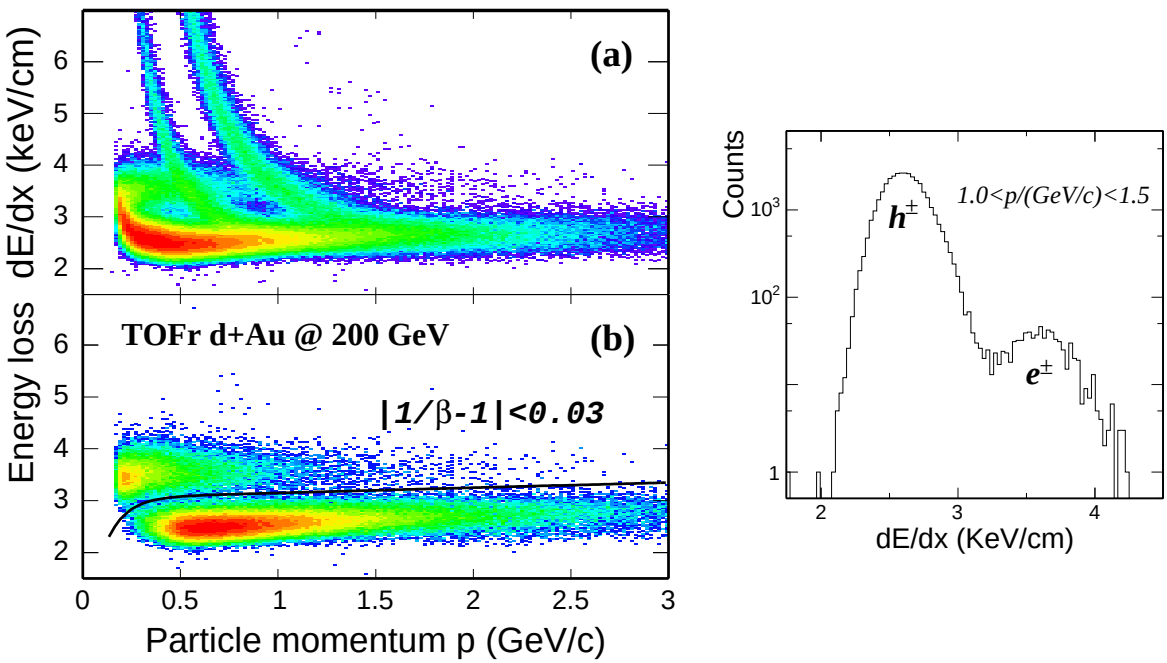

Figure 3.1: Left: Electron identification by combining β from TOFr and dE/dx from TPC. With the cut of $|1/\beta - 1| < 0.03$, electron band can be separated from the hadrons readily, shown in the bottom panel. Right: The dE/dx projection plot in $1.0 < p_T/(\mathrm{GeV/c}) < 1.5$.

Electrons were selected under the following cut:

$$dE/dx(p) > 2.4 + 0.65 \times (1 - e^{-(p-0.15)/0.1}) + 0.1 \times p \tag{3.1}$$

where p is in the unit of GeV and dE/dx is in keV/cm. Hadron contamination under this cut was studied by fitting to the dE/dx distributions in each p_T bin. The 2-Gaussian function cannot describe the shoulder region of fast hadron peak very well in lower p_T region, a function of exponential+gaussian was used in the fit. At $p_T \sim 2 - 3$ GeV, statistics cannot enable us to distinguish the difference of these two fitting methods, so

2-Gaussian fit was performed in this p_T region. Fig. 3.2 shows the fitting results in several typical p_T bins from d + Au collisions. The arrows denote the cut from Eq. 3.1. Hadron contamination ratio was estimated from these fits, shown in Fig. 3.4, and the efficiency for electrons was corrected for in the final spectra and will be discussed in the sections later.

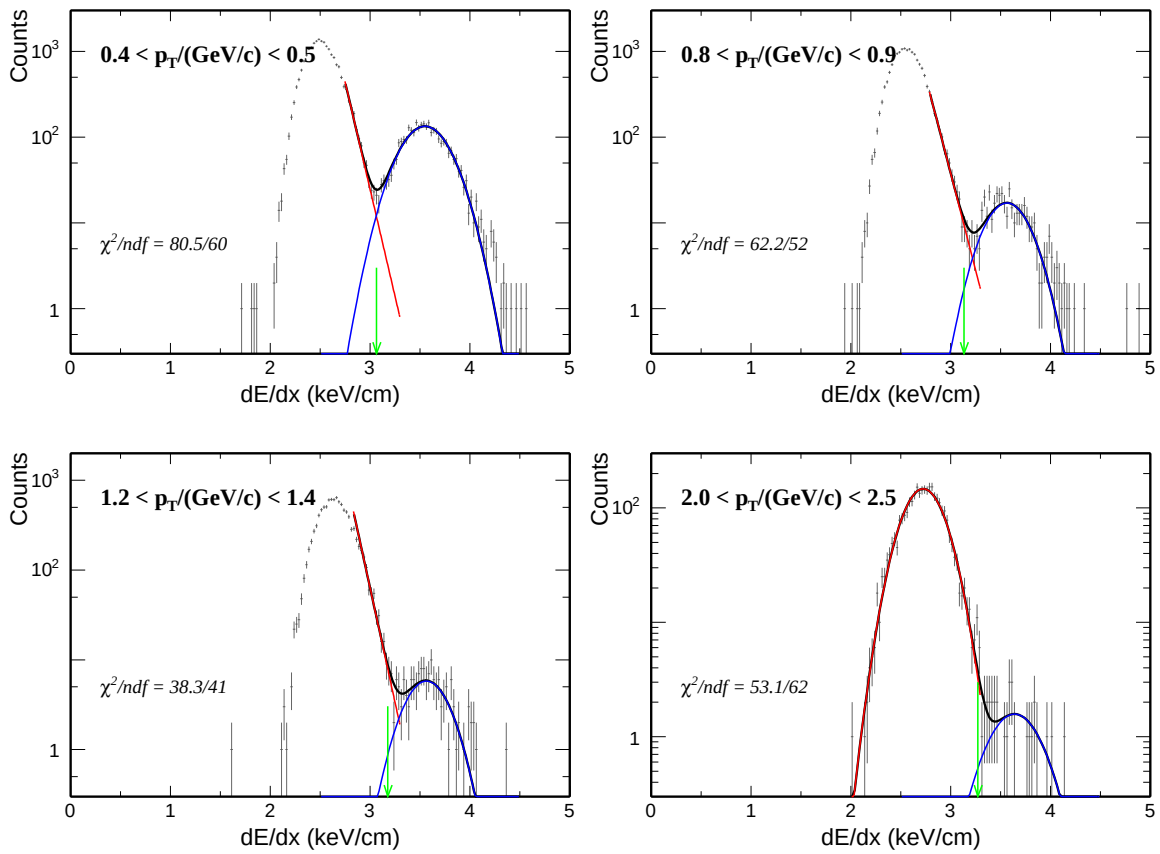

Figure 3.2: dE/dx projections in several p_T bins with the combination of TOFr PID cut. The electron yields were extracted from the fit. The green arrows denote the dE/dx cut to select electrons in each p_T bin.

At higher p_T ($2-4$ GeV/c), electrons could be identified directly in the TPC since hadrons have lower dE/dx due to the relativistic rise of the dE/dx for electrons. Positrons are more difficult to be identified using dE/dx alone because of the large background from the deuteron band. Additional track quality cuts were used in this selection: number of fit points is required to be at least 25 and the number of dE/dx points is required to be at least 16. Fig. 3.3 shows the logarithm of dE/dx distributions in each p_T bin. A 3-gaussian

function $(e+\pi+K/p)$ fit to the distribution was performed based on the assumptions that all the particles have the same dE/dx resolution and one gaussian function can describe kaons and protons. The results are shown in Fig. 3.3. Electrons with dE/dx greater than the peak mean value were selected.

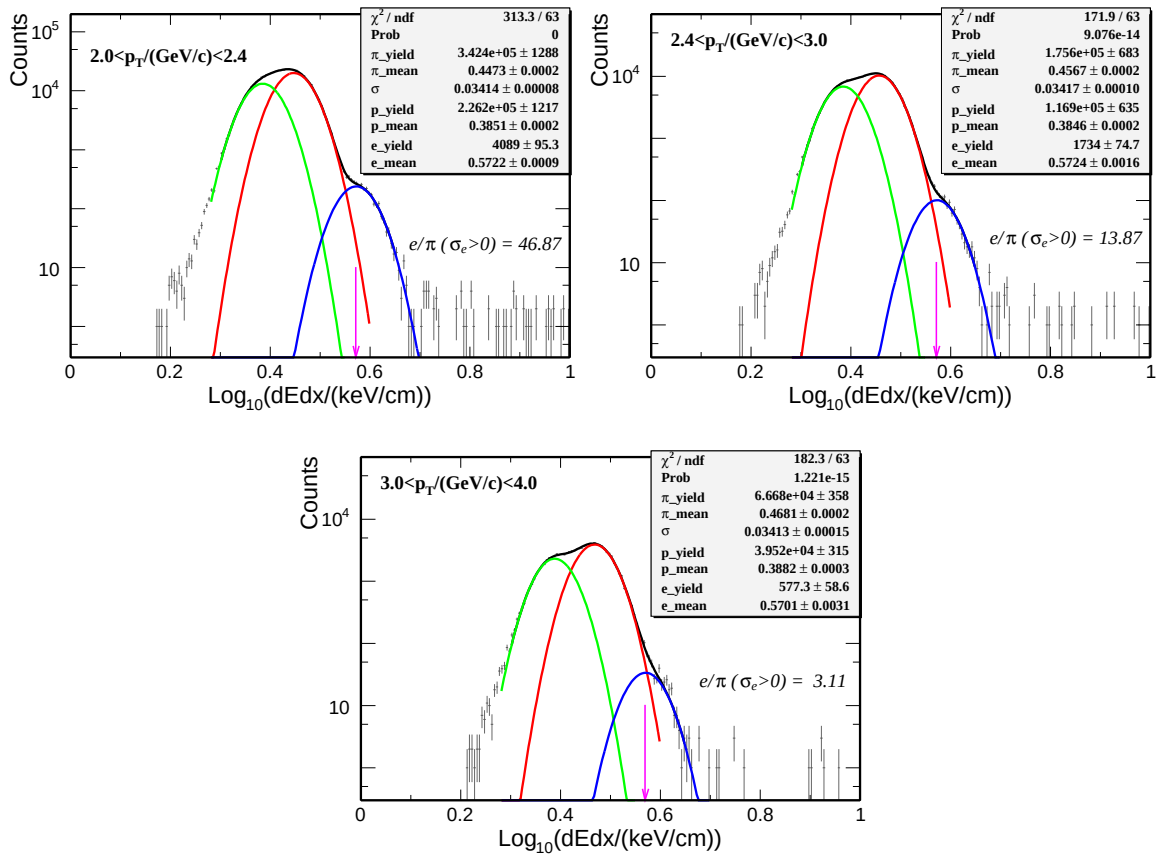

Figure 3.3: Logarithm of dE/dx distributions for negative charged particles in three p_T bins between $2-4$ GeV/c. A 3-Gaussian fit was used to extracted the electron yield and hadron contamination. The pink arrows denote the electrons selection cut.

Hadron contamination was extracted from the fits in these two methods, respectively, shown in Fig. 3.4 for both d + Au and $p+p$ collisions. The hadron contamination not only need to be subtracted statistically in the final yield, but also should be considered carefully on the track-by-track analysis later on. This will be discussed in detail in the next section.

Low hadron contamination and high electron efficiency are two competiting aspects. We performed the cut scanning to optimize the electron selection. Fig. 3.5 shows the

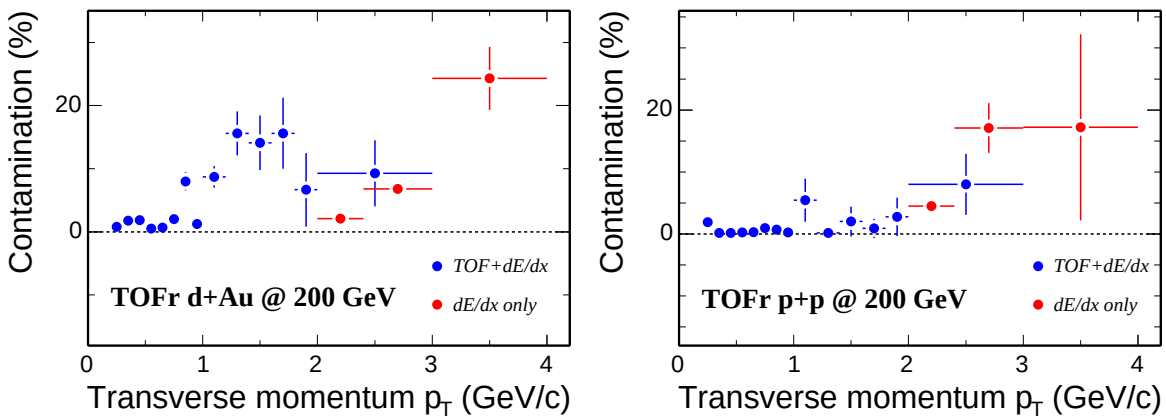

Figure 3.4: Hadron contamination fractions as a function of p_T from two electron PID methods in d + Au (left) and $p + p$ (right) collisions.

electron efficiency vs. hadron contamination. Since we are limited for the statistics currently, optimization results in the selection shown in Eq. 3.1 with $\sim$ 90% electron efficiency and $\sim$ 10% hadron contamination. Fig. 3.6 shows the p_T dependent ratio of electrons to the total hadrons. It shows $\sim$ 1% ratio at $p_T > 1$ GeV/c. Combining the $\sim$ 10% contamination ratio under the selection shown in Fig. 3.4, the estimated hadron rejection power under such selection is $\sim 10^3$ at $p_T > 1$ GeV/c and $\sim 10^4 - 10^5$ at $p_T \sim 0.5$ GeV/c.

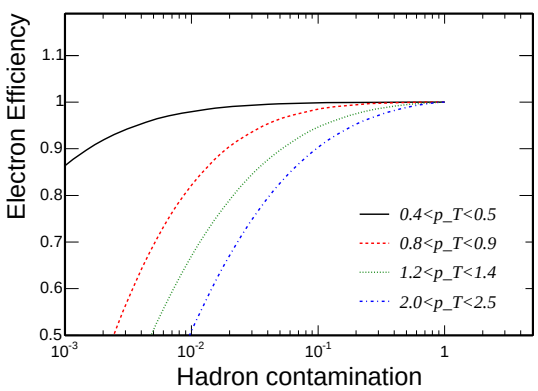

Figure 3.5: Electron efficiency vs. hadron contamination fraction by varying the dE/dx cut to selection electrons for 4 p_T bins.

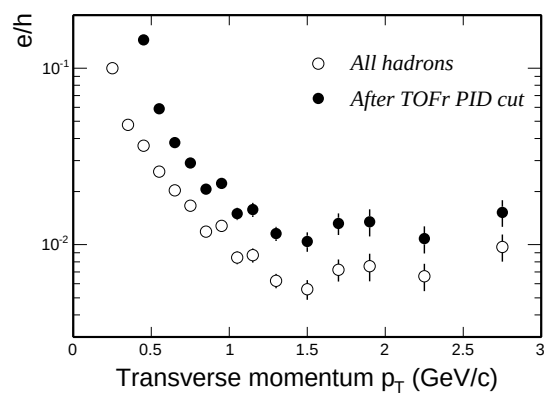

Figure 3.6: The ratio of electron yield to total hadron yield. By combining Fig. 3.4, the hadron rejection power under the current selection (Eq. 3.1) was estimated to be $\sim 10^3$ at $p_T > 1$ GeV/c.

Raw yields of inclusive electrons were then calculated from the fits to dE/dx distri-

butions at each p_T bin. Table. 3.2 lists the event-wise and track-wise cuts used in the electron selection.

Table 3.2: Electron selection criteria

Method	TOF+dE/dx	dE/dx
triggerword	2300 for d + Au 1300 for $p+p$	
$\|VertexZ\| <$	50 cm	30 cm
primary track ?	Yes	Yes
nFitPts $\geqslant$	15	25
nFitPts/nMax >	0.52	N/A
ndEdxPts $\geqslant$	N/A	16
rapidity	(-0.5, 0)	(-0.5, 0)
β from TOFr	$\|1/\beta - 1\| < 0.03$	N/A
TOFr hit quality	$10 < ADC < 300$	N/A
	$-2.7 < z_{local}/cm < 3.4$	N/A

3.1.3 Acceptance, Efficiency and Trigger bias

Raw yields need to be corrected for the detector acceptance, reconstruction and selection efficiency *etc.*, which were done through *Monte Carlo* (MC) simulations. Full detector simulations and/or embedding study show a $\sim 90\%$ reconstruction efficiency for e^+/e^- tracks, shown in Fig. 3.7. As for the tracks hitting TOFr detector, there are two ways to determine the acceptance/efficiency: the first one is divided into two steps, TPC reconstruction efficiency and the matching efficiency from TPC to TOFr from real data; the other one is get the total efficiency (including acceptance) from embedding data. Detailed matching efficiency study is referred to [Rua04b]. Due to the lower statistics of electrons, matching efficiencies of $\pi^{\pm}$ got from real data was used for electrons and a correction factor 90% was used to account for the loss (scattering and decay) of pions flying from TPC to TOFr. In the later method, d + Au HIJING events with an additional MC e^+/e^- track within TOFr acceptance were embedded into real zero-biased events, and the total efficiency was extracted from the embedding data directly. Fig. 3.8 shows the total efficiency (including acceptance) correction factor from two methods in d + Au collisions. The efficiency correction in $p+p$ collisions was used as the same number as those from d

+ Au results because of the similar multiplicities.

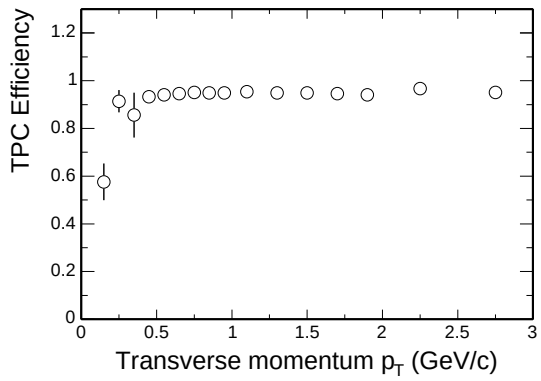

Figure 3.7: TPC track reconstruction efficiency for electrons from embedding data.

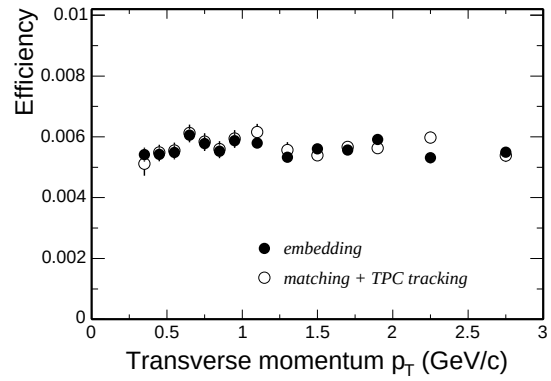

Figure 3.8: Acceptance included efficiency for TOFr + dE/dx electrons selection from two methods.

The additional TOFr PID cut $|1/\beta - 1| < 0.03$ used for slow hadrons rejection will naturally lead to some loss of the electrons. A simple fast simulation based on the TOFr timing resolution (120 ps in d + Au and 160 ps in $p + p$), charged particle phase space (p_T,η) distributions was used to determine this correction. The result shows $\sim$ 95% efficiency in d + Au and $\sim$ 87% efficiency in $p + p$ under this cut and this correction was applied in addition to the others above.

As for the TOF triggered data sets, the bias study of this trigger is mandatory. Detailed investigation was introduced in [Rua04b]. The results show no significant p_T dependence for the spectrum at $p_T > 0.3$ GeV/c according to the TOFr trigger and the charged particle multiplicity bias correction was done for both d + Au and $p + p$ data sets.

To improve statistics, the η cut $-0.5 < \eta < 0$ was removed. This leads to a $\sim$ 44% increase for the TOFr acceptance and no p_T dependence was found. Then the yields will be corrected to a definite η range for calculation according to this factor. The final results from loosing η cut are consistent within statistical errors with those with η cut applied. In the following text, we will remove this cut in the discussion.

3.1.4 Photonic background contribution

There are several sources that can contribute to the final single electron spectra in STAR environment:

- Photon (from π^0, η *etc.*) conversions in inner detectors
- π^0, η *etc.* scalar meson Dalitz decay
- ρ, ω, ϕ vector meson di-electron decay and/or Dalitz decay
- $K^{\pm}$ decay $-$ K_{e3}
- heavy flavor (c, b) hadron semi-leptonic decay
- other sources (Dell-Yan, heavy quarkonium decay, thermal electrons, direct photon conversion *etc.*)

In this analysis, the first four sources are considered to be the background $-$ photonic background, which need to be subtracted from the inclusive yield. As for the last item, theoretical predictions [Sj01, Rap01, Ala01] show no significant contributions with large uncertainties. This part of contribution is neglected in this analysis. The heavy flavor hadron decay is considered to be the only signal.

From the previous measurement [Adc02] and the estimation from the STAR environment, electrons from photon conversion and π^0 Dalitz decay dominate the total yield, especially at low p_T . At $p_T > 2$ GeV/c, the signal may become visible due to the different shape between the total spectrum and background spectrum. In PHENIX collaboration single electron analysis, they used *cocktail* method to subtract each contribution one by one [Adc02]. However, the p_T distribution and the total yield of each source particles were used as assumed input in their analysis, which may introduce large uncertainties. In STAR, due to the large acceptance of TPC, background from photon conversion *etc.* may be reconstructed experimentally. The pioneering analysis using topological method were done in [Ada04d, Joh02]. In the analysis we report here, since we have already

tagged one electron/positron track, we don't want to use the whole topological reconstruction. Instead, we try to use the kinematical features of photon conversion and π^0 Dalitz processes to justify whether the tagged electron/positron is from photonic background or not. Firstly, use TOFr or dE/dx at high p_T to tag one electron/ positron track from the primary collision vertex, then loop all other opposite-sign global tracks, whose helixes have a *distance of closest approach* (*dca*) to the tagged tracks' less than 3 cm, to find the other partner track in the TPC. Because the TPC acceptance is large, the pair reconstruction efficiency is reasonable.

To study the kinematics of the photon conversion and π^0 Dalitz decay processes, simulations of HIJING [WG91] for d + Au system and PYTHIA [Sj01] for $p+p$ system plus full detector description GEANT were investigated in detail. The data sets used are 1.38 M d + Au HIJING (v1.35 + GCALOR) minimum bias events and 1.2 M $p+p$ PYTHIA (v6.203 + GCALOR) events. The tagged electrons were required with the same cut as those for data, but all good TPC tracks were selected to increase the statistics. Fig. 3.9 shows the invariant mass square and opening angle distribution of electron pairs from different sources.

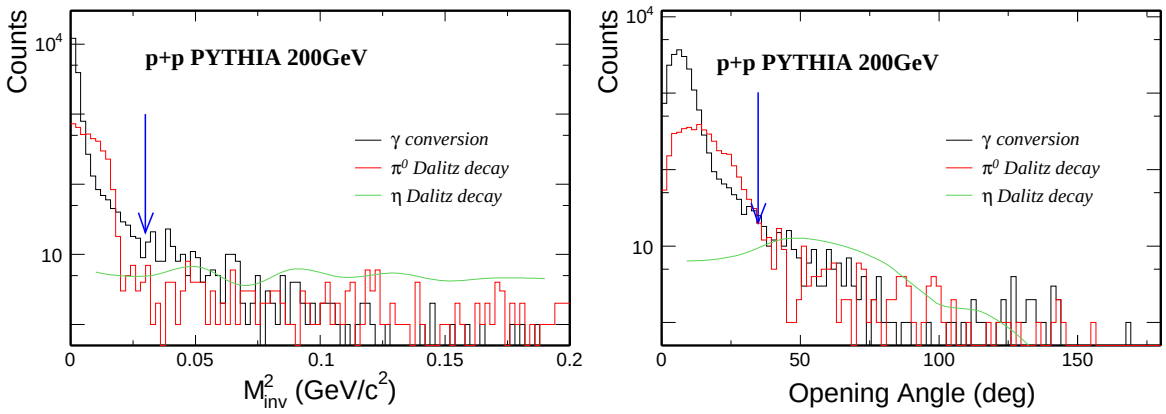

Figure 3.9: Invariant mass square and opening angle distributions of electron pairs from several sources in simulation. The blue arrows depict the cut thresholds in this analysis.

As expected, the results show those background mostly has small invariant mass square and/or small opening angle. This offers us a good opportunity to estimate the single electron background with almost topology-blind method. Those tagged electrons/positrons

with the invariant mass square or opening angle below certain thresholds will be considered to be background from photon conversion and/or π^0 Dalitz decay, and be rejected in the analysis.

To understand the background reconstruction capability in our environment, simulation study were done on the same data sets. Fig. 3.10 shows the reconstruction efficiency of photon conversion and π^0 Dalitz decay in the TPC. The simulation shows an almost constant efficiency $\sim 60\%$ at p_T above 1 GeV/c. From the π^0 embedding data, in which MC π^0 tracks through full detector response simulation were embedded into real zero-bias events , the similar result within errors was also obtained.

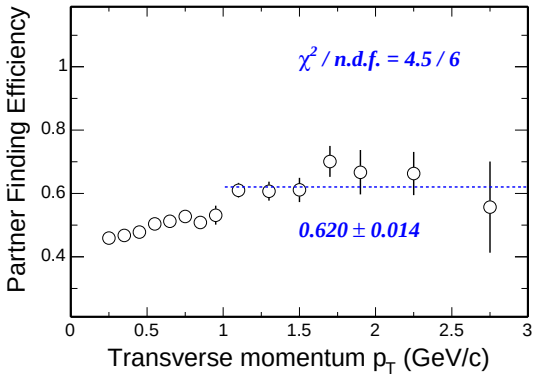

Figure 3.10: Photon conversion and π^0 Dalitz decay background reconstruction efficiency from simulations.

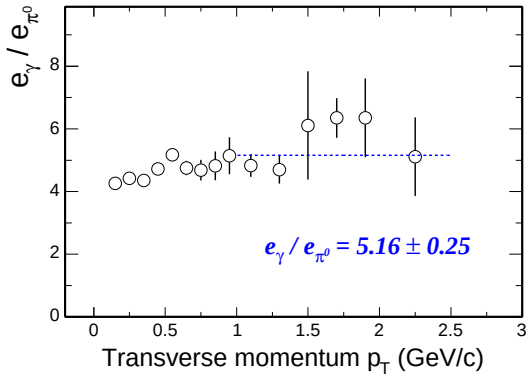

Figure 3.11: The ratio of single electrons from photon conversion to those from π^0 Dalitz decay from simulations.

By applying this efficiency to the spectrum after the kinematic cuts, one can extract the estimated total background from the main sources: photon conversion and π^0 Dalitz decay. Other contributions as well as the fractions of those could not be extracted from data directly, and we determined them from simulations. Fig. 3.11 shows the ratio of electrons from photon conversion to those from π^0 Dalitz decay. The electron spectrum from π^0 Dalitz was then used as a reference for those contributions from other light meson decays. Fig. 3.12 shows the spectra of electrons from different light hadron decays and the contribution of each source w.r.t π^0 contribution from d + Au HIJING simulations. From this , we found that the total contribution of photon conversion and π^0 Dalitz decay constitutes $\sim$ 95%, which were measured experimentally. Table 3.3 shows the

fractions of each electron background sources to the total background, averaging over $1 < p_T/(\mathrm{GeV/c}) < 3$. And the upper panel of Fig. 3.13 shows the inclusive electron spectra and the photonic background contributions in d + Au and $p+p$ collisions. Clear excess of electrons at $p_T > 1$ GeV/c is shown and the bottom panels of that plot shows the ratio of inclusive electrons to the total background electrons. The grey bands depict a 20% systematic uncertainty of the total background.

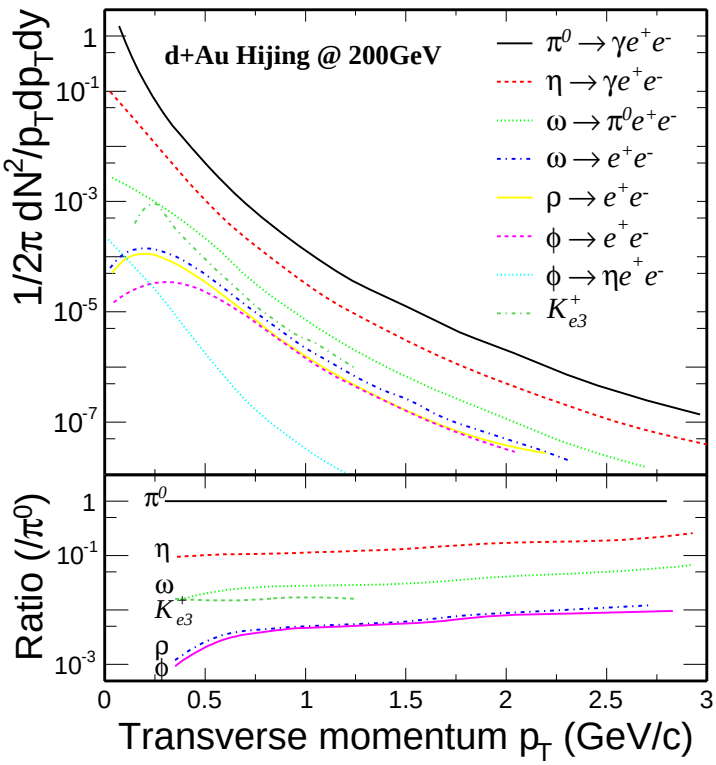

Figure 3.12: The single electron spectra from various source contributions from simulations. The bottom panel shows the relative fractions to π^0 Dalitz decay, which were used in the estimation of other source contributions in data analysis.

3.1.5 Signal extraction

One simple way to extract the signal so far is to just subtract the estimated total background from the total inclusive electron spectrum. In practice, to reduce the statistically subtracting errors, we subtracted the background from the left spectrum after the kinematical cuts applied. Besides the real background one can reject under such cuts,

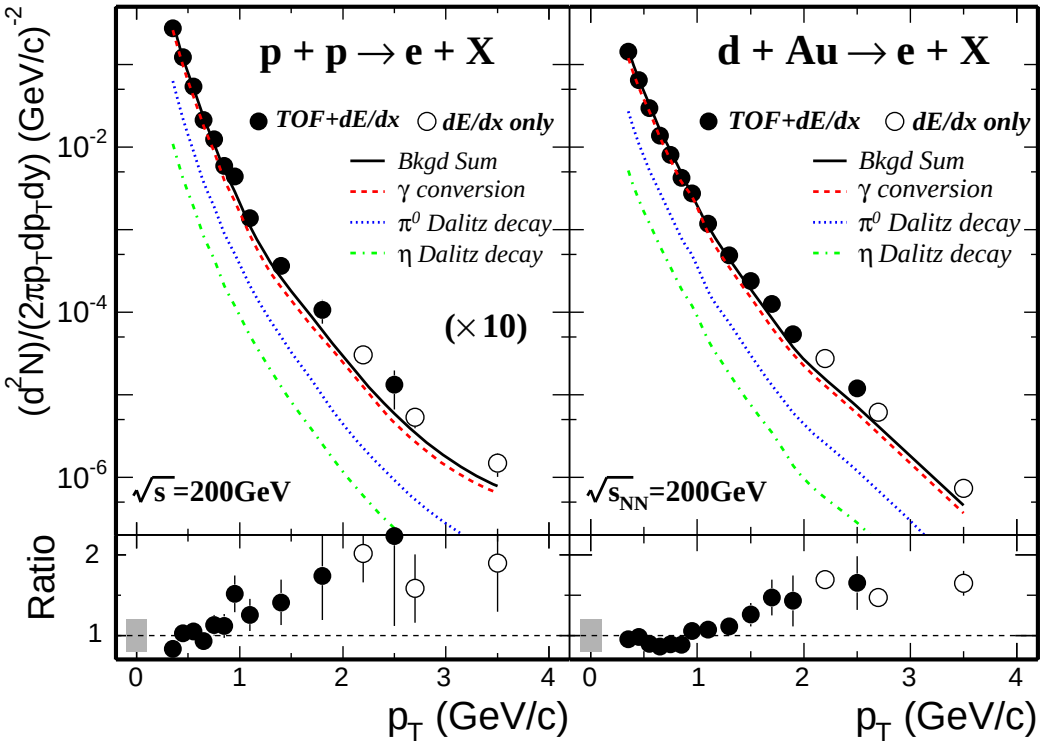

Figure 3.13: Upper panels: Electron distributions from p+p (left) and d+Au (right) collisions. Solid and open symbols depict electrons/positrons ($(e^+ + e^-)/2$) identified via a combination of TOFr and dE/dx, and electrons (e^-) identified via dE/dx alone. The measured total photonic backgrounds are shown as solid lines. Dashed lines depict the various contributing sources. The fractions were derived from simulations. Bottom panels: the ratio of inclusive electrons to the total backgrounds. The gray band represents the systematic uncertainty in each panel.

Table 3.3: Photonic sources contributions to single electron spectrum

Source	fraction (%)
γ conversion	80 ± 7
π^0 Dalitz	15 ± 2
η	3.2
ω	0.99
ϕ	0.22
ρ	0.19
K_{e3}	0.21

some signals may also be cut out due to the random combination with the hadron tracks (mostly pions), which need to be compensated after subtracting those background from photon conversion and π^0 Dalitz decay. Hadrons contaminating in the electron selection will be considered as following the random rejection power behavior under the above kinematical cuts. Fig. 3.14 shows the random rejection fractions as a function of p_T from the MC studies.

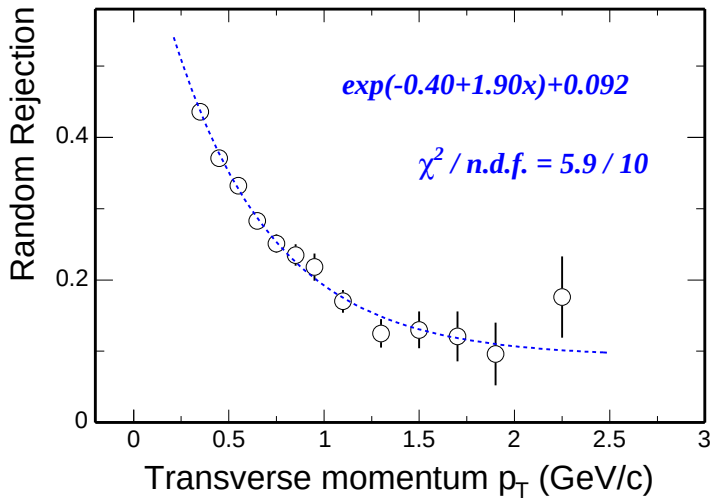

Figure 3.14: The electron fraction rejected by random particles as a function of p_T .

The signal fraction was then extracted from the following equations:

$$eff \times B + ran \times (S + H) = cut \tag{3.2a}$$

$$(1 - eff) \times B + (1 - ran) \times (S + H) = sur \tag{3.2b}$$

$$(S + B)/H = r \tag{3.2c}$$

where B, S, H represent background electrons, signal electrons and contaminating hadrons, respectively. eff denotes the efficiency of the background reconstruction, and ran denotes the random rejection efficiency for signals and hadrons. cut and sur represent the yields being cut out and surviving cuts in data, respectively. The electrons to hadrons ratio (related to hadron contaminations) r has already been obtained from previous fit to

dE/dx distributions. From (3.2), we have

$$S = \frac{(eff + ran/r) \times sur - (1 - eff + (1 - ran)/r) \times cut}{(eff - ran) \times (1 + 1/r)} \tag{3.3}$$

when hadron contamination is negligible ($r \gg 1$), the above formula can be written as

$$S = \frac{eff \times sur - (1 - eff) \times cut}{eff - ran} \tag{3.4}$$

Signal yields were extracted in each p_T bin.

The bin-by-bin systematic errors are dominated by the uncertainties of the background reconstruction efficiency from MC simulations and the hadron contamination. The errors were then calculated by varying the efficiency to 1σ uncertainty away and changing the dE/dx cut in the electron selection for different hadron contamination levels. Table 3.4 list the non-photonic electron spectra data points and the errors.

Table 3.4: Non-photonic electron spectra, the numbers represent yields ± statistical errors ± systematical errors.

		p_T (GeV/c)	data points
d + Au minbias	TOFr + dE/dx	$1.0 - 1.2$	$(1.30 \pm 0.71 \pm 0.83) \times 10^{-4}$
		$1.2 - 1.4$	$(5.52 \pm 3.66 \pm 2.41) \times 10^{-5}$
		$1.4 - 1.6$	$(6.42 \pm 2.43 \pm 3.40) \times 10^{-5}$
		$1.6 - 1.8$	$(3.88 \pm 1.61 \pm 0.88) \times 10^{-5}$
		$1.8 - 2.0$	$(1.55 \pm 0.85 \pm 0.26) \times 10^{-5}$
		$2.0 - 3.0$	$(4.82 \pm 1.99 \pm 0.47) \times 10^{-6}$
	dE/dx	$2.0 - 2.4$	$(7.53 \pm 1.12 \pm 2.41) \times 10^{-6}$
		$2.4 - 3.0$	$(1.19 \pm 0.41 \pm 0.36) \times 10^{-6}$
		$3.0 - 4.0$	$(2.45 \pm 1.22 \pm 1.72) \times 10^{-7}$
$p + p$ NSD	TOFr + dE/dx	$1.0 - 1.2$	$(2.23 \pm 1.36 \pm 1.43) \times 10^{-5}$
		$1.2 - 1.6$	$(7.02 \pm 4.51 \pm 3.30) \times 10^{-6}$
		$1.6 - 2.0$	$(3.59 \pm 2.05 \pm 0.79) \times 10^{-6}$
		$2.0 - 3.0$	$(7.16 \pm 4.57 \pm 0.70) \times 10^{-7}$
	dE/dx	$2.0 - 2.4$	$(1.10 \pm 0.30 \pm 0.36) \times 10^{-6}$
		$2.4 - 3.0$	$(1.89 \pm 0.85 \pm 0.68) \times 10^{-7}$
		$3.0 - 4.0$	$(4.11 \pm 3.02 \pm 1.68) \times 10^{-8}$

3.1.6 Background subtraction check

The photon conversions from the inner detectors are dominated by the inner SVT detector and its supporting materials. These materials are mainly within $|z| <\sim 50$ cm [Joh02]. As a double check the background subtraction, we made the vertex z position distributions of electron tracks normalized to the event vertex z position distributions, shown as solid symbols in Fig. 3.15 upper panel. The "M" structure reveals the conversion material positions. The open symbols in the same panel shows the same distributions for the cut out electrons, which are considered as conversion background. Both distributions show similar structure. If we take into account the background efficiency estimated from the discussion above, and subtract them from the total distribution, the result is depicted in the bottom panel in that figure. We cannot see significant material effect. The flat distribution demonstrates that the background subtracting method is reasonable.

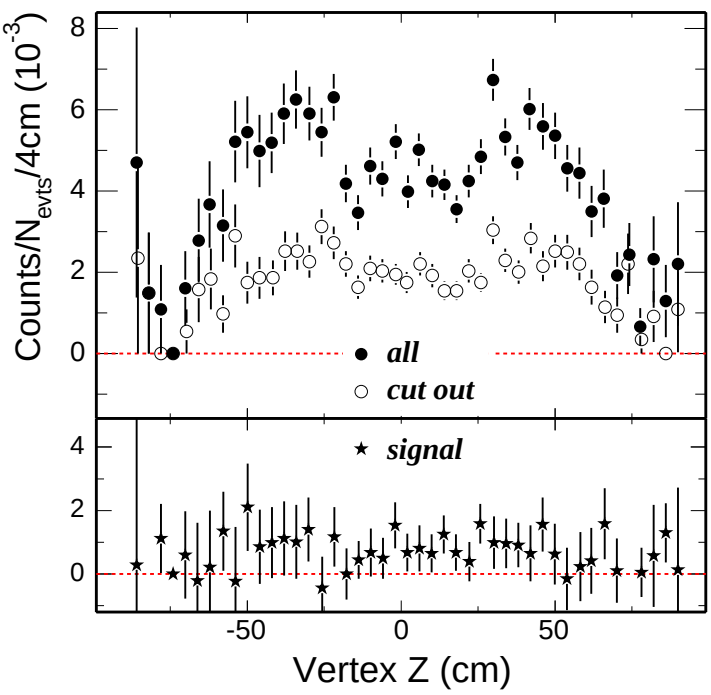

Figure 3.15: Normalized vertex z position distributions of electron tracks for total, cut-out background and expected signal.

Another important check is the electron/positron symmetry. Fig. 3.16 shows the non-photonic yield of electrons and positron separately. Within statistical errors, they are

consistent with each other. This indicates the possible δ electrons , which are knocked out from atoms in material by charged particles, does not contribute significantly in the final spectrum.

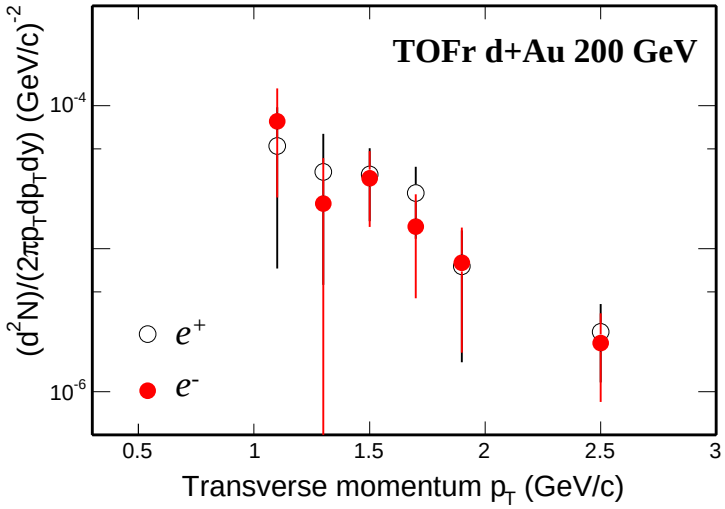

Figure 3.16: Non-photonic electrons and positrons spectra from d + Au collisions.

3.1.7 Electron dN/dy and implications for total charm production cross section

Many previous measurements tried to extract the charm production cross section from electron spectra only [Bot90, Adc02]. However, this method is strongly model dependent for the charm hadron p_T spectrum is unknown and as well as the fractions between different charm hadrons. In this analysis, the electron spectrum only covers $1-4$ GeV/c, which is corresponding to $\sim 2-6$ GeV/c in the charm hadron spectrum. The direct extraction from electron spectrum will have large systematic uncertainties.

On the other hand, STAR collaboration has measured charm mesons through hadronic decay channels in d + Au collisions [Rua04a, Tai04]. The low p_T $D^0(\overline{D^0})$ (we use D^0 implying $(D^0+\overline{D^0})/2$ in the following text) from channel $D^0(\overline{D^0})\rightarrow K^{\mp}\pi^{\pm}$ (*Branching ratio* $(B.R.) = 3.8\%$) was reconstructed through event mixing method [Adl02b]. In the following part, we will perform a fit combining both D^0 and electron data points in d + Au collisions.

Firstly, the decay kinematics of charm hadrons to electrons should be fixed. Two different decay packages were used: one is the GENBOD from CERNLIB [CER], which does the multi-body decay in phase space; the other one is the PY1ENT function from PYTHIA [Sj01], which is believed to be a more reliable one since other effects (such as spin *etc.*) have been taken into account. We implement both for the systematic studies. Fig. 3.17 shows a 2D plot of the correlation between p_T of charm hadrons and decayed daughter electron p_T. The result shows the parent charm hadrons have much higher p_T in comparison with the decayed electrons.

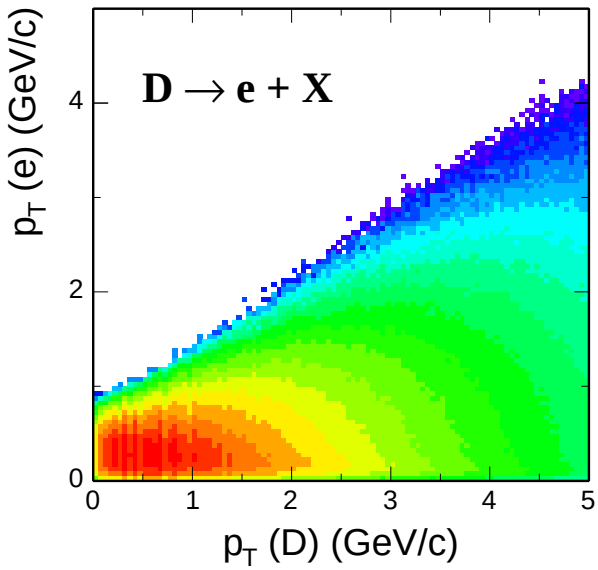

Figure 3.17: 2D correlation plot of p_T for charm hadrons and decayed electrons. The $\langle p_T \rangle$ of parent charm hadrons for decayed electrons at $p_T = 2-3$ GeV/c is ~ 4.8 GeV/c.

The fractions of different charm hadrons are also needed for the decay. Previous measurements as well as the model predictions show almost consistent ratios in broad energies and different collisions systems [Tai04]. We quote the values from e^+e^- collisions at $\sqrt{s} = 91$ GeV from PDG [Eid04]: $R \equiv N_{D^0}/N_{c\bar{c}} = 0.54 \pm 0.05$. And $D^+/D^0 \approx 0.4$ from STAR d + Au measurement. According to the large uncertainty of the $B.R.$ of $D_s^+ \to e^+ + X$ and $\Lambda_c^+ \to e^+ + X$, and both are similar to that of D^0, and the distributions of decay daughter electrons have similar shapes, we took D_s^+ and Λ_c^+ as D^0. Thus the final input charm mesons are: 79% D^0 and 21% D^+. This ratio will be tested for the systematic study later.

Table 3.5: The Combined fit characters for D^0 and electrons.

par.	scan range	step	result	χ^2/ndf
$dN/dy(D^0)$	(0.02, 0.04)	0.0004	0.029 ± 0.004	
$\langle p_T \rangle$	(0.9, 1.6)	0.05	1.15	18.8/9
n	(7, 16)	0.5	11	

The combined fit was then performed under the following assumptions:

- charm meson spectrum follows a power law function up to $p_T \sim 6$ GeV/c.
- similar p_T spectrum shape between different charm hadrons.
- the signal electrons are all from charm decays (bottom quark contribution will be discussed in chapter 5).

The power law function is written as the following:

$$\frac{d^2N}{2\pi p_T dp_T dy} = \frac{2(n-1)(n-2)}{\pi(n-3)^2\langle p_T \rangle^2}\frac{dN}{dy}\left(1 + \frac{p_T}{\frac{n-3}{2}\langle p_T \rangle}\right)^{-n} \tag{3.5}$$

There are only 3 free parameters: dN/dy, $\langle p_T \rangle$ and the power n. A specified charm hadron with a set of these parameters was input into the generators, and the decayed electrons spectrum was obtained. A 3-dimensional scan on the (dN/dy, $\langle p_T \rangle$, n) "plane" was done to fit D^0 and electron data points simultaneously. The point with the smallest χ^2 value was set to be the fit result. χ^2 was calculated from the following equation.

$$\chi^2 = \sum_D \left(\frac{y_D - f_D}{\sigma_D}\right)^2 + \sum_e \left(\frac{y_e - f_e}{\sigma_e}\right)^2 \tag{3.6}$$

where y_D, y_e denote the measured yields of D^0 and electrons and σ_D, σ_e denote the measured errors. f_D, f_e denote the expected values from input power law function for D^0 and electrons respectively. To avoid the p_T position issue in large p_T bins, we used the yield dN instead of $dN/p_T dp_T$ in each p_T bin. Table 3.5 lists all the fitting characters.

The error estimation was through the contour scan in the 3-D "plane" with the $\chi^2 =$

$\chi^2_{min} + 1$. The error of dN/dy was then obtained by projecting this 3-D contour into dN/dy axis. Fig. 3.18 shows the plots of corrected non-photonic electrons spectra and the combining fit results for D^0 and electrons spectra in d + Au collisions. The curve for $p + p$ collisions is by scaling down that of d + Au collisions by $\langle N_{bin} \rangle = 7.5 \pm 0.4$.

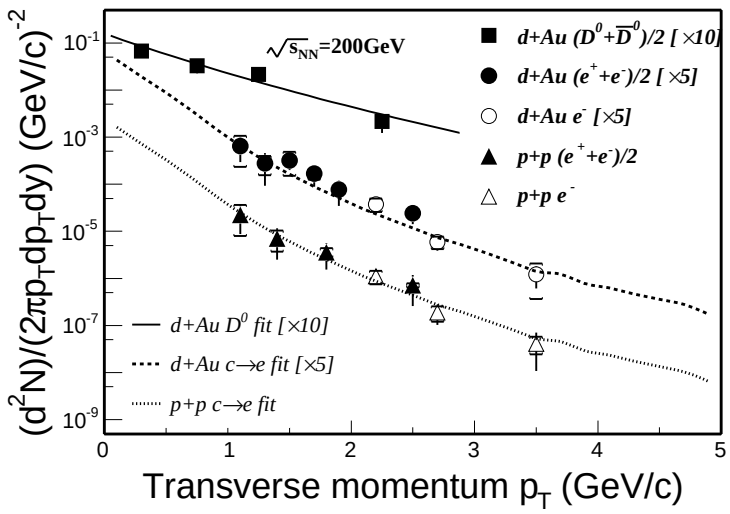

Figure 3.18: Reconstructed D^0 (solid squares) p_T distributions from d+Au collisions and non-photonic electron p_T distributions from p+p collisions (triangles) and d+Au collisions (circles). Solid and dashed lines are the fit results from both D^0 and electron spectra in d+Au collisions. The dotted line is scaled down by a factor of $\langle N_{bin} \rangle = 7.5 \pm 0.4$ from d+Au to p+p collisions.

Once the dN/dy was extracted, the total charm production cross section per nucleon-nucleon interaction at RHIC energy can be calculated from Eq. 3.7:

$$\sigma^{NN}_{c\bar{c}} = \frac{d\sigma^{NN}_{c\bar{c}}}{dy}\Big|_{y=0} \times f = \frac{dN_{D^0}}{dy}|_{y=0} \times R \times \frac{\sigma^{pp}_{inel}}{\langle N_{bin} \rangle} \times f \tag{3.7}$$

In this equation, the factor R is the D^0 fraction in total charm hadrons, as mentioned before, and f is a factor when extrapolating the dN/dy at mid-rapidity to full rapidity. This factor f was extracted from PYTHIA model study and we estimated a $\sim$ 15% systematic error on this factor from different parameters in that model. The charm production cross section per nucleon-nucleon collision at mid-rapidity and total cross

section at $\sqrt{s} = 200$ GeV is:

$$\frac{d\sigma_{c\bar{c}}^{NN}}{dy}\Big|_{y=0}(\sqrt{s} = 200\ GeV) = 0.30 \pm 0.04\ mb \tag{3.8}$$

$$\sigma_{c\bar{c}}^{NN}(\sqrt{s} = 200\ GeV) = 1.42 \pm 0.20\ mb \tag{3.9}$$

3.1.8 Systematic error study

The systematic errors contributing to the final total charm cross section were studied. One of the important sources is the uncertainty of charm hadron p_T spectrum and the fractions of different charm hadrons. The effect caused by the charm hadron p_T spectrum was studied by changing the power law parameters to 1σ away. The correlations between parameters were not taken into account in the estimation, instead, we looped all the combinations to find the largest deviation as the estimation systematic uncertainty. The effect caused by the uncertain fractions of different charm hadrons was studied by changing the effective fraction in the decay $D^0 : D^+ = 0.79 : 0.21$ to $0.90 : 0.10$ and $0.70 : 0.30$. For the charm decaying to electron kinematics, the difference of two decay codes was take into the systematic errors. Table 3.6 shows the contributions from possible sources.

Table 3.6: Systematic errors to the final charm cross sections.

Source	Relative contribution
charm hadron p_T spectrum	13%
fractions of charm hadrons	10%
decay codes	12%
$NFitHits$ $15 \rightarrow 25$	14%
rapidity distribution	15%
$\langle N_{bin} \rangle$ in d + Au	5%
Normalization	10%
Sum	31%

3.2 Single electrons from Au + Au collisions at $\sqrt{s_{NN}}$ = 62.4 GeV

The purpose of the data analysis of d + Au and $p+p$ collisions is to set up the baseline for heavy ion collisions. Since the large data sample of Au + Au collisions at $\sqrt{s_{NN}}$ = 200 GeV is not available yet, the smaller sample of Au + Au collisions at $\sqrt{s_{NN}}$ = 62.4 GeV has been analyzed to gain understandings of the necessary techniques for Au + Au collisions. Due to the significant increase of multiplicities in Au + Au collisions, and the consequent decrease of track qualities, the situation in Au + Au collisions becomes more complicated. In this section, I would discuss the inclusive electron spectrum from TOF + dE/dx method and the photonic background estimation. Since the charm yield is pretty low compared to photonic contributions, we would not expect to extract the signal with acceptable errors.

3.2.1 Data set and electron PID

RHIC has offered a relative short time Au + Au beams at $\sqrt{s_{NN}}$ = 62.4 GeV and STAR has accumulated $\sim$ 15 M events in total. With the minimum bias trigger $(0-80\%)$ and vertex z position selection, the useful physics events number in this analysis is $\sim$ 6.4 M.

The calibration results for TOF detectors are $\sim$ 110 ps resolutions for both TOFr and TOFp system, with $\sim$ 55 ps start timing resolution included. The hadron PID capability was reported in [Sha04]. Similar as before, electrons can be identified by combining TOF and dE/dx in the TPC. Primary electrons were selected under the criteria shown in Table. 3.7.

Fig. 3.19 shows the dE/dx vs. particle momentum after a β cut from TOF. Electrons band can be separated from hadrons. The dE/dx resolution in Au + Au collisions is worse than that in d + Au and $p+p$ due to much higher multiplicities, so the separation in this plot is not as good as that in d + Au and $p+p$, see Fig. 3.1. We performed both

Table 3.7: Electron selection criteria in Au + Au

Method	TOF+dE/dx
$\|VertexZ\| <$	30 cm
primary track ?	Yes
nFitPts $\geqslant$	25
ndEdxPts $\geqslant$	15
rapidity	(-1.0, 0)
χ^2/ndf	(0., 3.0)
β from TOF	$\|1/\beta - 1\| < 0.03$
TOFr hit quality	$30 < ADC < 300$
	$-2.7 < z_{local}/\text{cm} < 3.4$
	$\|y_{local} - y_C\| < 1.9$ cm
TOFp hit quality	$th_1 < ADC < th_2$
	$2.0 < z_{local}/\text{cm} < 18.0$
	$0.4 < y_{local}/\text{cm} < 3.2$

two-gaussian function and exponential+gaussian function fit to extract the electron raw yields in each p_T bin.

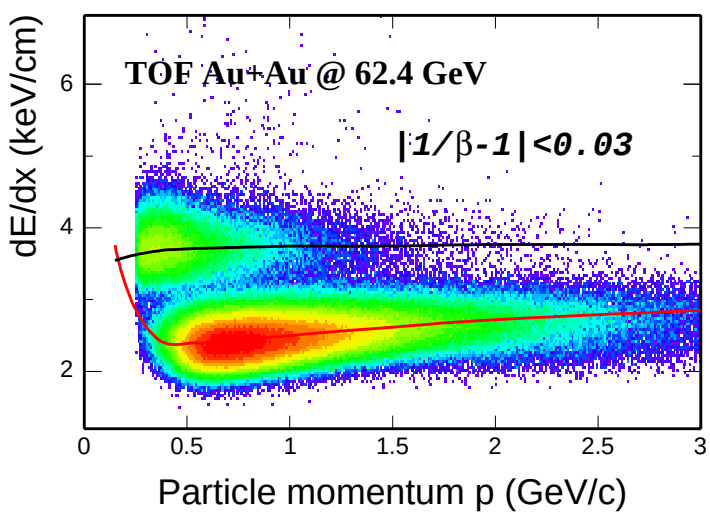

Figure 3.19: dE/dx vs. particle momentum after a TOF β cut ($|1/\beta - 1| < 0.03$)

Hadron contamination becomes larger if we select electrons with the same efficiency as before. We need to optimize the pure electron sample selection for the background study later. Fig. 3.20 shows the hadron contamination fractions under different electron selections.

The fit results show that to have contamination under control ($< 10\%$), we need the

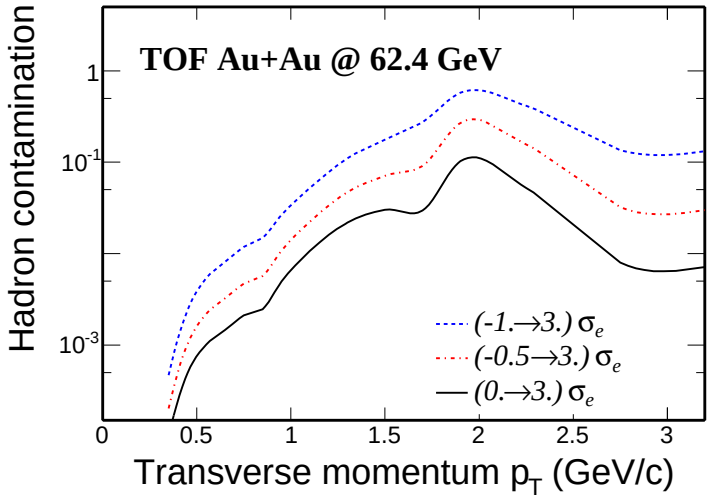

Figure 3.20: Hadron contamination fractions for different electron selections in Au + Au 62.4 GeV.

selection $\sigma_e > 0$ with electron efficiency $\sim 50\%$.

3.2.2 Non-photonic background estimation in Au + Au

In Au + Au collision events, due to large multiplicity, the PID-blinding partner track reconstruction will lead to a huge combinatorial background. Even a critical dE/dx selection is applied, this combinatorial background is still significant. Fig. 3.21 shows the electron pair candidate invariant mass distribution. The tagged electron track was selected from TOF with the cuts shown in Table. 3.7 and additional $0 < \sigma_e < 3$ (we will open it to $-1 < \sigma_e < 3$ later). The partner track candidate was selected under the criteria shown in Table. 3.8.

Table 3.8: Partner candidate selection criteria in Au + Au

charge	opposite to tagged track
primary/global ?	global
nFitPts $\geqslant$	15
nFitPts/nMax >	0.52
χ^2/ndf	(0., 3.0)
σ_e	(-1., 3.0)†
dca of e^+,e^-	(0.0, 3.0) cm

† several different σ_e cuts were tried.

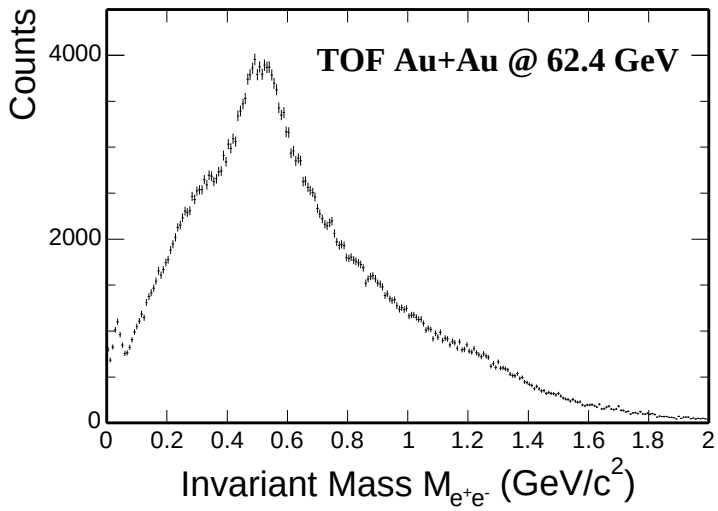

Figure 3.21: Invariant mass of electron candidates pair from the same event in Au + Au 62.4 GeV collisions. The plot shows significant combinatorial contribution near the conversion peak.

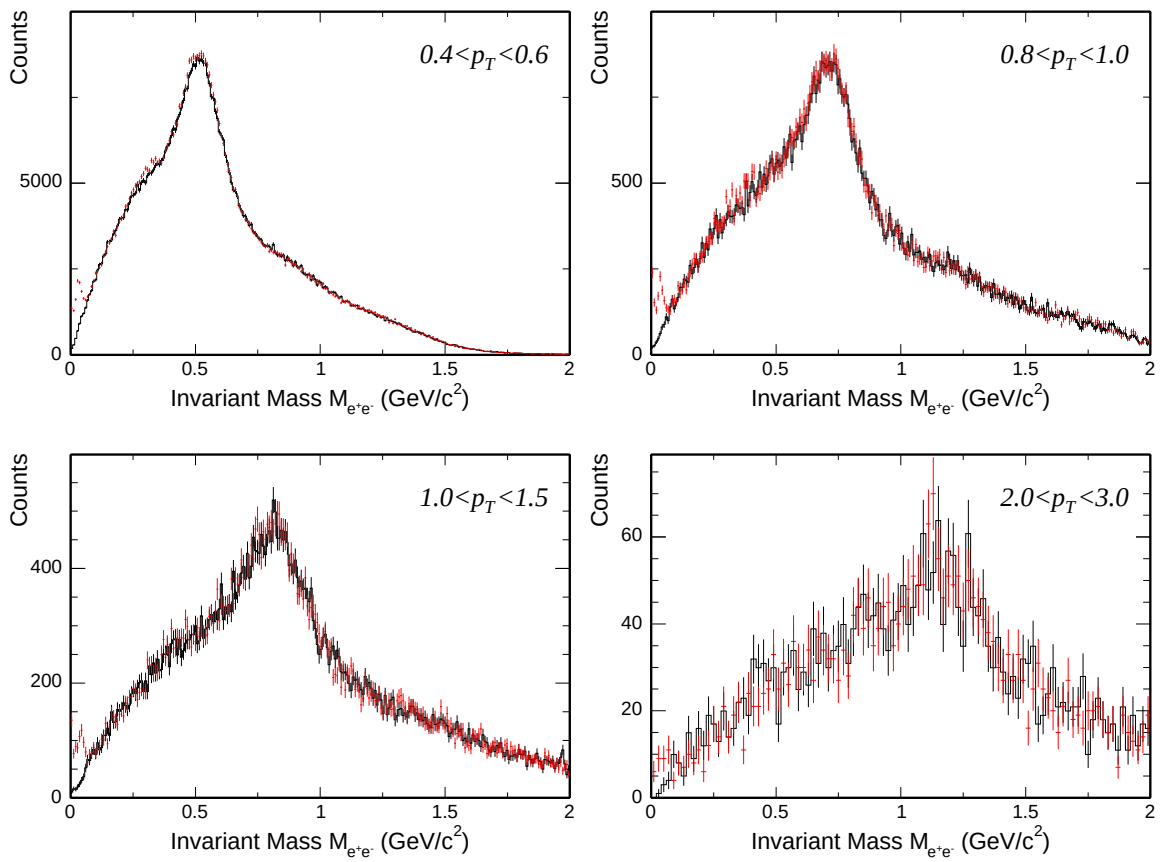

Figure 3.22: Main photonic background reconstruction in Au + Au collisions. The crosses depict the real electron pair candidate invariant mass distributions and the histograms represent the combinatorial backgrounds. The photon conversion peak is clear in ~ 0 mass region, while the π^0 Dalitz is hard to see.

To reconstruct the photon conversion and π^0 Dalitz, we need to understand the combinatory background shape in Fig. 3.21. In this step, the photon conversion and other correlations will be considered as signals, and combinatorial background was produced by rotating the partner track momentum $\overrightarrow{p} \rightarrow -\overrightarrow{p}$, then do the normalization of the mass spectrum in the region $0.8 < M_{e^+e^-}/(\mathrm{GeV/c^2}) < 2.0$. Fig. 3.22 shows this results in several p_T bins. Here p_T is the p_T of tagged electrons. The plots show the combinatorial background was very well reproduced. In the first plot, there are two small bumps at $M_{e^+e^-} \sim 0.3$ GeV/c^2 and 0.5 GeV/c^2. These are due to the misidentified pions which come from K_S^0 and ρ, ω decays, respectively. This has been confirmed through MC decay simulations.

The photon conversion peak is clearly seen near zero mass region, and the offset from 0 is due to the opening angle resolution [Joh02]. The π^0 Dalitz contribution is not visible in this case, possibly because the Dalitz contribution is much smaller and distribution is much broader compared to conversion processes. We subtracted the combinatorial background from the real distribution, and integrated the remaining distribution from $0 - 0.15$ GeV/c^2 to get the reconstructed main photonic background raw yield. In this case, we assumed that both photon conversion and π^0 Dalitz decays were reconstructed.

The background raw yield need to be corrected for the reconstruction efficiency, as we did it for d + Au and $p + p$ collisions. This efficiency was calculated from Au + Au 62.4 GeV HIJING events plus full detector MC simulations. After $|V_Z| < 30$ cm cut, ~ 53 K events were used in the calculation. We took all TPC electron tracks without any dE/dx and TOF hit cut to improve the statistics. The procedure is the same as we did before. Fig. 3.23 shows the background reconstruction efficiency in Au + Au 62.4 GeV compared with d + Au results. Due to the higher multiplicities, the relative lower reconstruction efficiency does make sense.

This efficiency was used to correct for the photonic background raw yield obtained from above. In addition, a $\sim 5\%$ fraction of other photonic background (from d + Au results) and the σ_e selection efficiency were also included. Then we can get the corrected background spectrum compared with the inclusive spectrum, shown as Fig. 3.24. All these

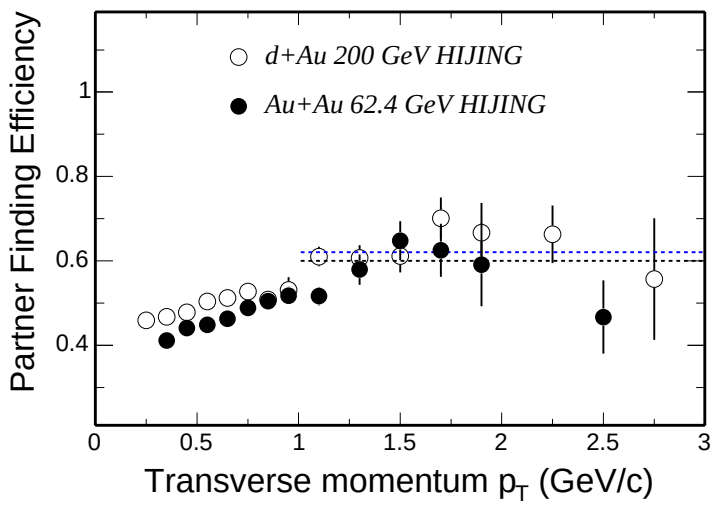

Figure 3.23: Photonic background reconstruction efficiency from Au + Au 62.4 GeV HIJING simulations. Also shown on the plot is that from d + Au 200 GeV HIJING simulations.

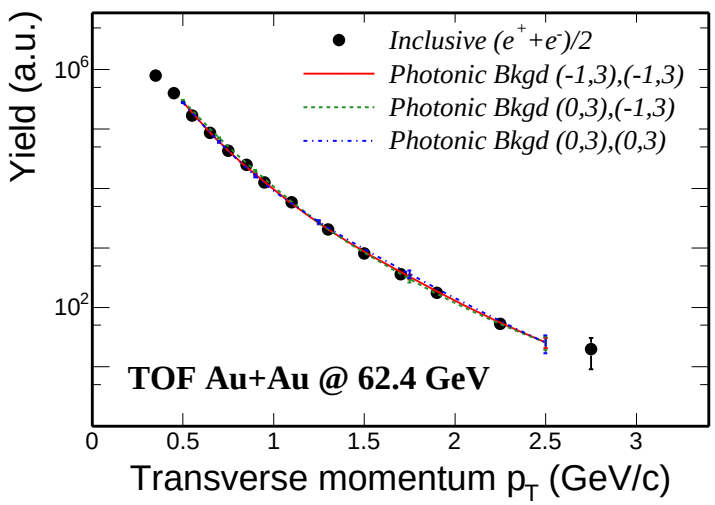

Figure 3.24: Raw inclusive electron yield and the reconstruction efficiency corrected photonic background contributions under different electron/positron track selections. The numbers in the brackets on the plot show the σ_e cut for the tagged track and the partner track, respectively.

were not corrected for the single track efficiency and acceptance yet. The reconstructed background matches the total inclusive electron spectrum. This is not surprised since the charm yield is pretty low at 62.4 GeV.

This improved method for Au + Au system working makes us confident to extract the charm signal at $2-3$ GeV/c from the coming 30 M minimum bias 200 GeV Au + Au data.

3.2.3 Spectra from Au + Au collisions at $\sqrt{s_{NN}} = 62.4$ GeV

Single electron track efficiency and acceptance is needed to correct the raw yield spectrum. The efficiency calculation is similar to what has been introduced before. Here, the method combining TPC tracking efficiency from MC simulation and TOF matching efficiency from real data was used. Fig. 3.25 shows the matching efficiency of pions from TPC to TOF (including both TOFr and TOFp) within $-1 < y < 0$ window [Sha04].

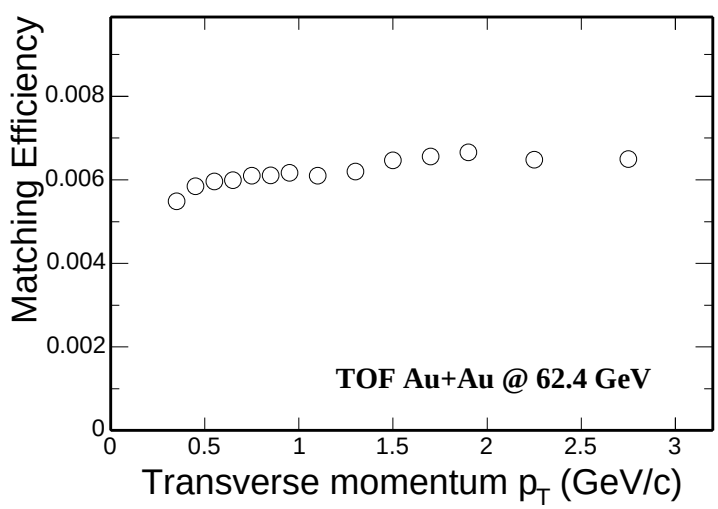

Figure 3.25: Matching efficiency (including detector response) from TPC to TOF (including both TOFr and TOFp) of pions whin $-1 < y < 0$ window.

The TPC tracking efficiency from d + Au was lowered down by 5% to as an estimation for Au + Au 62.4 GeV collisions according to the multiplicity difference in d + Au and Au + Au collisions. The TOF velocity selection efficiency was estimated to be $\sim 95\%$. With all these efficiency corrected, we can get the spectrum of inclusive electrons, shown

in Fig. 3.26. Also shown in the plot are inclusive charged pion spectrum from TOFr measurement in Au + Au 62.4 GeV and a previous ISR non-photonic electron spectrum from $p+p$ 52.7 GeV collisions scaled by the N_{bin} to Au + Au collisions. This plot shows the expected non-photonic signal is about an order of magnitude lower than the inclusive electron spectrum. This is also consistent with the photonic background reconstruction discussed in the previous section.

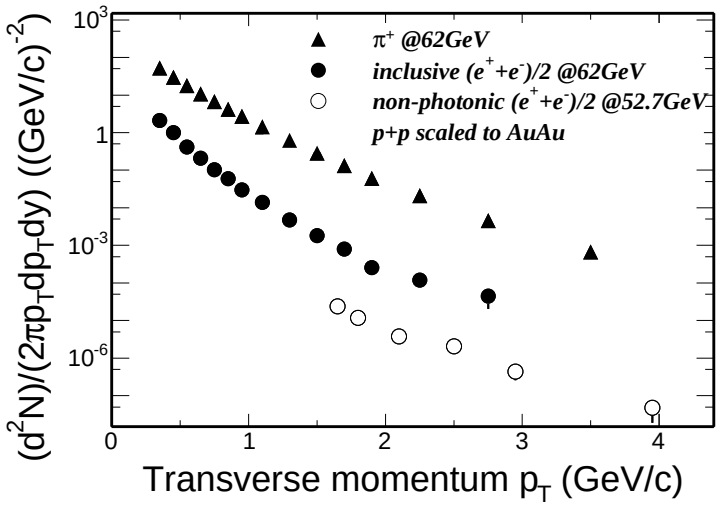

Figure 3.26: Inclusive electron spectrum in Au + Au 62.4 GeV compared with the charged pion spectrum in the same system and the ISR non-photonic electron spectrum in 52.7 GeV $p+p$ collisions scaled with N_{bin} to Au + Au minimum bias collisions.

Although more than $\sim 90\%$ of the electrons up to 3 GeV/c are photonic background in Au + Au 62.4 GeV so that we cannot extract the non-photonic signal with reasonable errors, this photonic background reconstruction method works well and technically, it is ready for the coming 200 GeV large data sample analysis to answer some of the issues about the charm production in heavy ion collisions.

CHAPTER 4

Single electron azimuthal anisotropy distributions

The data set used in this analysis is Au + Au minimum bias triggered $(0 - 80\%)$ events at $\sqrt{s_{NN}} = 62.4$ GeV. This data sample is the same as that described before. The anisotropic parameters were obtained from event plane analysis technique. The detailed analysis method introduction can be found in [PV98].

4.1 Event plane and its resolution

In heavy ion collisions, the even plane is reconstructed from the detected final particle azimuths. The acceptance and efficiency of the detectors in azimuth was corrected by compensating the azimuth to a flat distribution with ϕ weights. Technically, the ϕ weights were created for different days to deal with the different situations in long period run. Additional p_T weight was also applied to improve the event plane resolution. Thus, the second order harmonic event plane azimuth Ψ_2 can be calculated from the $\overrightarrow{Q}$ vector, as Eq. 4.1,4.2:

$$\Psi_2 = \left(\arctan^{-1}\frac{Q_y}{Q_x}\right)/2, \qquad 0 < \Psi_2 < \pi \tag{4.1}$$

$$\overrightarrow{Q} = (Q_x, Q_y) = \left(\sum_i w_i \cdot \cos(2\phi_i), \quad \sum_i w_i \cdot \sin(2\phi_i)\right) \tag{4.2}$$

Here, w_i is the weight for each track included in event plane calculation, which includes both ϕ weight and p_T weight. Fig. 4.1 shows the a set of typical ϕ weight distributions for a single day. The bumps at $\phi \sim 6$ in "east" and "fast east" plots are due to a bad sector in east side TPC. The tracks selected in the event plane calculation should satisfy

the criteria shown in Table. 4.1.

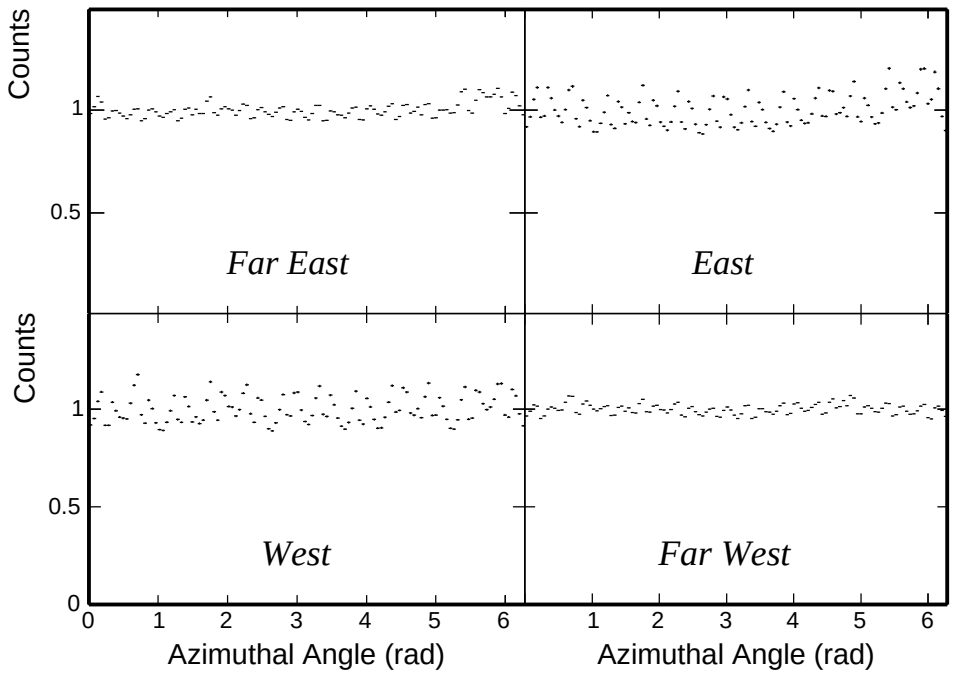

Figure 4.1: ϕ weight used for a single day for minimum bias 62.4 GeV Au + Au collisions. The bump around ~ 6 rad in ϕ in east and far east set is due to a bad sector in east side of TPC.

Table 4.1: Track selection in event plane calculation

nFitPts	≥ 15
nFitPts/nMax	> 0.52
p_T	(0.1, 4.0)
η	(-1.3, 1.3)
global dca	(0.0, 3.0)

Fig. 4.2 shows the second order event plane azimuthal angle distribution. This distribution was fit to a constant value and the fit quality $\chi^2/ndf = 126/119$ which means a good event plane reconstruction.

The resolution of event plane was calculated through sub-event method [PV98]. Each event was divided into two sub-events with nearly equal multiplicity randomly. The event plane was reconstructed in each sub-event, denoted as Ψ_2^a and Ψ_2^b. Then the event plane resolution $r = \langle cos[2(\Psi_2 - \Psi_{rp})]\rangle$ can be calculated from Eq.(14) and (11) from [PV98], which are shown as followings:

$$\langle\cos[2(\Psi_2 - \Psi_{rp})]\rangle = \frac{\sqrt{\pi}}{2\sqrt{2}}\chi_2 \exp(-\chi_2^2/4) \times [I_0(\chi_2^2/4) + I_1(\chi_2^2/4)] \tag{4.3}$$

$$\langle\cos[2(\Psi_2^a - \Psi_{rp})]\rangle = \sqrt{\langle\cos[2(\Psi_2^a - \Psi_2^b)]\rangle} \tag{4.4}$$

$$\chi_2 = v_2/\sigma = v_2\sqrt{2N} \tag{4.5}$$

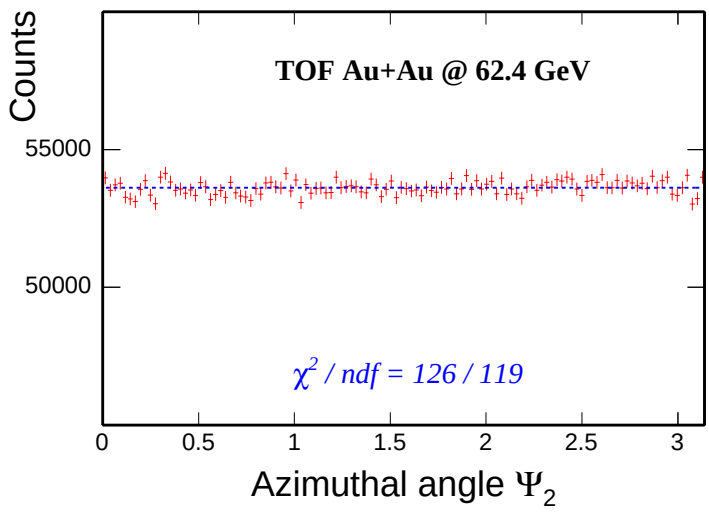

Figure 4.2: The second harmonic event plane azimuthal angle distribution. A constant fit with χ^2/ndf close to unity means a good event plane reconstruction.

Firstly, we obtained the sub-event resolution $\langle\cos[2(\Psi_2^a - \Psi_{rp})]\rangle$ from Eq. 4.4. Then using Eq. 4.3 applied on sub-event, we can extract the sub-event χ_2^a. The variable is proportional to $\sqrt{N}$ according to Eq. 4.5, so the total event χ_2 was obtained by $\chi_2 = \sqrt{2}\chi_2^a$. And after putting this χ_2 into Eq. 4.3, we calculated the final full event resolution. The physical v_2 is calculated as $v_2 = v_2^{obs}/r$, where v_2^{obs} is the observed v_2 and r is the event plane resolution. However, experimentally, what we observe is $\langle v_2^{obs}\rangle$, the averaged v_2^{obs} over a data sample, such as the minimum bias events. Then

$$\langle v_2\rangle = \left\langle \frac{v_2^{obs}}{r} \right\rangle \approx (but \neq)\frac{\langle v_2^{obs}\rangle}{\langle r\rangle} \tag{4.6}$$

This is not quite correct when we just divide the $\langle v_2^{obs}\rangle$ by the event-wise averaged resolution $\langle r\rangle$. Practically, we calculated a track-wise averaged resolution by weighting

each event with the number of observed particles in v_2^{obs} calculation [Sor04]. Fig. 4.3 shows the event-wise averaged and track-wise averaged event plane resolution for 9 centrality bins and minimum bias $(0-80\%)$ events. The final event plane resolution used for correction is 68% for minimum bias Au + Au 62.4 GeV collisions.

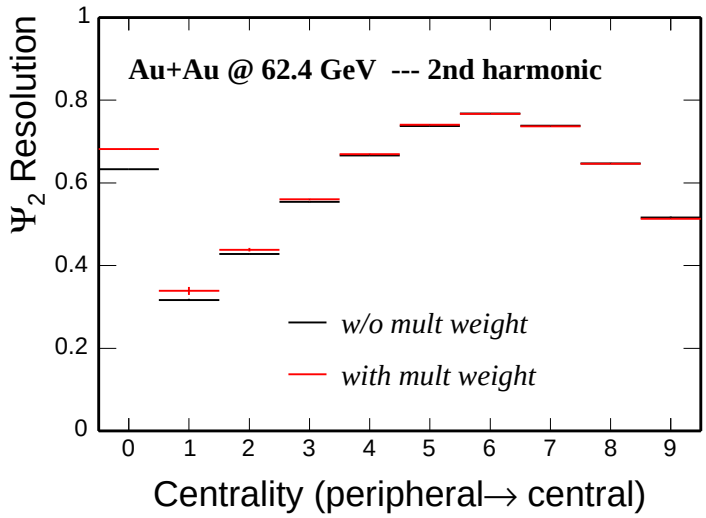

Figure 4.3: Event plane resolutions for all centrality bins (bin 1-9) and minimum bias $(0-80\%)$ events (bin 0). Black points show the resolution with event weight only. Red points show the improved resolution with multiplicity weight.

4.2 Elliptic flow of stable hadrons

The TOF detectors were used for hadron identification in this analysis. Multiple gaussian fit was applied to the M^2 distributions in each p_T bin. In those p_T bins that peaks start to merge, a cut of more than 95% purity was applied in the particle selection. In the p_T region out of π and K separation with TOF only, dE/dx was used additionally to help on the π identificaion while K PID is limited by its low yield [Sha04].

There is a certain correlation between the selected particle ϕ_j and the event plane azimuth calculated including this particle. This so-called auto correlation was removed by excluding this selected particle in a new event plane azimuth calculation. The new $\overrightarrow{Q_j}$ vector was constructed by:

$$\overrightarrow{Q_j} = (Q_{jx}, Q_{jy}) = \left(\sum_{i \neq j} w_i \cdot \cos(2\phi_i), \quad \sum_{i \neq j} w_i \cdot \sin(2\phi_i) \right) \tag{4.7}$$

$$\Psi_{2j} = \left(\tan^{-1} \frac{Q_{jy}}{Q_{jx}} \right) /2 \tag{4.8}$$

Then the v_2^{obs} in each p_T bin was calculated by

$$v_2^{obs} = \langle \cos[2(\phi_j - \Psi_{2j})] \rangle \tag{4.9}$$

Fig. 4.4 shows the measured resolution corrected v_2 of $\pi^{\pm}$, $K^{\pm}$ and $p(\bar{p})$ from TOF detector at Au + Au 62.4 GeV minimum bias $(0 - 80\%)$ collisions. The results show: at low p_T region, the mass ordering is similar to what has been observed in 200 GeV Au + Au collisions; and at intermediate p_T ($>$ 2 GeV/c) the proton v_2 overtakes pion v_2, which is also similar to that in 200 GeV case. To check the NCQ scaling what we have observed in 200 GeV data, a funtion parametrization Eq. 4.10 was used to fit to the measured v_2 [DES04].

$$v_2(p_T, n) = \frac{an}{1 - \exp[-(p_T/n - b)/c]} - dn \tag{4.10}$$

The fit results are shown in Table. 4.2, which are consistent with NCQ scaling picture. This scaling in 62.4 GeV was also further demonstrated by the measurements of v_2 of K_S^0, Λ, Ξ and Ω [zzz05].

Table 4.2: Parametrization for v_2 of $K^{\pm}$ and $p + \bar{p}$

	$K^{\pm}$	$p + \bar{p}$
a	6.3 ± 1.8	6.1 ± 1.3
b	0.44 ± 0.04	0.38 ± 0.03
c	0.14 ± 0.06	0.13 ± 0.04
d	0.05 ± 1.05	0.66 ± 0.92

Comparisons of the identified particle v_2 from different energy measurements are shown in Fig. 4.5. Those are measurements from $\sqrt{s_{NN}} = 200$ GeV Au + Au minimum bias $(0-$

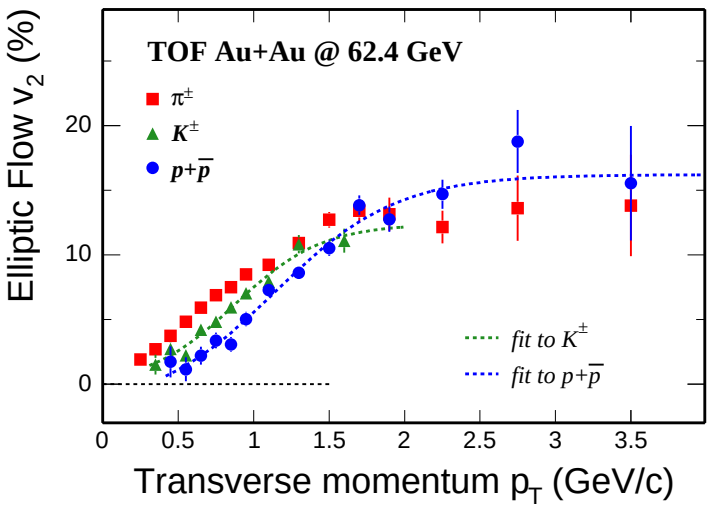

Figure 4.4: Elliptic flow v_2 of $\pi^{\pm}$, $K^{\pm}$ and $p(\bar{p})$ from TOF detector at Au + Au 62.4 GeV minimum bias $(0-80\%)$ collisions. Curves depict the parametrized function fit from [DES04].

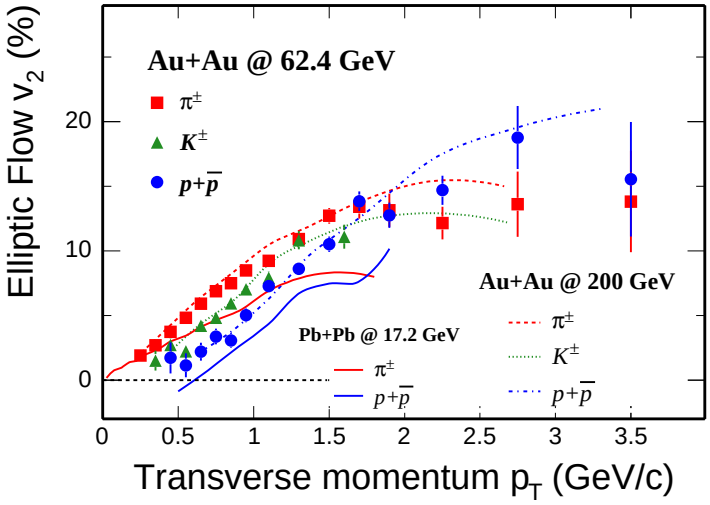

Figure 4.5: Minimum bias Au + Au 62.4 GeV v_2 (data points) compared with those from 200 GeV measurements in Au + Au collisions at RHIC (non-solid lines) citephenixpikpv2 and 17.2 GeV measurements for pions and protons (solid lines) in Pb + Pb collisions at SPS [Alt03].

92%) collisions [Adl03a] and $\sqrt{s_{NN}} = 17.2$ GeV Pb + Pb minimum bias collisions [Alt03]. The results show the v_2 from 62.4 GeV is very similar to that from 200 GeV measurement, while it is significantly different from that in 17.2 GeV measurement. This can indicate a phase transition happening from SPS (lower v_2) to RHIC top energy (higher v_2).

Charged pions can also be identified using the relativistic dE/dx (rdE/dx) method [Xu04] up to ~ 7 GeV/c (limited by the statistics). A simple selection of $0 < \sigma_\pi < 2$ was used to select pion sample and the contamination from kaons and protons was estimated to be less than 3% [Xu04]. Fig. 4.6 shows the pion v_2 measured over a large p_T region ($0.2 - 7.0$ GeV/c). The event plane method shows a continuous flat region up to almost 7 GeV/c. However, the non flow effect in high p_T region becomes important and even significant in central and peripheral collisions [Ada04e]. To answer the question of high p_T identified particle v_2, we need other methods (such as multiparticle cumulant methods *etc* [Ada04f]) to minimize the non flow effects.

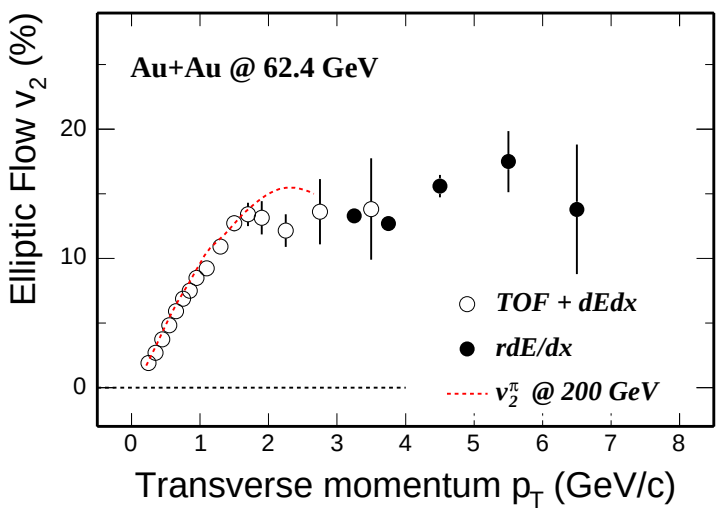

Figure 4.6: Pion v_2 from TOF, TOF + $dEdx$ and relativistic dE/dx (rdE/dx) measurements in Au + Au 62.4 GeV.

4.3 Elliptic flow of inclusive and photonic background electrons

The electron PID capability in Au + Au 62.4 GeV was already shown in Fig. 3.19. With the selection of $0 < \sigma_e < 3$, we identify electrons with the purity more than 90% in

$1-3$ GeV/c. The inclusive electrons v_2 was extracted using the similar method as what we did for v_2 of $\pi^{\pm}$, $K^{\pm}$ and $p(\bar{p})$. Fig. 4.7 shows the results compared with v_2 of $\pi^{\pm}$. Since the dominant source of the electrons are photon conversion where the photons are from π^0 two photon decay processes, and π^0 Dalitz decay, the electrons at lower p_T will carry the anisotropy of those parent pions at higher p_T . This will be discussed in the next chapter.

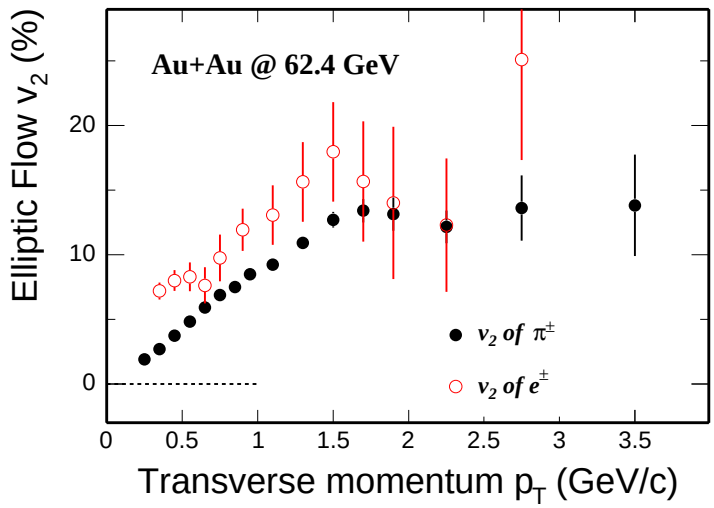

Figure 4.7: v_2 of inclusive electrons and pions from TOF detector in Au + Au 62.4 GeV minimum bias $(0-80\%)$ collisions.

Photonic electrons v_2 is needed to extract the interesting non-photonic electrons v_2. We used event mixing technique to reconstruct the main photonic background from the TPC only. The tagged and partner electrons candidate are selected using the same selection criteria shown in Table. 3.7 and 3.8, but we used all TPC candidates instead of TOF tracks only. Both tagged and partner track are required to have $0 < \sigma_e < 3$ to reject large amount of hadrons. The event buffer used for mixing is divided into a $10 \times 10 \times 9$ lattice in (V_z, Mult, Ψ_2) with lattice size of 6 cm $\times$ 60 $\times$ 20°. Two 3-D ($M_{e^+e^-}$, p_T , $\Delta\phi = \phi - \Psi_2$) histograms for the same event and mixed-event were stored. The additional dimension in Ψ_2 for event mixing is to get the residual background reasonably well controlled in different $\Delta\phi$ bins. The histograms were then projected into $M_{e^+e^-}$ axis for each (p_T , $\Delta\phi$) bin. The mixed event distribution, which is expected to describe combinatorial contribution, was normalized to the same event distribution in high $M_{e^+e^-}$ region, where

there is no significant decay correlation. The normalized mixed event distribution was then subtracted from the same event distribution. The photonic electrons was extracted for every $\Delta\phi$ bin in each p_T bin. The $\Delta\phi$ distribution was fit to the following function to get the observed v_2^{obs}.

$$\frac{dN}{d(\Delta\phi)} \propto 1 + 2v_2^{obs}\cos(2\Delta\phi) \tag{4.11}$$

Fig. 4.8 shows $M_{e^+e^-}$ distribution of the electron candidate pairs from the same event (crosses) and the mixed event (histograms) in different $\Delta\phi$ bin for tagged electron $2.0 < p_T/(\mathrm{GeV/c}) < 2.5$. The combinatorial background shows oscillation in $\Delta\phi$, which is expected from the anisotropy from final state hadrons. After mixed combinatorial background subtracted, the photonic source electrons anisotropy is shown in Fig. 4.9. Since the photon conversion (π^0 Dalitz continuum may hide in) distribution is not a gaussian-like peak, it is hard to do a signal+background fit as we did for other resonances to extract the signal yields. We need to understand the residual background well. So in the yield extraction in each $\Delta\phi$ bin, we tried several residual background estimation to extract the systematic errors: (i) no residual. (ii) use a constant fit in $0.15 < M_{e^+e^-}/(\mathrm{GeV/c^2}) < 0.25$ and take it as a residual. (iii) the same as (ii), but take the averaged value through all $\Delta\phi$ bins as a common residual. Fig. 4.10 shows the yields from each $\Delta\phi$ bin using method (iii). Eq. 4.11 was used to fit the distribution and the result is $v_2^{obs} = (13.4 \pm 4.4)\%$. After resolution correction, we can get the physics v_2 of electrons from photonic sources. Fig. 4.11 shows the photonic electrons v_2 as a function of p_T , compared with the inclusive electrons v_2 and pions v_2. The photonic electrons v_2 shows consistent with that of inclusive electrons, which is expected from the spectra analysis in the previous chapter.

In general, the v_2 of inclusive electrons is the sum of photonic (B) and non-photonic (S) electrons v_2, weighted by each yield fraction f_B, f_S.

$$v_2^{tot} = f_B \times v_2^B + f_S \times v_2^S \tag{4.12}$$

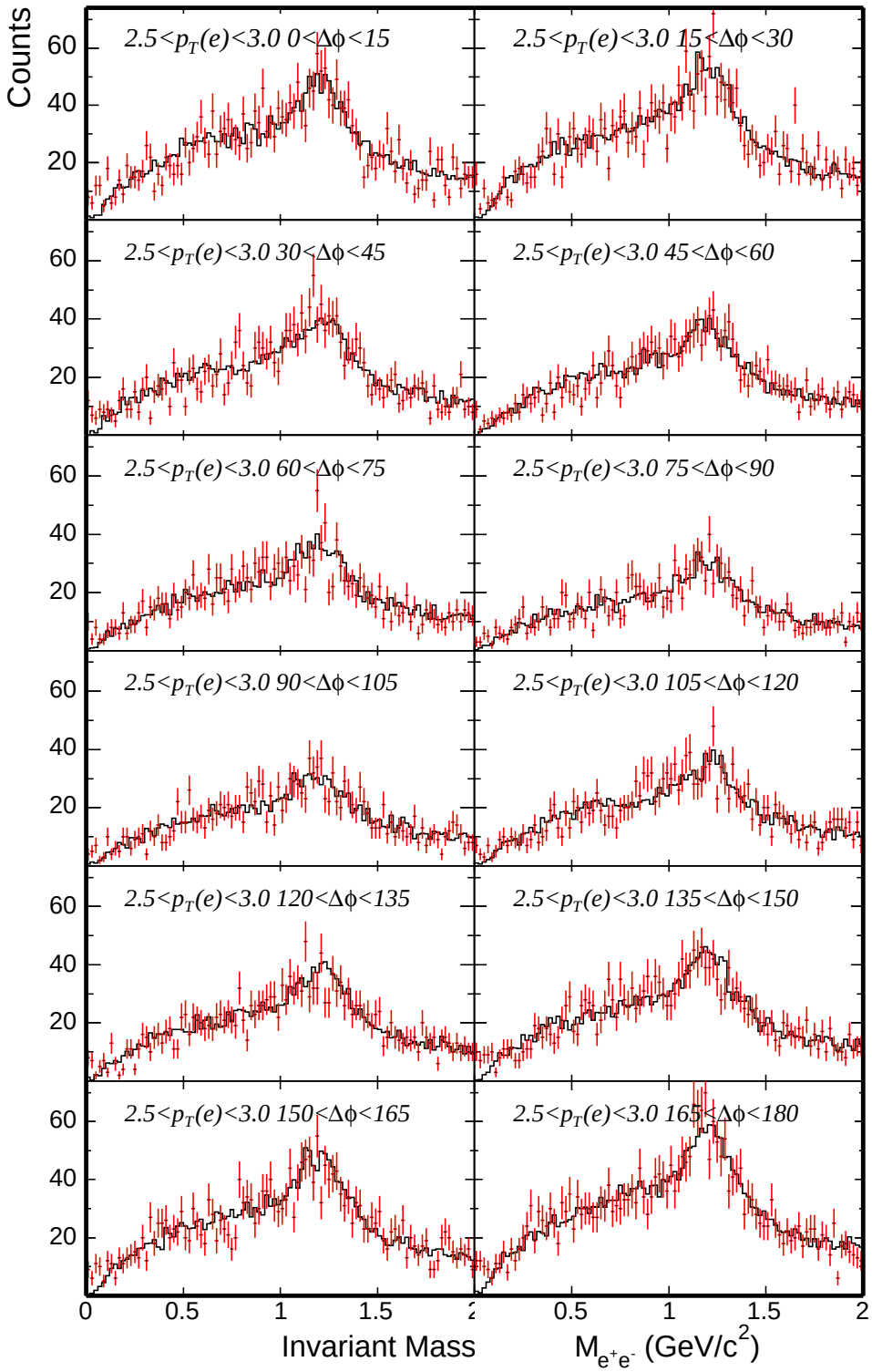

Figure 4.8: Invariant mass $M_{e^+e^-}$ distributions of electron pair candidates and the combinatorial background from rotating method in each $\Delta\phi$ bin for tagged electron $2.0 < p_T/(\mathrm{GeV/c}) < 2.5$.

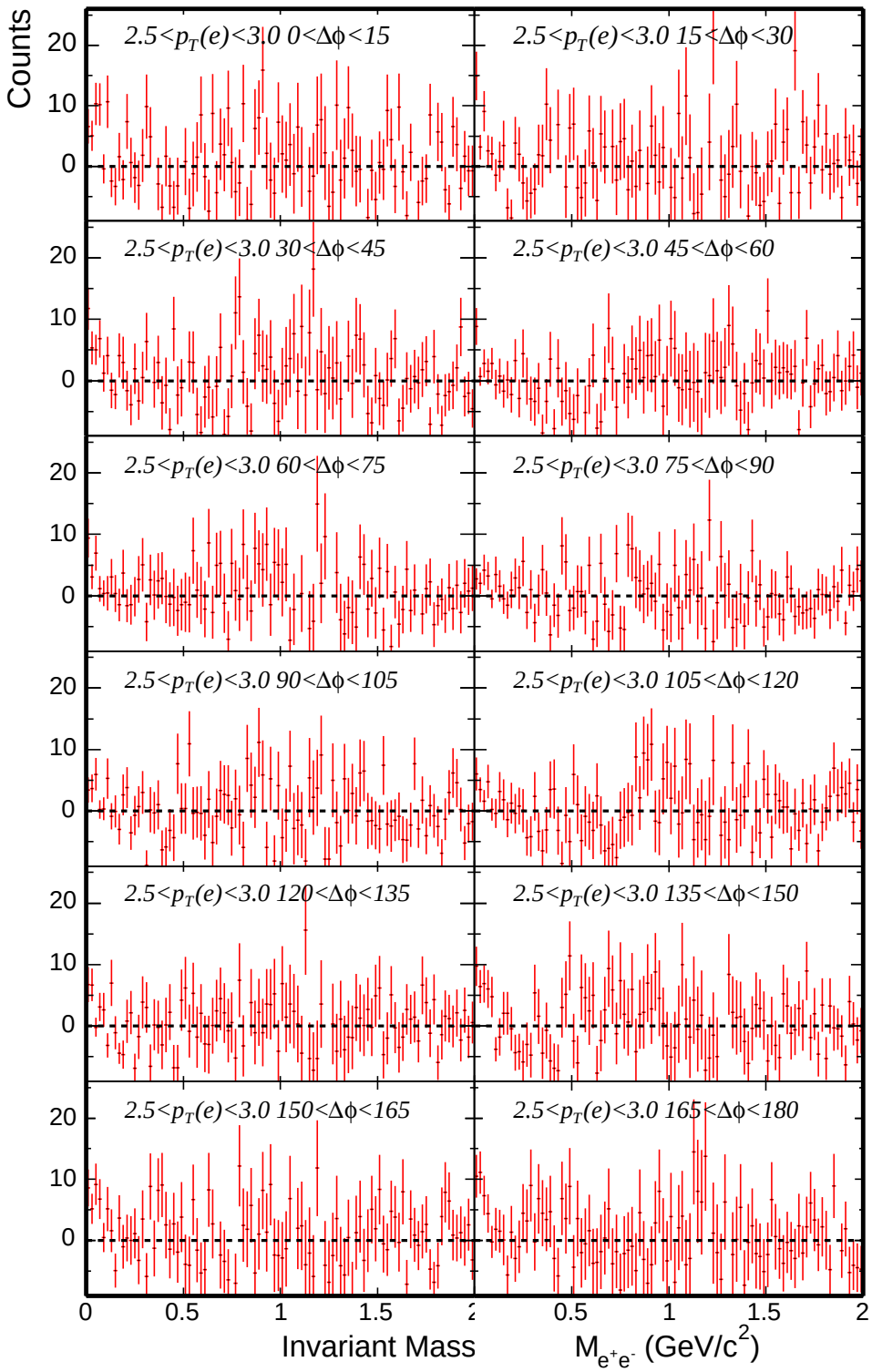

Figure 4.9: Invariant mass $M_{e^+e^-}$ distribution of combinatorial background subtract electron pair candidates in each $\Delta\phi$.

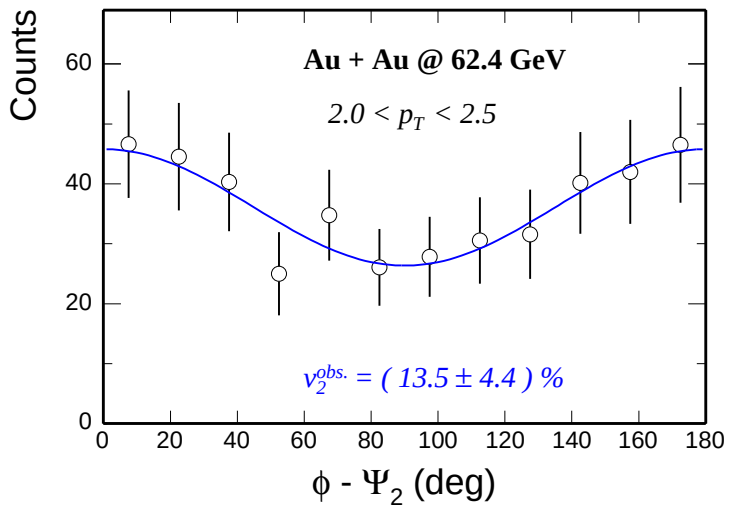

Figure 4.10: $\Delta\phi$ distribution of photonic electrons in $2.0 < p_T/(\mathrm{GeV/c}) < 2.5$. The distribution was fit to $[0] \times (1 + 2v_2^{obs.} \cos(2\Delta\phi))$ to extract the observed $v_2^{obs.}$.

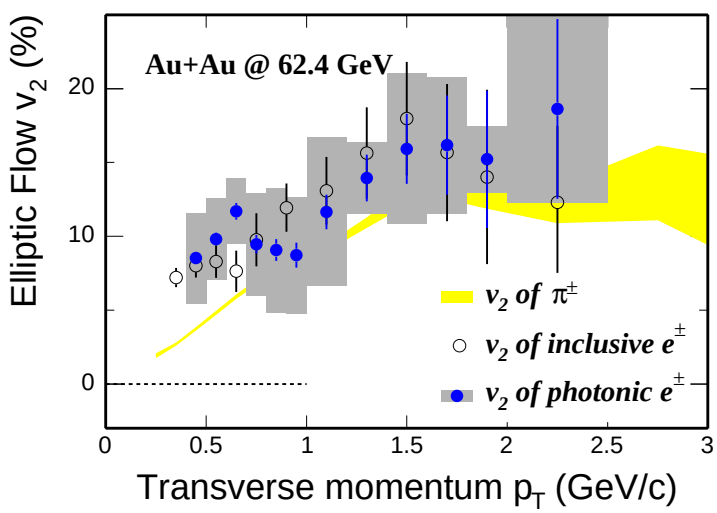

Figure 4.11: Inclusive electrons v_2 (from TOF trays) and photonic electrons v_2 (from the TPC) compared with charged $\pi^{\pm}$ v_2. The grey bands in each p_T bin for photonic electrons v_2 depict the systematic uncertainties from the combinatorial background estimation.

So the v_2^S, the elliptic flow of non-photonic electrons, can be calculated as

$$v_2^S = \frac{v_2^{tot} - f_B \times v_2^B}{f_S} \tag{4.13}$$

From above formula, the ratio of S/B is needed in this analysis. So the spectra analysis is necessary for the v_2 of non-photonic electrons.

A recent technique was developed to deal with such signal v_2 extraction from background [Sor04]. We can get the v_2 of inclusive electrons in different $M_{e^+e^-}$ bins $- v_2(M)$. And if we know the signal to background ration $r(M)$, then we can use two free parameters v_2^S and v_2^B to fit the $v_2(M)$. This statistical fit method looks promising in the v_2 calculation for V_0 particles, and $\pi^{\pm}$, p,$\bar{p}$ in dE/dx relativistical rising region. So this method is feasible for the extraction of photonic electrons v_2 out of the mixture with combinatorial background, and also that of non-photonic electrons v_2 out of inclusive electrons.

CHAPTER 5

Discussion

5.1 Open charm production in high energy collisions

5.1.1 Total charm cross section

As we discussed in the introduction chapter, the heavy quark total cross section measurement offers a powerful test for pQCD calculations. Since plenty of measurements were made at low energies while few were made at $\sqrt{s} > 100$ GeV, theoretical calculations are often tuned to match the low energy data points and then extrapolated to high energies. Because the parameters in the calculations (scales, heavy quark mass *etc.*) are not understood well yet in all energies, the predictions at high energies differ significantly. Fig. 5.1 shows almost all the total charm cross section measurements made so far compared with several theoretical calculations.

The low energy ($\sqrt{s}$ <100 GeV) data points were taken from the review paper [Tav87] (which summarized all the charm measurements before 1987) and from several experiments after 1988 (refer to [Adc02] for data points)[1]. A factor of 1.5 was applied on all these data points to include the contribution of $D_s^{\pm}$ and $\Lambda_c^{\pm}$ [FMN97]. We do not include total cross sections from those references that were extrapolated from high x_F and/or had extremely low efficiency from correlation measurements.(with extrapolation factor of $\gg 10$). The PHENIX and UA2 experiments extracted the cross section from the single electron spectrum in 130 GeV Au + Au and 630 GeV $p + \bar{p}$ collisions, respectively.

The lines depict different theoretical calculations and model fits. PYTHIA, a model

[1]Detailed data points selections are listed in Appendix C.

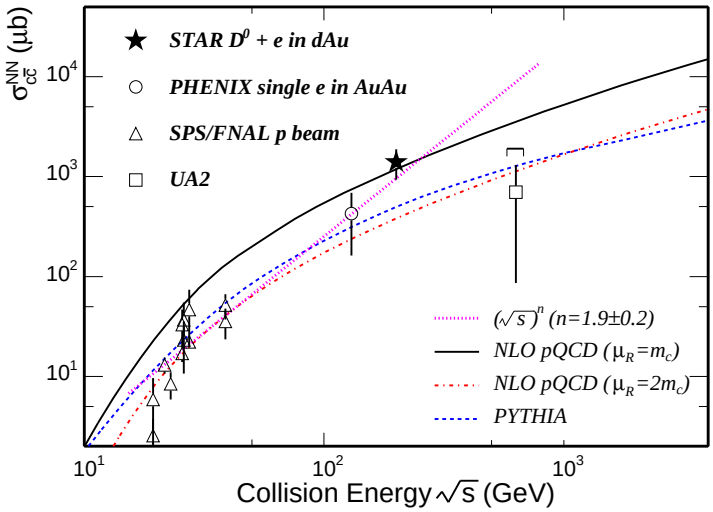

Figure 5.1: Total $c\bar{c}$ cross section per nucleon-nucleon collision vs. the collision energy ($\sqrt{s}$). The dashed line depicts a PYTHIA calculation with a specific set of parameters [Sj01]. The solid and dot-dashed lines depict two NLO pQCD calculations with MRST HO, $m_c = 1.2$ GeV/c^2, $\mu_F = 2m_c$ and specified μ_R shown on the plot [Vog02]. The dotted line (in pink) depicts a power law fit to the data points, with power $n \sim 2$.

based on pQCD calculations, is often used for predictions. The dashed line depicts a typical pQCD calculation with the only change of PDF from the default PYTHIA (CTEQ5L→CTEQ5M1). The result underpredicts the measurements at RHIC. Although the default PYTHIA takes initial radiation into account, high order processes seem to still not be well predicted. These include initial and final radiation, gluon splitting, and production through parton showers *etc.*. Recent analysis for CDF energy open beauty measurements showed these processes contribute a large fraction in the heavy flavor creation at Tevatron [Bus04]. This discrepancy indicates these processes may also play an important role at RHIC energy.

The two curves labeled "NLO pQCD" depict the full NLO pQCD calculations from [Vog02, Vog04]. "Full" means for both PDFs and differential cross sections. The red dot-dashed line shows a calculation tuned to the low energy data points. This calculation underpredicts our measurements at 200 GeV as well. The scale parameters used are $m_c = 1.2$ GeV/c^2, $\mu_F = \mu_R = 2m_c$. When the NLO pQCD calculation is carried out with $\mu_R = m_c$ instead of $2m_c$, it seems to reproduce the measurement at 200 GeV, but misses other data

points. An even smaller scale ($\mu_R = m_c/2$) was tried, but it overshoots our measurement by almost an order of magnitude. The K-factors in pQCD calculations also differ significantly when changing the scales [Vog02, Vog04]. As we know, when the scales go to $\sim$ 600 MeV, which is close to Λ_{QCD}, the feasibility of pQCD is doubtful. The discrepancy indicates these scales can be energy dependent.

On the other hand, recent π^0 spectrum measurements at both mid-rapidity [Adl03b] and forward rapidity [Ada04g] at RHIC seem to offer clear evidence that pQCD can reproduce the π^0 spectrum very well. This agreement even reaches as low as $p_T \sim 1$ GeV/c. Because of the large Q^2, one might naturally think the agreement for heavy flavor production should be better. However, our measurement indicates a negative result, which means there can be some differences in the calculations between light flavor hadrons and heavy flavor hadrons.

We fit a power law function to the data points in Fig. 5.1 and the result is depicted as a pink dotted line with the power $n \sim 1.9 \pm 0.2$. This power law dependence has already been proposed in [RRL03] and they gave the power $n \sim 1.6$. The power law dependence of charged hadron production ($n \sim 0.3$) has been observed in A + A collisions from AGS to RHIC [ABR03] and also predicted in the saturation approach [KL01]. Also for pion production, a linear scaling as a function of $F \equiv (\sqrt{s_{NN}} - 2m_N)^{3/4}/\sqrt{s_{NN}^{1/4}} \approx \sqrt{\sqrt{s_{NN}}}$ was observed [Afa02] in central A + A collisions, which is equivalent to a power law dependence of $\sqrt{s_{NN}}$ with $n \sim 0.5$. For the kaons that have strange valence quarks, similar scaling seems to hold from AGS to RHIC, but with a larger power value $n \sim 0.6 - 1$. Hence, this power scaling for charm quark production up to RHIC is not surprising. One interesting thing is that heavier quark production has a larger value of power, which may be caused by a threshold effect in the production: once the production channels are opened, or above and near production threshold, the total cross section distribution on different flavors is likely to favor heavier quarks.

Fig. 5.2 shows $d\sigma/dy$ compared to theoretical predictions with smaller systematic uncertainties. This figure shows clearly that the theoretical calculations underpredict out measurement.

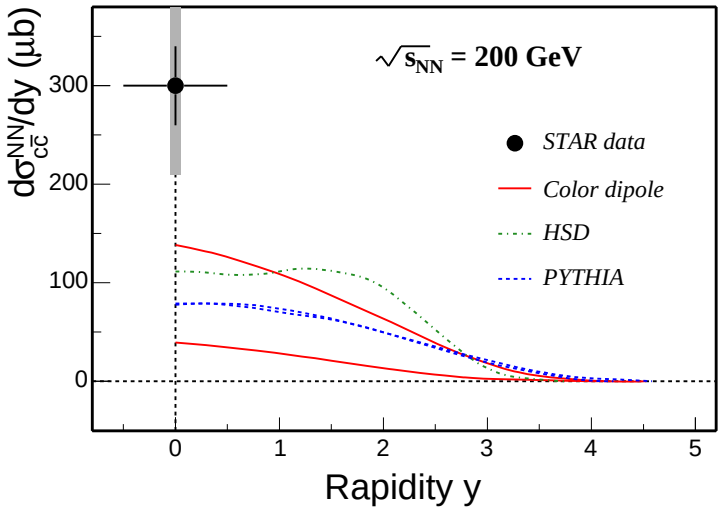

Figure 5.2: $d\sigma/dy$ of charm quarks from STAR measurement compared with different theoretical predictions [Vog04, RP03, BCH03].

5.1.2 Spectrum comparison

Open charm hadrons, including $D^0(K^-\pi^+)$, $D^{\star+}(D^0\pi^+)$, $D^+(K^-\pi^+\pi^+)$ and $D^0(K^-\pi^+\rho)$, were reconstructed directly in d + Au collisions (the measurements were statistically limited in $p+p$). A consistency check between the open charm spectrum and its expected semi-leptonic decay electron spectrum were made. The PYTHIA function for particle decay was used for generating the electron spectrum. The input open charm spectrum was fit to a power law function, and the parameters are [Tai04]: $dN/dy = 0.0265 \pm 0.0035$, $\langle p_T \rangle = 1.32 \pm 0.08$, and $n = 8.3 \pm 1.2$. Fig. 5.3 shows the electron spectra compared with the expected contribution from charm quark semi-leptonic decays. The bands include the uncertainties from those parameters. The comparison demonstrates a consistency between the two measurements.

There are already several electron spectra from charm semileptonic decay measurements. In Fig. 5.4 they are shown.

The comparison shows a continuous increase in the yields with the increase of beam energies. However, from RHIC 130 GeV to UA2 630 GeV, the errors on the data points conceal the detailed structure. Not only the total yield, but also the shape of the spectra seem to become harder with the increase of collision energy.

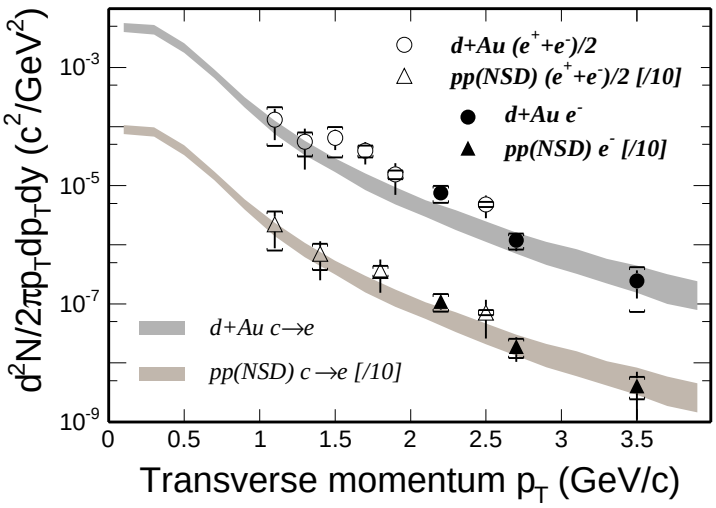

Figure 5.3: Non-photonic electron spectra compared with the expected ones from the semi-leptonic decays of measurement open charm spectrum.

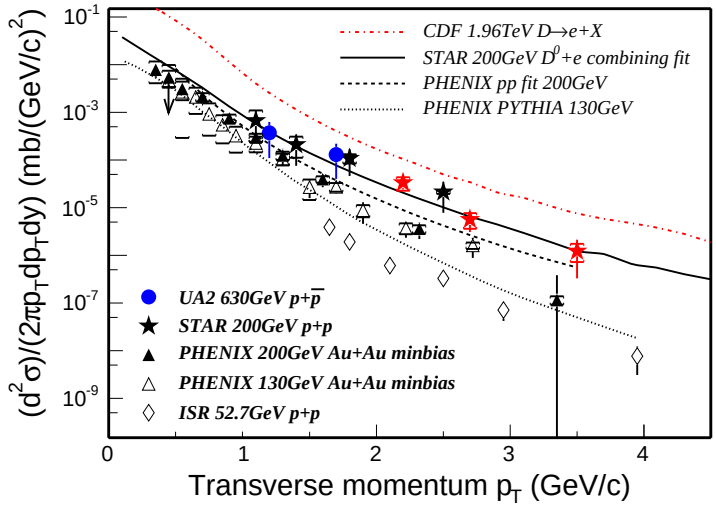

Figure 5.4: Non-photonic electron spectra from several collision energies and collision systems. Data points are taken from [B76, Adc02, Adl05, Bot90]. Curves are expected spectra from models or measured open charm spectrum.

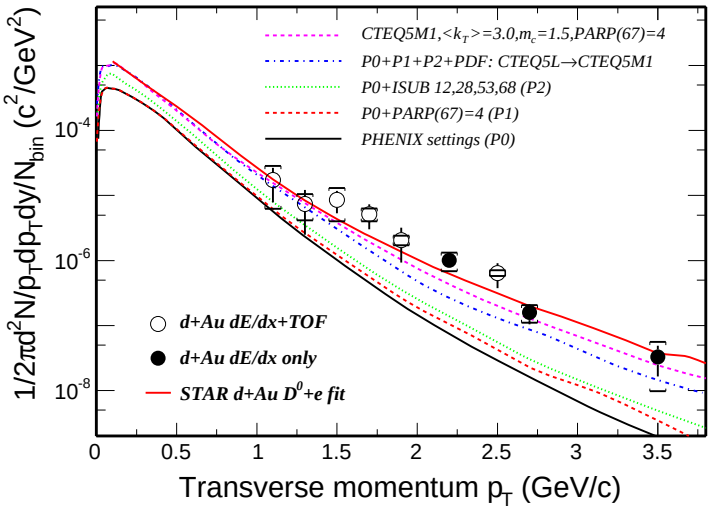

Figure 5.5: Measured non-photonic electron spectrum compared with PYTHIA calculations with different parameter settings at 200 GeV.

Fig. 5.5 shows a comparison of our measurement to PYTHIA calculations using different parameters. The PYTHIA calculation from the PHENIX 130 GeV Au + Au paper [Adc02] was used as a starting line (black solid curve). This calculation deviates significantly from the result of d + Au measurement at $\sqrt{s_{NN}}$ = 200 GeV: it shows a lower yield and a steeper p_T spectrum. Several parameters in PYTHIA were tuned to try to match our measurement: we increased the abundance of parton showers, we included higher order processes and gluon splitting processes, we changed the PDFs, we increased the initial $\langle k_T \rangle$ and we changed the charm quark mass. Although one of the calculations (red solid line) seems to match the spectrum, the large initial $\langle k_T \rangle$ requirement is questionable. Theoretical predictions [Vit03] as well as measurements show a much smaller $\langle k_T \rangle$ is needed for the 200 GeV d + Au system. In general, PYTHIA results seem to be hard to match to our measured spectrum.

In the above comparisons, we didn't change anything about the charm quark fragmentation function, which is a Peterson function in the default PYTHIA [Sj01]. The bare charm quark spectrum from PYTHIA seems to match the open charm measurement, which means a very hard fragmentation function (almost a δ function) is needed for charm quarks [Tai04] at RHIC energy. This may indicate that charm quark coalescence processes become competitive with fragmentation processes in the 200 GeV d + Au

system. A recent study shows this final state effect may play an important role through soft and shower recombination in d + Au collisions [HY04, Rua04b].

5.1.3 Bottom contribution

In the above discussions, the bottom contribution to the non-photonic electron spectrum was neglected. Since there is no bottom measurement around RHIC energy, this can only be studied through models. We used the default PYTHIA as a first estimation. Fig. 5.6 shows the results from this estimation where we used the scale $\sigma_{c\bar{c}} : \sigma_{b\bar{b}} = 400 : 1$ as the normalization [Vog02, RP03]. At p_T above 1 GeV/c, all the electrons from bottom are from direct semi-leptonic decays. This contribution is $\sim 25-40\%$ for $2 < p_T/(\mathrm{GeV/c}) < 3$ and $\sim 60-100\%$ for $3 < p_T/(\mathrm{GeV/c}) < 4$ to the charm contribution. The corresponding bottom contribution to the total non-photonic electrons is $\sim 20-30\%$ for $2 < p_T/(\mathrm{GeV/c}) < 3$ and $\sim 40-50\%$ for $3 < p_T/(\mathrm{GeV/c}) < 4$. If we subtract this estimated bottom contribution from our spectra, the change in the total cross section from a combined fit is ~ 0.09 mb, within the current statistical error of our result. This fraction is strongly model dependent however, so we didn't include the bottom contribution in the final calculation.

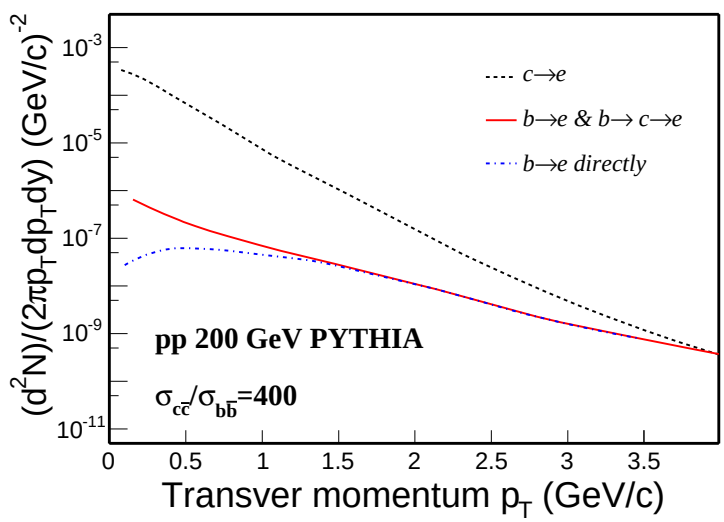

Figure 5.6: Comparison between the contributions from charm quarks and bottom quarks from the default PYTHIA.

We also tried several of the parameter settings from Fig. 5.6 to estimate the bottom contribution. Almost all these results show the bottom contribution will begin to overcome the charm contribution around $p_T \sim 3 - 4$ GeV/c. However, in these calculations, the heavy quark fragmentation functions have not been modified. As we discussed above, there is a hint that heavy quark may have a hard fragmentation function. In this case the difference of the fragmentation between charm quarks and bottom quarks may be much smaller than the default Peterson settings in PYTHIA. A recent study shows that under such assumptions, the bottom contribution on the electron spectrum does not overcome the charm contribution until $p_T \sim 10$ GeV/c [Lin04]. Precise measurements of heavy flavor spectra are needed to address these open issues.

5.1.4 Cronin effect of charm hadrons in d + Au

The well-known "Cronin effect" was named after the observation that particle (differential) cross sections depend on the atomic number (A) and the particle species from low energy p + A collisions [Cro73]. It is also characterized by the spectrum broadening in the intermediate p_T in p + A collisions compared to $p+p$ collisions. The initial projectile partons' multi-scattering with target partons has been proposed as an explanation for this effect [Wan00, Vit03]. However, a recent measurement on the pseudorapidity asymmetry of charged hadron spectra shows a contrary result with these model predictions. Another approach through the final state recombination of soft and shower partons seems to reproduce the identified particle spectra in d + Au collisions [Rua04b, HY04]. Measuring the Cronin effect of charm hadrons offers an additional opportunity to study the initial $\langle k_T \rangle$ broadening and coalescence of the final state charm quarks. Even though we don't have enough statistics to measure the charm hadron spectra in both d + Au and $p+p$ collisions, estimates of R^e_{dAu}, the nuclear modification factor of non-photonic electrons can give us some hints about these processes for charm hadrons.

Fig. 5.7 shows the R^e_{dAu} for $1 < p_T/(\text{GeV/c}) < 4$ compared with a theoretical prediction curve based on the initial multi parton scattering picture. We used the measured charm

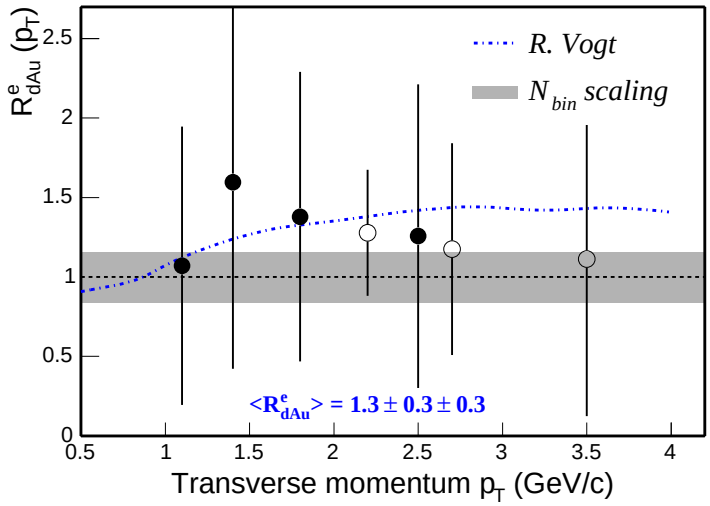

Figure 5.7: Cronin effect of non-photonic electrons in d + Au collisions, compared with the theoretical prediction of charm hadrons.

hadron spectrum in d + Au collisions and generated that in $p+p$ collisions according to the R^D_{dAu} from [Vog03]. Then we obtained the decayed electron spectra from both and calculated the predicted R^e_{dAu}. Due to poor statistics, the current measurement cannot give definite conclusions. The averaged R^e_{dAu} in $1 < p_T/(\mathrm{GeV/c}) < 4$ is $1.3 \pm 0.3 \pm 0.3$, which is consistent with N_{bin} scaling within present uncertainties.

5.2 Closed charm production

5.2.1 J/ψ production in $p+p$ collisions

The heavy quarkonia production mechanism in hadron hadron collisions is not well understood. Understanding this production mechanism in $p+p$ collisions is needed to search for J/ψ suppression as a signature of QGP formation in central Au + Au collisions at RHIC energy. Recent theoretical progress [NLC03] and the measurement from PHENIX collaboration [Adl04b] strongly support the *Color Octet Model* (COM) for J/ψ production in $p+p$ collisions at $\sqrt{s} = 200$ GeV. Fig. 5.8 shows the measured J/ψ production cross sections compared with the total charm quark pair production cross sections in different energies. The ratio of $\sigma_{J/\psi}/\sigma_{c\bar{c}}$ is on the order of 10^{-2} and shows a slight decrease from

low energies up to RHIC energy.

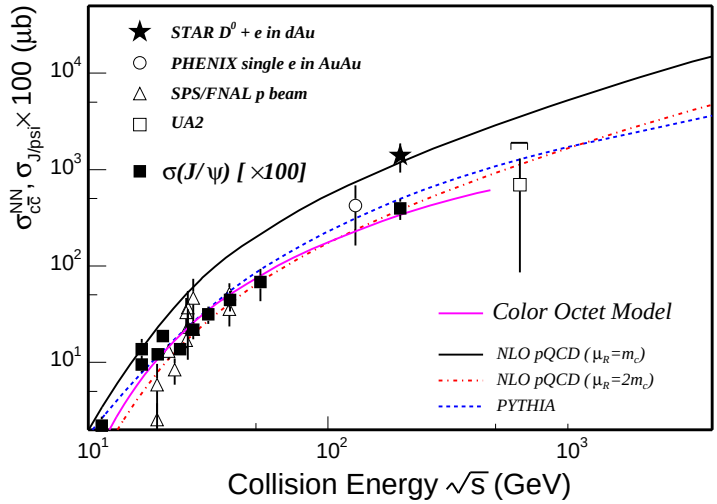

Figure 5.8: $\sigma_{J/\psi}$ as a function of collision energy in comparison to the total charm cross section. J/ψ production mechanism is proved to validate the COM model at RHIC energy.

5.2.2 J/ψ production in heavy ion collisions

In the hot dense QGP matter, the color screening effect is predicted to prevent heavy quark pairs from forming quarkonium bound states, and thus leads to a decrease of the ratio of closed charm (bottom) to open charm (bottom) [MS86]. This heavy quarkonium suppression has been proposed as a signature of QGP formation. In low energy SPS 17.2 GeV Pb + Pb collisions, the NA50 experiment reported a suppression of heavy quarkonium suppression relative to normal nuclear absorption. This was interpreted as an anomalous suppression due to the dissociation of $c\bar{c}$ pairs interacting with co-movers [Abr01].

In high energy heavy ion collisions, since there may be multiple $c\bar{c}$ pairs produced in a single collision, charmonium production through coalescence of charm quarks may become important: $D + \bar{D} \rightarrow J/\psi + X$. Since $c\bar{c}$ pairs are mostly produced from initial scatterings [Lin96], the partition of these charm quarks between open and closed ones is

deduced in statistical coalescence models [ABR03] from Eq. 5.1 .

$$N_{c\bar{c}}^{Tot} = \frac{1}{2}N_{oc} + N_{c\bar{c}} \tag{5.1a}$$

$$N_{oc} \propto g_c n_{oc} \tag{5.1b}$$

$$N_{c\bar{c}} \propto g_c^2 n_{c\bar{c}} \tag{5.1c}$$

In these models, the total charm yield is needed as an input to calculate g_c. The models often use $300 - 400$ μb for $\sigma_{c\bar{c}}$ at RHIC energy, which is a typical value from NLO pQCD calculations [MNR93, Vog02, RP03]. With this input, the statistical coalescence model, without any additional absorption effects, seems to agree with the J/ψ measurement in Au + Au collisions within errors [Adl04c]. However, if our measurement $\sigma_{c\bar{c}}^{NN} = 1.4$ mb is used as the input, assuming the statistical coalescence models work in central Au + Au collisions at RHIC and ignoring the absorption effect, one would expect at least a factor of 3 increase above the number of binary scaling in the J/ψ yield in central Au + Au collisions. The upper limit from PHENIX measurement on J/ψ production in central Au + Au collisions seems to invalidate this expectation.

Additional improvements for the nucleon absorption effects on J/ψ were taken into account in [GR01]. But in central collisions, the production through coalescence can still make up a significant portion of the total production. Fig. 5.9 shows the predictions from different calculations.

From Fig. 5.9, because of the dominant contribution from charm quark recombination, the expected J/ψ yield in central Au + Au collisions inferred from our d + Au result is still significantly higher than expectations from number of binary scaling. Even when nuclear effects in the d + Au system are taken into account, which means $\sigma_{c\bar{c}} \sim 1.0$ mb is used as the input, this prediction is still above number of binary scaling. In the QGP, due to color screening, the J/ψ yield will be suppressed comparing to N_{bin} scaling. Since most of the suppression will occur at low p_T , the $\langle p_T \rangle$ of J/ψ will be efficiently increased. On the other hand, if the QGP is formed, partons will reach kinetic equilibrium [ABR03] and charm quark coalescence will be important for J/ψ production, the J/ψ yield will be

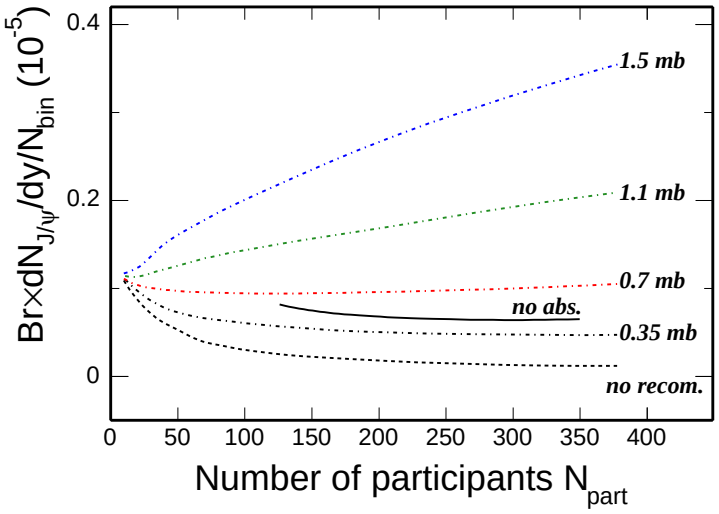

Figure 5.9: J/ψ yields from models as a function of number of participants. The black dashed curve depicts a calculation only includeing J/ψ absorption effects, and no recombination effects from [Gra04] with $\sigma_{c\bar{c}} = 0.35$ mb. The black solid curve depict a calculation from statistical coalescence model and there is no absorption effect in it [ABR03] with $\sigma_{c\bar{c}} = 0.39$ mb. The dot-dashed lines depict several calculations including both absorption and recombination effects with different cross sections as input [Gra04].

"enhanced" in this case. Furthermore, the J/ψ from coalescence production will have a larger $\langle p_T \rangle$ than those from direct production. Therefore, both enhancements in the J/ψ yield and $\langle p_T \rangle$ could be a good signature for QGP production at RHIC. The combination of the suppression and possible coalescence enhancement will, in principle, further enforce this argument. However, the energy loss of initially produced heavy quarks traversing the medium might complicate this picture. Detailed analysis of J/ψ yields as well as transverse momentum distributions are necessary in order to distangle the problem.

5.3 Elliptic flow of charm quarks and thermalization

In heavy ion collisions, the momentum-space azimuthal anisotropy can reveal the early stage system information [ZGK99]. The large v_2 measured for multi-strange hadrons and the NCQ scaling of hadrons at intermediate p_T indicate a partonic level collectivity has been developed in Au + Au collisions at RHIC. However, partonic collectivity is necessary but not sufficient to show that local thermal equilibrium has been established. Parton

thermalization is crucial to demonstrate the discovery of QGP in heavy ion collisions at RHIC.

Charm quarks are believed to be mostly produced through initial scatterings. Hence the study of elliptic flow of charm quarks may give us some hints of properties of the produced matter in heavy ion collisions. Charm quarks, because of their heavy masses, need many more rescatterings to develop flow similar to light quarks (u, d, s). If charm quarks flow as much as light quarks, this may tell us there are frequent rescatterings happening between the light quarks and thus provide a strong clue to illustrate the thermalization of the light (u, d, s) quarks [DES04].

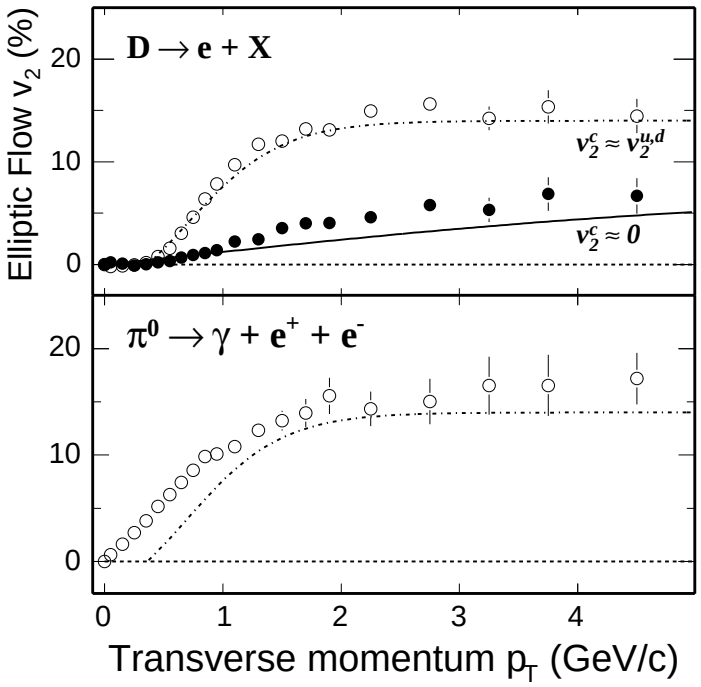

Figure 5.10: v_2 of electrons from the decays of charm hadrons and π^0. Lines depict the input D or π^0 v_2 while the points depict the v_2 of decay electrons. Upper panel: the input D v_2 are assumed as $v_2^c \approx v_2^{u,d}$ (dot-dashed line) and $v_2^c \approx 0$ (solid line), respectively. Bottom panel: the input $v_2(\pi^0)$ (dot-dashed line) is from 200 GeV measurement.

At present, the direct reconstruction of open charm hadrons uses a mixed-event method. In this method, there are huge combinatorial backgrounds under the signal peaks, which leads to large uncertainties to extract v_2 from this method. A new way to measure the charm quark v_2 is to measure the v_2 of their semi-leptonic decayed electrons.

Fig. 5.10 upper panel shows the input open charm hadron v_2 and decayed electron v_2 when charm quarks flow or not. About 50 M D^0s were input into PYTHIA to obtain the decayed electrons. The shape of the D^0 p_T spectrum is a power law function which we discussed before. The results show that, at p_T above 2 GeV/c, the electrons will carry almost all the saturated v_2 of open charm hadrons [DES04] and the electron v_2 can distinguish between $v_2^c \approx v_2^{u,d}$ and $v_2^c \approx 0$. This demonstrates that measuring non-photonic electron v_2 for p_T above 2 GeV/c is a feasible and efficient way to measure the charm quark v_2 [BKG03, DES04].

Neutral pion decay is the dominant background source in the single electron analysis. The two photon processes are followed by conversion into electrons in the detector, and the rate of conversion depends on detector materials. These background electrons can be rejected by a topological method [Joh02]. The remaining dominant background source is π^0 Dalitz decay, which can only be subtracted statistically. The bottom panel of Fig. 5.10 shows the electron v_2 from π^0 Dalitz decays. The background electron flow leads to large uncertainties in the statistical subtraction.

Electrons from heavy flavor decays begin to dominate the electron spectrum above $p_T \sim 3$ GeV/c. With the knowledge of the pion yield, D-meson yield, the pion v_2, and the electron v_2, it is possible to extract the D-meson v_2. These measurements can be made by both the PHENIX and STAR collaborations at RHIC. Direct photon v_2 can also be measured with this method.

CHAPTER 6

Outlook

6.1 Detector upgrade proposals

STAR has proposed two important sub-detector upgrades: a full barrel Time-Of-Flight (TOF) detector [STA04] and a Heavy Flavor Tracker (HFT) [STA05].

The proposed full barrel TOF detector would surround the outer edge of the TPC, and cover $-1 < \eta < 1$ and $\sim 2\pi$ in azimuth. By using the recently developed technology - MRPC, the TOF system can achieve the required timing resolution < 100 ps and the required particle detecting efficiency $> 95\%$. This will significantly improve the STAR PID capability: π/K can be separated to 1.8 GeV/c and p/meson can be separated up to ~ 3 GeV/c. The TOF detector allows us to greatly reduce the integrated luminosity needed for key measurements (collectivity, elliptic flow *etc.*), to significantly extend the p_T reach of resonance measurements, and to study large and small scale correlations and fluctuations *etc.*. Good performance of the prototype TOF detector (TOFr) in Run III and Run IV strongly offers us confidence about the full coverage barrel TOF detector.

The Heavy Flavor Tracker detector will be placed between the beam pipe and the SVT detector. It will retain the (p_T, η) coverage of the current TPC and have two layers of silicon pixel detectors. The 10 μm vertex resolution provided by the HFT will allow us to reconstruct open charm and bottom hadrons directly and make high precision measurements of p_T spectra, particle ratios, azimuthal anisotropy *etc.*. With the help of the SVT, it can be used to remove photon conversion electrons, which will make the measurement of the low mass e^+e^- spectrum possible.

At RHIC, several key measurements such as jet quenching, bulk collective motion, and

partonic collectivity *etc.* have provided strong hints for the discovery of QGP. However, at least two remaining critical points need to be demonstrated: whether the system is thermalized and whether the chiral symmetry is restored? These two sub-detector upgrade will help us to understand these questions and the two following measurements should be investigated.

6.2 Open charm measurements

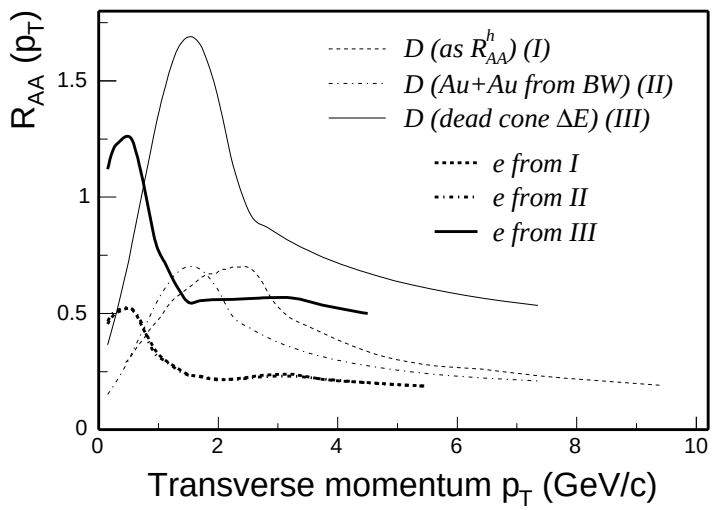

Figure 6.1: R_{AA} of charm hadrons (thin lines) and decayed electrons (thick lines) for several assumed D spectra in Au + Au central collisions. The baseline used in $p+p$ collisions is from STAR d + Au measurement. The thin dashed line depicts the R_{AA} of D with the same behavior as charged hadrons. The thin dot-dashed line is for D with $T_{fo} = 160$ MeV and $\langle\beta_T\rangle = 0.4$ c blast wave behavior in low p_T and with the same R_{AA} as charged hadron in high p_T . The thin solid line is for D with the same BW parameters as the dot-dashed line in low p_T , but the total yield of D is assumed to obey N_{bin} scaling. While in high p_T , the R_{AA} is taken from dead-cone energy loss calculation [DG04]. Thick lines depict the electron distributions from the corresponding D distribution with the same line style.

In the previous discussion, we proposed the measurement of charm azimuthal anisotropy through its semi-leptonic decay channel. However, the decay kinematics can smear the spectra differences. So it is hard to study charm meson radial flow or hydrodynamic behavior through its semi-leptonic decay channel. Fig. 6.1 shows R_{AA} of charm hadrons and decayed electrons for several assumed D spectra in Au + Au central collisions. The

difference between the solid black line and the dashed black line for D is visible and it can be attributed to the smaller collectivity of charm hadrons due to heavy masses. But this difference is washed out by the decay kinematics and it is hard to tell the magnitude of charm hadron collectivity from decayed electron spectra.

At high p_T, heavy quark may lose less energy due to the "dead-cone" effect [DK01, DG04]. A precise charm-decayed electron spectrum measurement may give us some hints from the suppression factor. But, the contribution to electrons from bottom decays may become significant above 3 GeV/c and bottom quarks are expected to lose much less energy. As such, the electron spectrum suppression at high p_T is hard to interpret in terms of charm hadrons and/or bottom hadrons separately. So the direct charm spectrum measurement is crucial to answer the hydrodynamic behavior and "dead-cone" effect of charm hadrons. Together with those measurements for light hadrons, we can understand the properties of the hot dense matter created in heavy ion collisions.

Measured light hadron (u, d, s) yields and their ratios, from AGS to RHIC energies, have been well described in statistical models [Bra01]. Precise measurement on charm hadron yields and their ratios can help us understand the charm quark chemistry and the kinematical equilibration property of charm quarks in the medium. Meanwhile, since the charm quark yield is quite high at RHIC energy, coalescence models predict significantly different ratios of different charm hadrons [RS03]. Furthermore, the standard J/ψ suppression scenario may be modified when thermally produced J/ψ become significant. Precise measurements on these sensitive probes: D_s^+/D^0, D_s^+/D^+ and $J/\psi/D^0$ are needed to distinguish different pictures [STA05]. Table. 6.1 shows the events needed to observe 3σ D^0 and D_s^+ signals with different detector configurations. With the help of TOF and HFT detectors, these precise measurements become feasible.

The development of elliptic flow requires frequent rescatterings between components. Identified particle elliptic flow measurements show strong evidence that a partonic level collectivity has been established in Au + Au collisions at RHIC energy. However, it is still not sufficient to prove that the system is thermalized. Charm quarks are abundantly produced at RHIC energies. Due to their large masses and expected smaller hadronic

Table 6.1: Number of events needed to observe 3σ D^0 and D_s^+ signals in Au + Au 200 GeV collisions with different detectors configurations.

	D^0	D_s^+
TPC+SVT	12.6 M	500 M ($K_S^0 + K^+$)
TPC+SVT+TOF	2.6 M	100 M
TPC+SVT+TOF+HFT	5 K (Minuit)	700 K (Minuit $\phi + \pi^+$)

rescattering cross sections, non-zero charm quark flow would provide a strong indication that light quarks (u, d, s) are thermalized. Although an electron v_2 measurement can provide an indirect effective method, the technical systematics need to be understood very well before we can draw conclusions. A precise direct measurement of the charm hadron flow up to intermediate p_T can be achieved with the upgraded detectors TOF and HFT. Simulations show the statistical errors can reach $\sim 2-3\%$ at $p_T \sim 5$ GeV/c in one year of Au + Au run.

6.3 Low mass e^+e^- spectrum

Electromagnetic probes have great advantages to investigate the early stage information of the system compared to hadronic probes because they don't have strong interactions with the final state system. The di-electron invariant mass $M_{e^+e^-}$ distribution has been proposed as a unique tool to study the properties of vector mesons (ρ, ω, ϕ, J/ψ *etc*) in-medium effect during heavy ion collisions. This is directly connected with the QGP signature − chiral symmetry restoration by measuring the mass position change of these vector mesons. Once the broken chiral symmetry is restored, $\langle\bar{\psi}\psi\rangle$ becomes 0 and the quark mass coupling with the Higgs field decreases to 0. This is a robust proof of the discovery of QGP.

This measurement has been carried out in low energy Pb + Au collisions at SPS. CERES/NA45 studied the e^+e^- invariant mass spectrum with projectile beams of 40A GeV and 158A GeV. They observed an excess in the di-electron spectrum compared to light hadron decays and attributed it to in-medium modifications of the ρ meson due to

the restoration of approximate chiral symmetry [Ada03a]. However, the data points from SPS have large errors both statistically and systematically, so we cannot draw a strong conclusion from them so far. In the phase diagram shown in Fig. 1.4, the SPS machine sits near the crossover boundary of the phase transition into QGP. While the T_{ch} is higher and μ_B is lower in RHIC, this signal should be easier to observe. Since almost all other RHIC measurements indicate the formation of QGP, a precise measurement of the low mass e^+e^- spectrum at RHIC energy is likely to be interesting.

This measurement needs both detector upgrade. By combining TOF and dE/dx in the TPC, electrons can be identified. This has been demonstrated in Fig. 3.1 and 3.19. Background electrons from photon conversion and light hadron decays were studied in the simulations. Fig. 6.2 shows the simulated electron pair invariant mass distributions for those pairs from different sources in $\sim$ 1 M PYTHIA + GEANT simulation events. The background level in the interesting ω, ρ mass region is shown in Table.6.2.

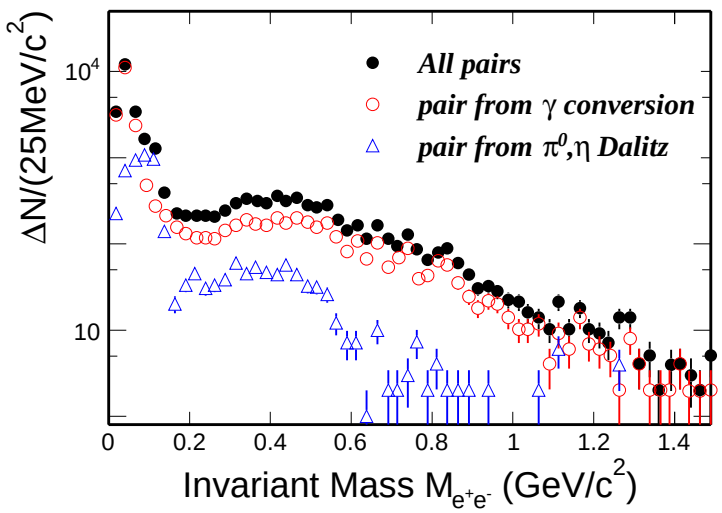

Figure 6.2: $M_{e^+e^-}$ of electron pairs from PYTHIA + GEANT simulations for those from all sources (black solid circles), photon conversion only (red open circles) and π^0,η Dalitz decays (blue triangles).

Table 6.2: Electron pair contribution from background

	ω	ϕ
Total bkgd	$10^{-4}/(25\ \mathrm{MeV/c^2})$	$2\times10^{-5}/(25\ \mathrm{MeV/c^2})$
π^0 Dalitz	$5\times10^{-6}/(25\ \mathrm{MeV/c^2})$	$5\times10^{-7}/(25\ \mathrm{MeV/c^2})$

According to the material properties of the detectors and also from simulations, photon conversions mostly happen in the SVT, especially the first layer of the SVT (out of three). So requiring charged particle hits in the SVT and HFT will significantly remove the photon conversion electrons. Fig. 6.3 shows the electron p_T distribution from photon conversions with a 25-TPC-hit cut only (black), a 25-TPC-hit and a 2-SVT-hit cut (red) and a 25-TPC-hit, a 2-SVT-hit cut and a 2-HFT-hit cut (blue). With the help of SVT and HFT, $\sim$ 98% of conversion electrons can be removed. In this case, the π^0 will become the dominant background source for primary electrons.

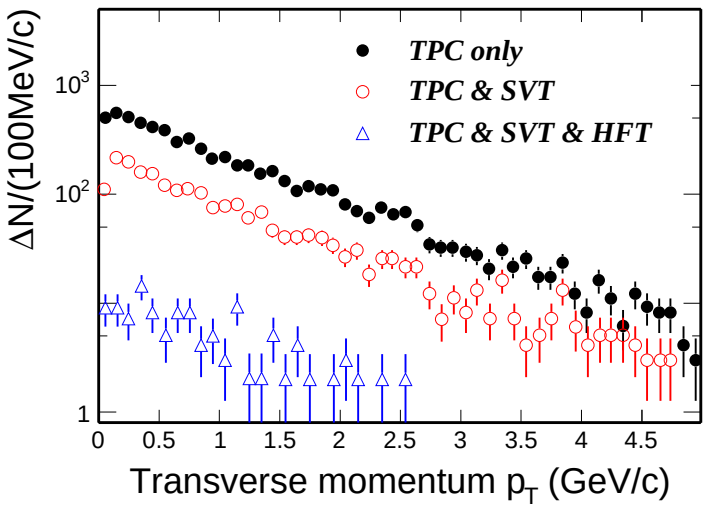

Figure 6.3: Electrons from photon conversion p_T spectrum for a 25-TPC-hit and a 2-SVT-hit cut (red) and a 25-TPC-hit, a 2-SVT-hit cut and a 2-HFT-hit cut (blue). Only $\sim$ 2% of total electrons from photon conversion are left with combined TPC+SVT+HFT cut.

Furthermore, we can estimate the number of events needed to observe the vector meson signals under different background levels. From previous measurements and model simulations, we assume that $dN^{\pi}/dy \approx 1$ in 200 GeV $p+p$ collisions and $dN^{\pi}/dy \approx 300$ in Au + Au collisions; $\omega/\pi \approx 0.15$, $\phi/\pi \approx 0.02$, $\sigma_{\omega} \approx 10$ MeV/c^2, $\sigma_{\phi} \approx 8$ MeV/c^2 from simulations; The matching and electron PID efficiency with TOF+dE/dx method is $\sim$ 80% and the matching efficiency of the combined TPC+SVT+HFT is $\sim$ 60%. Then to observe 3σ signals for the ω and ϕ, the number of events of Au + Au collisions needed are shown in Table. 6.3.

Table 6.3: Number of events needed to observe 3σ ω and ϕ signals in Au + Au 200 GeV collisions with different detectors configurations.

	ω	ϕ
TPC+TOF	7 M	2 M
TPC+TOF+SVT+HFT	800 K	150 K

The measurements of vector mesons through electromagnetic decay channels can shed light on whether chiral symmetry which is broken in QCD vacuum is restored in the QGP, and furthermore indicate the origin of mass in nature.

APPENDIX A

QCD Lagrangian

A.1 Notations

We use the *natural units* throughout this thesis: $c = \hbar = k_B = 1$.

In the following part, we define the *contravariant vectors* in for space-time coordinates and 4-momentum vector in the Minkowski space.

$$x^\mu = (x^0, x^1, x^2, x^3) = (t, \boldsymbol{x}) = (t, x, y, z) \tag{A.1}$$

$$p^\mu = (p^0, p^1, p^2, p^3) = (E, \boldsymbol{p}) = (E, \boldsymbol{p_T}, p_z) = (E, p_x, p_y, p_z) \tag{A.2}$$

The space-time *metric tensor* $g_{\mu\nu}$ is:

$$g_{\mu\nu} = g^{\mu\nu} = \begin{pmatrix} 1 & 0 & 0 & 0 \\ 0 & -1 & 0 & 0 \\ 0 & 0 & -1 & 0 \\ 0 & 0 & 0 & -1 \end{pmatrix} \tag{A.3}$$

The *covariant vector* is related to the contravariant vector through $g_{\mu\nu}$ by

$$x_\mu = g_{\mu\nu} x^\nu \tag{A.4}$$

and conversely,

$$x^\mu = g^{\mu\nu} x_\nu \tag{A.5}$$

In this thesis, we use the notation that a repeated index implies a summation with respect

to that index, unless indicated otherwise. The scaler product of two vectors a and b is defined as:

$$a \cdot b \equiv a^\mu b_\mu = g_{\mu\nu} a^\mu b^\nu = a^0 b^0 - \boldsymbol{a} \cdot \boldsymbol{b} \tag{A.6}$$

The gradient operator ∂_μ is the derivative with respect to x^μ:

$$\partial_\mu = \frac{\partial}{\partial x^\mu} \tag{A.7}$$

The four-momentum operator p^μ in coordinate representation is

$$p^\mu = i\partial^{mu} = ig^{\mu\nu}\partial_\nu = ig^{\mu\nu}\frac{\partial}{\partial x^\nu} = (i\frac{\partial}{\partial x^0}, -i\frac{\partial}{\partial x^1}, -i\frac{\partial}{\partial x^2}, -i\frac{\partial}{\partial x^3}) \tag{A.8}$$

It is convenient to work with gamma matrices γ^μ later. They satisfy the anticommutation relation

$$\{\gamma^\mu, \gamma^\nu\} \equiv \gamma^\mu\gamma^\nu + \gamma^\nu\gamma^\mu = 2g^{\mu\nu} \tag{A.9}$$

A.2 $SU(3)_C$ invariant QCD Lagrangian

We denote q_f^α a quark field with color α and flavor f and adopt a vector notation in color space: $q_f \equiv column(q_f^1, q_f^2, q_f^3)$. The free Lagrangian is written as:

$$\mathcal{L}_0 = \sum_f \bar{q}_f(i\gamma^\mu\partial_\mu - m_f)q_f \tag{A.10}$$

It is invariant under arbitrary global $SU(3)_C$ transformations in color space:

$$q_f^\alpha \to (q_f^\alpha)' = U_\beta^\alpha q_f^\beta, \qquad UU^\dagger = U^\dagger U = 1, \qquad \det U = 1 \tag{A.11}$$

The $U(3)_C$ matrices can be written as

$$U = \exp\left(-ig_s\frac{\lambda^a}{2}\theta_a\right) \tag{A.12}$$

where λ^a $(a = 1, 2, ..., 8)$ denote the generators of the fundamental representation of the $SU(3)_C$ algebra, and θ_a are arbitrary parameters. In $SU(3)_C$, the matrices λ^a correspond to the eight Gell-Mann matrices and they satisfy the commutation relations

$$[\lambda^a, \lambda^b] \equiv \lambda^a \lambda^b - \lambda^b \lambda^a = 2if^{abc}\lambda^c \tag{A.13}$$

with f^{abc} structure constants, which are real and totally antisymmetric.

As in the QED case, to satisfy the invariance under *local* $SU(3)_C$ transformations: $\theta_a = \theta_a(x)$, 8 independent gauge bosons $G^\mu_a(x)$ - *gluons* are introduced. Define:

$$D^\mu q_f \equiv \left[\partial^\mu - ig_s \frac{\lambda^a}{2} G^\mu_a(x)\right] q_f \equiv [\partial^\mu - ig_s G^\mu(x)] q_f \tag{A.14}$$

To require $D^\mu q_f$ to transform in exactly the same way as q_f, the transformation properties of the gauge fields under an infinitesimal $SU(3)_C$ transformation:

$$G^\mu_a \to (G^\mu_a)' = G^\mu_a - \partial^\mu(\delta\theta_a) + g_s f^{abc}\delta\theta_b G^\mu_c \tag{A.15}$$

Unlike the QED case, the non-commutativity of the $SU(3)_C$ matrices gives rise to an additional term involving the gluon fields themselves. To build a gauge invariant kinetic term for the gluon fields, the field strengths were introduced:

$$\begin{gathered} G^{\mu\nu}(x) \equiv \frac{i}{g_s}[D^\mu, D^\nu] = \partial^\mu G^\nu - \partial^\nu G^\mu - ig_s[G^\mu, G^\nu] \equiv \frac{\lambda^a}{2} G^{\mu\nu}_a(x) \\ G^{\mu\nu}_a(x) = \partial^\mu G^\nu_a - \partial^\nu G^\mu_a + g_s f^{abc} G^\mu_b G^\nu_c \end{gathered} \tag{A.16}$$

The final $SU(3)_C$ invariant QCD Lagrangian is:

$$\mathcal{L}_{QCD} \equiv -\frac{1}{4} G^{\mu\nu}_a G^a_{\mu\nu} + \sum_f \bar{q}_f (i\gamma^\mu D_\mu - m_f) q_f \tag{A.17}$$

It is worthwhile to decompose the Lagrangian into different pieces:

$$\begin{aligned}\mathcal{L}_{QCD} = &-\frac{1}{4}(\partial^\mu G_a^\nu - \partial^\nu G_a^\mu)(\partial_\mu G_\nu^a - \partial_\nu G_\mu^a) + \sum_f \bar{q}_f^\alpha (i\gamma^\mu \partial_\mu - m_f) q_f^\alpha \\ &+ g_s G_a^\mu \sum_f \bar{q}_f^\alpha \gamma_\mu \left(\frac{\lambda^a}{2}\right)_{\alpha\beta} q_f^\beta \\ &- \frac{g_s}{2} f^{abc}(\partial^\mu G_a^\nu - \partial^\nu G_a^\mu) G_\mu^b G_\nu^c - \frac{g_s^2}{4} f^{abc} f_{ade} G_b^\mu G_c^\nu G_\mu^d G_\nu^e\end{aligned} \tag{A.18}$$

The first line contains the correct kinetic terms for different fields. The second line shows the color interaction between quarks and gluons. In the last line, owing to the non-abelian character of the $SU(3)_C$ group, the $G_a^{\mu\nu} G_{\mu\nu}^a$ term generates the cubic and quartic gluon self-interactions.

A.3 Chiral symmetry and effective chiral Lagrangian

In the absence of quark masses, the QCD Lagrangian can be written:

$$\mathcal{L}_{QCD} \equiv -\frac{1}{4} G_a^{\mu\nu} G_{\mu\nu}^a + i\bar{q}_L \gamma^\mu D_\mu q_L + i\bar{q}_R \gamma^\mu D_\mu q_R \tag{A.19}$$

. It is invariant under independent *global* $G \equiv SU(N_f)_L \otimes SU(N_f)_R$ transformations of the left-and right-handed quarks in flavor space:

$$q_L \xrightarrow{G} g_L q_L, \qquad q_R \xrightarrow{G} g_R q_R, \qquad g_{L,R} \in SU(N_f)_{L,R} \tag{A.20}$$

This chiral symmetry, which should be approximately good for light quark sector (u, d, s), is however not seen in the hadronic spectrum. Moreover, the octet of pseudoscalar mesons are much lighter than all the other hadronic states. Hence, the ground state of the theory (the vacuum) should not be symmetric under the chiral group. In the Goldstone's theorem, an octet of pseudoscalar massless bosons is introduced and the

symmetry $SU(3)_L \otimes SU(3)_R$ spontaneously breaks down and the quark condensate

$$v \equiv \langle 0|\bar{u}u|0\rangle = \langle 0|\bar{d}d|0\rangle = \langle 0|\bar{s}s|0\rangle < 0 \tag{A.21}$$

The Goldstone nature of the pseudoscalar mesons implies strong constraints on their interactions, which can be most easily analyzed on the basis of an effective Lagrangian. The Goldstone boson fields can be collected in a 3×3 unitary matrix $U(\phi)$.

$$\langle 0|\bar{q}_L^j q_R^i|0\rangle \to \frac{v}{2} U^{ij}(\phi) \tag{A.22}$$

A convenient parametrization is given by

$$U(\phi) \equiv \exp(i\sqrt{2}\Phi/f) \tag{A.23}$$

$$\Phi(x) \equiv \frac{\overrightarrow{\lambda}}{2}\overrightarrow{\phi} = \begin{pmatrix} \frac{\pi^0}{\sqrt{2}} + \frac{\eta_8}{\sqrt{6}} & \pi^+ & K^+ \\ \pi^- & -\frac{\pi^0}{\sqrt{2}} + \frac{\eta_8}{\sqrt{6}} & K^0 \\ K^- & \bar{K}^0 & -\frac{2\eta_8}{\sqrt{6}} \end{pmatrix} \tag{A.24}$$

The matrix $U(\phi)$ transforms linearly under the chiral group, but the induced transformation on the Goldstone fields $\overrightarrow{\phi}$ is highly non-linear.

We should write the most general Lagrangian involving the matrix $U(\phi)$ and organize it in terms of increasing powers of the momentum or, equivalently, in terms of an increasing number of derivatives:

$$\mathcal{L}_{eff}(U) = \sum_n \mathcal{L}_{2n} \tag{A.25}$$

The terms with a minimum number of derivatives will dominate in the low energy domain. To lowest order, the effective chiral Lagrangian is uniquely given by the term

$$\begin{aligned} \mathcal{L}_2 &= \frac{f^2}{4}\mathrm{Tr}[\partial_\mu U^\dagger \partial^\mu U] \\ &= \frac{1}{2}\mathrm{Tr}[\partial_\mu \Phi \partial^\mu \Phi] + \frac{1}{12f^2}\mathrm{Tr}[(\Phi \overleftrightarrow{\partial}_\mu \Phi)(\Phi \overleftrightarrow{\partial}_\mu \Phi)] + \mathcal{O}(\Phi^6/f^4) \end{aligned} \tag{A.26}$$

The non-linearity of the effective Lagrangian relates amplitudes with different numbers of Goldstone bosons, allowing for absolute predictions in terms of f.

Considering the quark masses, the corrections induced by the non-zero masses are taken into account through the term

$$\begin{aligned} \mathcal{L}_m &= \frac{|v|}{2}\mathrm{Tr}[\mathcal{M}(U+U^\dagger)], \qquad \mathcal{M} \equiv \mathrm{diag}(m_u, m_d, m_s) \\ \mathcal{L}_m &= |v|\left\{-\frac{1}{f^2}\mathrm{Tr}[\mathcal{M}\Phi^2] + \frac{1}{6f^4}\mathrm{Tr}[\mathcal{M}\Phi^4] + \mathcal{O}(\Phi^6/f^6)\right\} \end{aligned} \tag{A.27}$$

The relation between the physical meson masses and the quark masses can be obtained rom the trace in the quadratic mass term. Although the absolute values of the quark masses cannot be fixed from this approach because of the factor $|v|/f$ in each mass, one can obtain information about quark mass ratios after taking out this common factor. One of the famous ratios advocated by Weinberg is:

$$m_u : m_d : m_s = 0.55 : 1 : 20.3 \tag{A.28}$$

APPENDIX B

Kinematic variables

Let us introduce several useful kinematic variables in hadron-hadron interactions.

- Bjorken x, $x_{Bjorken} \equiv \dfrac{p_z(i)}{p_z(hadron)}$: the longitudinal momentum fraction carried by the parton i to the total hadron momentum. Usually denoted as x.
- Feynman x, $x_F \equiv \dfrac{p_z^\star}{p_z^\star(max)}$: the longitudinal momentum fraction of final particle to the maximum momentum in the center-of-mass system.
- transverse mass $m_T \equiv \sqrt{p_T^2 + m^2}$.
- rapidity $y \equiv \dfrac{1}{2}\ln\left(\dfrac{p_0 + p_z}{p_0 - p_z}\right)$. Then $p_0 = m_T \cosh y$, and $p_z = m_T \sinh y$.
- pseudorapidity $\eta \equiv \dfrac{1}{2}\ln\left(\dfrac{|\boldsymbol{p}| + p_z}{|\boldsymbol{p}| - p_z}\right)$. Then $|\boldsymbol{p}| = p_T \cosh \eta$, and $p_z = p_T \sinh \eta$.

We consider a two-parton interaction $1 + 2 \to 1' + 2' + ...$ Two partons are from the incoming hadron beams of symmetric energy $\sqrt{s}$. Usually, the z axis is defined to parallel to the beam. At high energy ($\sqrt{s} \gg m_h$), before interaction, the four-momentum of the two partons are:

$$p_1^\mu = (x_1 \frac{\sqrt{s}}{2}, 0, 0, x_1 \frac{\sqrt{s}}{2}), \qquad p_2^\mu = (x_2 \frac{\sqrt{s}}{2}, 0, 0, -x_2 \frac{\sqrt{s}}{2}) \tag{B.1}$$

The four-momentum of final state particle j is:

$$p_j^{\mu\prime} = (p'_{0j}, \boldsymbol{p_T}'_j, p'_{zj}) \tag{B.2}$$

Due the momentum conservation

$$\begin{aligned}\frac{\sqrt{s}}{2}(x_1+x_2) &= \sum_j p'_{0j} \\ \frac{\sqrt{s}}{2}(x_1-x_2) &= \sum_j p'_{zj}\end{aligned} \tag{B.3}$$

Using $p'_{0j} = p'_{Tj}\cosh y_j$ and $p'_{zj} = p'_{Tj}\sinh y_j$, we can obtain

$$\begin{aligned}x_1 &= \frac{1}{\sqrt{s}}\sum_j p'_{Tj}e^{y_j} \\ x_2 &= \frac{1}{\sqrt{s}}\sum_j p'_{Tj}e^{-y_j}\end{aligned} \tag{B.4}$$

If we consider a two-particle final state, transverse momentum conservation requires $p'_{T1} = p'_{T2} = p_T$(neglect the symbol $\prime$), at mid-rapidity where $y_{1,2} \sim 0$, we have:

$$x_1 = x_2 = x_T = \frac{2p_T}{\sqrt{s}} \tag{B.5}$$

In general cases, we often use this treatment $x_{Bjorken} \approx x_T = 2p_T/\sqrt{s}$.

Since the maximum fraction of the longitudinal momentum for a certain parton is $\sqrt{s}/2$, the Feynman x is easily to be extracted:

$$x_F = \frac{2p_z}{\sqrt{s}} \tag{B.6}$$

APPENDIX C

Low energy charm cross section data points selection

There were a lot of charm cross section measurements at low energy ($\sqrt{s} < 70$ GeV). Table C lists all the charm cross section data points at low energies from journal publications. We ignored those data points extrapolated from high x_F and/or extremely low efficiency from correlation measurements, with extrapolation factor of $\gg 10$. The references for these data points are listed as followings. The data values included in the thesis are multiplied by 1.5 to account for the additional $D_s^{\pm}$ and $\Lambda_c^{\pm}$ contribution [FMN97].

1. S.P.K. Tavernier, *Rep. Prog. Phys.* 50, 1439(1987) and references therein.
2. NA32 collaboration, *Z. Phys. C* 39, 451(1988).
3. E769 collaboration, *Phys. Rev. Lett.* 77, 2388(1996).
4. NA16 collaboration, *Z. Phys. C* 40, 321(1988).
5. NA27 collaboration, *Phys. Lett. B* 135, 237(1984).
6. E743 collaboration, *Phys. Rev. Lett.* 61, 2185(1988).
7. E653 collaboration, *Phys. Lett. B* 263, 573(1991).

Table C.1: Overview of charm cross section data points at low energies and the criteria to include those in the thesis. Some experiments used $d\sigma/dx_F = (1-|x_F|)^{-n}$ for extrapolation.

Beam p (GeV/c)	Beam + Target	$\sigma_{c\bar{c}}$ (μb)	Comment	Included? Ref.
200	p + Si	1.5 ± 0.7	NA32,D^0, D^+,good acceptance (0-20%) at $x_F > 0$	✓ [2]
200	p + C_3F_8	$3.9^{+2.5}_{-1.9}$	NA25,Bubble chamber HOBC, 1μ trigger, $E(\mu) > 6$ GeV, good acceptance at $x_F > 0$ (8% efficiency)	✓ [1]
250	p + Be,Cu, Al,W	9.0 ± 1.5	E769, D^0, D^+, good acceptance at $x_F > 0$	✓ [3]
280	n + He/Ne	5.6 ± 1.7	E630 streamer chamber, 1μ trigger, $E(\mu)$ >6.5 GeV	✓ [1]
350	p + Fe	22 ± 9	CIT-Stanford, prompt 1μ trigger, $E(\mu)$ >20 GeV, acceptance 39%	✓ [1]
350	p + Fe	11.3 ± 2.0	FNAL-CCFRS, prompt 1μ trigger, $E(\mu)$ >20 GeV, n=5, x >0.3	✓ [1]
360	p + C_3F_8	$24.6^{+12.0}_{-8.3}$	See 200GeV data	✓ [1]
360	$p+p$	$5.5^{+8.2}_{-4.6}$	NA16, H_2 bubble chamber LEBC+EHS, good acceptance for x_F >0	✓ [4]
400	$p+p$	15.1 ± 1.7	NA27, H2 bubble chamber good acceptance for x_F >0	✓ [5]
400	p + Fe	31^{+29}_{-18}	CIT-Stanford, 1μ, $E(\mu)$ >20 GeV, $1.0 < p_T < 2.5$ GeV, 2.5%, n$\sim$5	✓ [1]
800	$p+p$	48^{+10}_{-8}	E743, LEBC-MPS, -0.1< x_F <0.5, n$\sim$8	✓ [6]
800	$p+p$	76^{+10}_{-19}	E653, -0.2< x_F <0.5, n$\sim$7	✓ [7]
400	p + Cu	320^{+150}_{-100}	GGM ν beam dump, n=3, $\langle x \rangle$ =0.8	× [1]
400	p + Cu	39 ± 10	CERN 1st ν beam dump, CDHS, $E(\mu) > 20$ GeV, n=3-5, $\langle x \rangle$ =0.8	× [1]
400	p + Cu	17 ± 4	CERN-BEBC, 2nd beam dump, $E(\mu) > 10$ GeV, n=4, $\langle x \rangle$ =0.8	× [1]
400	p + Cu	15 ± 5	CERN-CHARM ν beam dump, $E(\mu) > 20$ GeV, n=4, $\langle x \rangle$ =0.8	× [1]
400	p + W	15.5 ± 2.5	E613 FNAL ν beam dump, $E(\mu) > 20$ GeV, n=4, $\langle x \rangle$ =0.45	× [1]
400	p + Cu	~ 17	WA66-BEBC, CERN 2nd ν beam dump, $E(\mu) > 10$ GeV, n$\sim$5	× [1]
400	p + Cu	15.5 ± 2.9	CHARM, CERN 2nd ν beam dump, n=5	× [1]
400	p + Cu	~ 20	CDHS, CERN 2nd ν beam dump, n=5	× [1]
the above experiments cover high x, large extrapolation errors				

continued

Beam p (GeV/c)	Beam + Target	$\sigma_{c\bar{c}}$ (μb)	Comment	Included? Ref.
400	p + Fe	$7 \sim 20$	CIT-Stanford, 2μ+missing energy, p_T >0.75 GeV, 0.1-0.4% acceptance	× [1]
400	p + W	< 10	$\mu + \mu$ mass	× [1]
using correlation, low acceptance				
$\sqrt{s}$				
63	$p + p$	840 ± 320	ISR, trigger, $\Lambda_c(K\pi p)$ only, n∼0	× [1]
63	$p + p$	$150 - 450$	ISR, e trigger, $\Lambda_c(K\pi p)$ and $D(K\pi\pi)$	× [1]
62	$p + p$	650 ± 222	ISR, CBF, e trigger, n=3(D), n=0(Λ_c)	× [1]
62	$p + p$	129 ± 75	ISR, CBF, new runs, $\Lambda_c(K\pi p)$ only	× [1]
53-62	$p + p$	1390 ± 180	ISR, $\Lambda_c(K\pi p)$ only, n=0, x >0.75	× [1]
correlation, high x_F, large extrapolation errors				
53-62	$p + p$	70 ± 36	ISR, $e + \mu$ unlike-sign pairs, 0.0016% efficiency, n∼5	× [1]
53-62	$p + p$	73 ± 21	ISR, ee pairs	× [1]
correlation, low efficiency				

References

[Abr01] M.C. Abreu et al. *Phys. Lett. B*, **521**:195, 2001.

[ABR03] A. Andronic, P. Braun-Munzinger, K. Redlich, and J. Stachel. *Phys. Lett. B*, **571**:36, 2003.

[Aco03] D. Acosta et al. *Phys. Rev. Lett.*, **91**:241804, 2003.

[Ada03a] D. Adamova et al. *Phys. Rev. Lett.*, **91**:042301, 2003.

[Ada03b] J. Adams et al. *Phys. Rev. Lett.*, **91**:072304, 2003.

[Ada03c] J. Adams et al. *arXiv: nucl-ex/0309012*, 2003.

[Ada03d] J. Adams et al. *Phys. Rev. Lett.*, **91**:172302, 2003.

[Ada04a] J. Adams et al. *Phys. Rev. Lett.*, **92**:112301, 2004.

[Ada04b] J. Adams et al. *Phys. Rev. Lett.*, **92**:052302, 2004.

[Ada04c] J. Adams et al. *arXiv: nucl-ex/0406003*, 2004.

[Ada04d] J. Adams et al. *Phys. Rev. C*, **70**:044902, 2004.

[Ada04e] J. Adams et al. *Phys. Rev. Lett.*, **93**:252301, 2004.

[Ada04f] J. Adams et al. *Phys. Rev. Lett.*, **93**:252301, 2004.

[Ada04g] J. Adams et al. *Phys. Rev. Lett.*, **92**:171801, 2004.

[Ada05] J. Adams et al. "STAR white paper." *arXiv: nucl-ex/0501009*, 2005.

[Adc02] K. Adcox et al. *Phys. Rev. Lett.*, **88**:192303, 2002.

[Adc04] K. Adcox et al. "PHENIX white paper." *arXiv: nucl-ex/0410003*, 2004.

[Adl02a] C. Adler et al. *Phys. Rev. Lett.*, **89**:202301, 2002.

[Adl02b] C. Adler et al. *Phys. Rev. C*, **66**, 2002.

[Adl03a] S.S. Adler et al. *Phys. Rev. Lett.*, **91**:182301, 2003.

[Adl03b] S.S. Adler et al. *Phys. Rev. Lett.*, **91**:241803, 2003.

[Adl04a] S.S. Adler et al. *arXiv: nucl-ex/0409015*, 2004.

[Adl04b] S.S. Adler et al. *Phys. Rev. Lett.*, **92**:051802, 2004.

[Adl04c] S.S. Adler et al. *Phys. Rev. C*, **69**:014901, 2004.

[Adl05] S.S. Adler et al. *Phys. Rev. Lett.*, **94**:082301, 2005.

[Afa02] S.V. Afanasiev et al. *Phys. Rev. C*, **66**:054902, 2002.

[Ala01] J. Alam et al. *Phys. Rev. C*, **63**:021901, 2001.

[Alt03] C. Alt et al. *Phys. Rev. C*, **68**:034903, 2003.

[Alv96] G.A. Alves et al. *Phys. Rev. Lett.*, **77**:2388, 1996.

[Amm88] R. Ammar et al. *Phys. Rev. Lett.*, **61**:2185, 1988.

[And03] M. Anderson et al. *Nucl. Instr. Meth. A*, **499**:659, 2003.

[B76] F.W. Büsser et al. *Nucl. Phys. B*, **113**:189, 1976.

[Bar88] S. Barlag et al. *Z. Phys. C*, **39**:451, 1988.

[BCH03] E.L. Bratkovskaya, W. Cassing, and Stöcker H. *Phys. Rev. C*, **67**:054905, 2003.

[BCS04] E.L. Bratkovskaya, W. Cassing, H. Stöcker, and N. Xu. *arXiv: nucl-th/0409047*, 2004.

[Bea04] I.G. Bearden et al. *Phys. Rev. Lett.*, **93**:102301, 2004.

[Bjo83] J.D. Bjorken. *Phys. Rev. D*, **27**:140, 1983.

[BKG03] S. Batsouli, S. Kelly, M. Gyulassy, and J.L. Nagle. *Phys. Lett. B*, **557**:26, 2003.

[Bot90] O. Botner et al. *Phys. Lett. B*, 1990.

[Bra01] P. Braun-Munzinger. *Nucl. Phys. A*, **681**:119c, 2001.

[Bus04] P.J. Bussey et al. *arXiv: hep-ex/0408020*, 2004.

[Cas04] J. Castilllo et al. *J. Phys. G*, **30**:S1207, 2004.

[CER] CERN. "http://wwwasd.web.cern.ch/wwwasd/cernlib/.".

[Cro73] J.W. Cronin et al. *Phys. Rev. Lett.*, **31**:1426, 1973.

[DES04] X. Dong, S. Esumi, P. Sorensen, N. Xu, and Z. Xu. *Phys. Lett. B*, **597**:328, 2004.

[DG04] M. Djordevic and M. Gyulassy. *J. Phys. G*, **30**:S1183, 2004.

[DK01] Y.L. Dokshitzer and D.E. Kharzeev. *Phys. Lett. B*, **523**:199, 2001.

[DKS03] G. Dissertori, I. Knowles, and M. Schmelling. *Quantum Chromodynamics - High Energy Experiments and Theory.* Oxford Universidy Press, 2003.

[Eid04] S. Eidelman et al. "Review of Particle Physics." *Physics Letters B*, **592**:1+, 2004.

[FK02] Z. Fodor and S.D. Katz. *J. High Energy Phys.*, **0203**:014, 2002.

[FMN97] S. Frixione, M.L. Mangano, P. Nason, and G. Ridolfi. *arXiv: hep-ph/9702287*, 1997.

[GK04] V. Greco and C.M. Ko. *Phys. Rev. C*, **70**:024901, 2004.

[GKL02] M.I. Gorenstein, A.P. Kostyuk, McLerran L., H. Stöcker, and W. Greiner. *J. Phys. G*, **28**:2151, 2002.

[GKR04] V. Greco, C.M. Ko, and R. Rapp. *Phys. Lett. B*, **595**:202, 2004.

[GR01] L. Grandchamp and R. Rapp. *Phys. Lett. B*, **60**, 2001.

[Gra04] L. Grandchamp. *Private communications*, 2004.

[Gup98] R. Gupta. *arXiv: hep-lat/9807028*, 1998.

[HY04] R.C. Hwa and C.B Yang. *Phys. Rev. Lett.*, **93**:082302, 2004.

[Joh02] I. Johnson. Ph.D. Thesis, U.C. Davis, 2002.

[Kar02a] F. Karsch. *Lect. Notes Phys.*, **583**:209, 2002.

[Kar02b] F. Karsch. *Nucl. Phys. A*, **698**:199, 2002.

[KH03] P.F. Kolb and U. Heinz. *arXiv: nucl-th/0305084*, 2003.

[KL01] D. Kharzeev and E Levin. *Phys. Lett. B*, **523**:79, 2001.

[KLP00] F. Karsch, E. Laermann, and A. Peikert. *Phys. Lett. B*, **478**:447, 2000.

[Kod91] K. Kodama et al. *Phys. Lett. B*, **263**:573, 1991.

[LG96] Z. Lin and M. Gyulassy. *Phys. Rev. Lett.*, **77**:1222, 1996.

[Lin96] Z. Lin. Ph.D. Thesis, Columbia University, 1996.

[Lin04] X. Lin. *arXiv: hep-ph/0412124*, 2004.

[LK02] Z. Lin and C.M. Ko. *Phys. Rev. Lett.*, **89**:202302, 2002.

[Llo04] W.J. Llope et al. *Nucl. Instr. Meth. A*, **522**:252, 2004.

[LM03] Z. Lin and D. Molnar. *Phys. Rev. C*, **68**:044901, 2003.

[MNR93] M.L. Mangano, P. Nason, and G. Ridolfi. *Nucl. Phys. B*, **405**:507, 1993.

[MS86] T. Matsui and H. Satz. *Phys. Lett. B*, **178**:416, 1986.

[MV03] D. Molnar and S.A. Voloshin. *Phys. Rev. Lett.*, **91**:092301, 2003.

[NLC03] G.C. Nayak, M.X. Liu, and F. Cooper. *Phys. Rev. D*, **68**:034003, 2003.

[Pic95] A. Pich. *arXiv: hep-ph/9505231*, 1995.

[PV98] A.M. Poskanzer and S.A. Voloshin. *Phys. Rev. C*, **58**:1671, 1998.

[Rap01] R. Rapp. *Phys. Rev. C*, **63**:054907, 2001.

[RP03] J. Raufeisen and J.-C. Peng. *Phys. Rev. D*, **67**:054008, 2003.

[RRL03] I.V. Rakobolskaya, T.M. Roganova, and Sveshnikova L.G. *Nucl. Phys. B (Proc. Suppl.)*, **122**:353, 2003.

[RS03] R. Rapp and E.V. Shuryak. *Phys. Rev. D*, **67**:074036, 2003.

[Rua04a] L. Ruan et al. *J. Phys. G*, **30**:S1197, 2004.

[Rua04b] L.J. Ruan. Ph.D. Thesis, University of Science and Technology of China, 2004.

[Sha02] M. Shao et al. *Nucl. Instr. Meth. A*, **492**:344, 2002.

[Sha04] M. Shao et al. *Hot Quark Proceedings*, 2004.

[Sj01] T. Sjöstrand et al. *Computer Physics Commmun.*, **135**:238, 2001.

[Sor04] P.R. Sorensen. *Private communications*, 2004.

[SSH93] E. Schnedermann, J. Sollfrank, and U. Heinz. *Phys. Rev. C*, **48**:2462, 1993.

[STA04] STAR TOF Collaboration. *STAR TOF Proposal*, 2004.

[STA05] STAR HFT Collaboration. *STAR HFT Proposal*, 2005.

[Sto04] R. Stock. *J. Phys. G*, **30**:S633, 2004.

[Tai04] A. Tai et al. *J. Phys. G*, **30**:S809, 2004.

[Tav87] S.P.K. Tavernier. *Rep. Prog. Phys.*, **50**:1439–1489, 1987.

[TSR01] R.L. Thews, M. Schroedter, and J. Rafelski. *Phys. Rev. C*, **63**:054905, 2001.

[Vit03] I Vitev. *Phys. Lett. B*, **562**:36, 2003.

[Vog02] R. Vogt. *arXiv: hep-ph/0203151*, 2002.

[Vog03] R. Vogt. *Int. J. Mod. Phys. E*, **12**:211, 2003.

[Vog04] R. Vogt. *Private communications*, 2004.

[Wan00] X.N. Wang. *Phys. Rev. C*, **61**:064910, 2000.

[Wan04] F. Wang et al. *J. Phys. G*, **30**:S1299, 2004.

[WG91] X.N. Wang and M. Gyulassy. *Phys. Rev. D*, **44**:3501, 1991.

[Won94] C.-Y. Wong. *Introduction to High-Energy Heavy-Ion Collisions*. World Scientific Publishing Co. Pte. Ltd., 1994.

[Xu04] Z. Xu et al. *arXiv: nucl-ex/0411001*, 2004.

[ZGK99] B. Zhang, M. Gyulassy, and C.M. Ko. *Phys. Lett. B*, **455**:45, 1999.

[zzz05] zzz. *Phys. Rev. C*, **xx**:xx, 2005.